FACULTY OF SCIENCE
UNIVERSITY OF COPENHAGEN

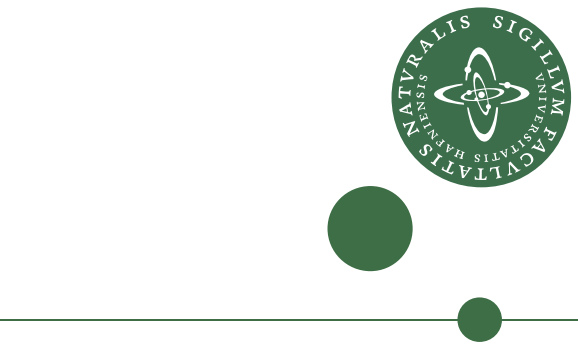

Master thesis

Measurement of Hard Double-Parton Interactions in $Z \to l\bar{l} + 2$ jet Events with the ATLAS Detector at $\sqrt{s} = 7$ TeV

Christian Caeser

Academic Adviser:
Peter Hansen

Discovery Center
Niels Bohr Institute
University of Copenhagen

18. Januar 2013

English Abstract

The aim of this thesis was the examination of multiple parton interactions (MPI) in $Z \to l\bar{l} + 2$ jet processes at the hadron level. The determination of MPI in real data samples taken by the ATLAS detector at the LHC in 2011 ($\sqrt{s} = 7$ TeV) was the main focus of this study. Minimum bias data corresponding to an integrated luminosity of 440.89 pb^{-1} and preselected muons data corresponding to an integrated luminosity of 161.31 pb^{-1} were used to perform the analysis. Events passing several selection criteria have been used to measure the fraction of MPI events f_{DP} by using the p_T balance between pairs of jets. To do this different Monte Carlo (MC) generators were used, namely Pythia and Sherpa. Eventually the amount of MPI in the data samples was extracted by using a template method. Additionally, in order to check the behaviour of the MC generators several properties were compared to real data properties.
The result for the fraction of MPI obtained here can confirm an earlier study conducted in 2012 on $W \to l\nu + 2$ jet events. The main result for the fraction of MPI obtained in this study is $f_{DP} = 0.062 \pm 0.024$ (stat.) ± 0.009 (sys.).

Dansk Resume

Formålet med denne afhandling er en undersøgelse af mange parton interaktioner (MPI) i $Z \rightarrow l\bar{l} + 2$ jet processer på hadron niveau. I denne undersøgelse er der hovedsageligt fokuseret på bestemmelsen af MPI i data produceret af ATLAS detektoren ved LHC i 2011 ($\sqrt{s} = 7$ TeV). Minimum bias data svarende til en integreret luminositet på $440,89$ pb^{-1} og præselekteret muon data svarende til en integreret luminositet på $161,31$ pb^{-1} blev brugt til at udføre analysen. Begivenheder, som opfylder bestemte udvælgelseskriterier, er blevet anvendt til at måle fraktionen af MPI begivenheder f_{DP} udfra forholdet i p_T mellem par af jets. For at gøre dette blev forskellige Monte Carlo (MC) generatorer anvendt, nemlig Pythia og Sherpa. Til sidst blev mængden af MPI i dataen ekstraheret ved hjælp af en skabelon metode. For at kontrollere adfærden af MC generatorerne blev adskillige af deres egenskaber sammenlignet med virkelige data. Resultatet opnået for fraktion af MPI kan bekræfte en tidligere undersøgelse gennemført i 2012 for $W \rightarrow l\nu + 2$ jet begivenheder. Det vigtigste resultat for fraktion af MPI opnået i denne undersøgelse er $f_{DP} = 0.062 \pm 0.024$ (stat.) ± 0.009 (sys.).

Acknowledgements

First of all I would like to thank my supervisor Peter Hansen for his guidance during the entire process of writing this thesis. I am very grateful for all the insightful discussions on topics related to my thesis and physics in general. Our discussions have been very enlightening and kept me motivated whenever my motivation slumped.
Secondly I would like to thank Sascha Mehlhase for reading my thesis before submitting it and giving me a lot of very good and helpful feedback. This thesis has benefited a lot from all his stylistic comments but especially from all his comments in terms of content. Margar Simonyan also deserves many thanks for all his useful comments and discussions while sharing an office with him.
I would also like to thank Karina Schifter-Holm for her nice company in the office and for giving me a hand with the translation of my abstract. Furthermore, I would like to thank all my other office mates that have made my time at the institute much more enjoyable.
Finally I would like to thank the entire work group at the university for offering me such a good time. I am very grateful for the friendly and informal atmosphere and felt very welcome during my whole time at the institute.

Contents

Chapter 1

Introduction

High energy physics is the part of physics that aims at understanding and explaining elementary particles and the interactions between them. Theoretically, particle physics is described by the Standard Model, a model first introduced about 40 years ago. It describes three of the four fundamental forces, namely the electromagnetic, the weak and the strong force. The exchange particles of these forces are the photon, the $W^{\pm}$ and the Z bosons and finally the gluon. The only force the Standard Model does not describe is the gravitational force and so far no theory was found that can describe the gravitational force and the phenomena described by the Standard Model together. These phenomena are the outcomes of particle physics experiments at particle colliders. However, in order to investigate particle physics in ever greater detail, colliders with ever higher energies are required. The most powerful particle accelerator to date is the Large Hardon Collider (LHC) which is situated in Switzerland at the border to France and consists of two main parts, the accelerator ring and the detector parts. The accelerator accelerates particles to energies required to perform particle physics experiments while the detectors record the outcomes of the particle collisions. In order to study particles and their interactions in ever greater accuracy, higher and higher energies are vital. At high energies the dominating force in particle processes is the strong force which is also the reason why the LHC is sometimes referred to as a gluon collider. Gluons are the strong force's exchange particles and thus mediate it between strongly charged particles. Most commonly when referring to particle collisions, a single partonic interaction is meant. However, this does not always have to be the case. There is also a considerable probability for more than one parton interaction per proton-proton collision. Such an event is called a multiple parton interaction. Earlier experiments like those conducted at the Tevatron have already indicated that there is a non-negligible contribution from multiple parton interactions in

proton-proton collisions. However, they are still not very well understood and this makes further studies in this area necessary.

The main aim in this thesis is to gain a better understanding of multiple parton interactions in proton-proton collisions. Furthermore, I will attempt to determine how well Monte Carlo generators reproduce experimentally recorded data. Whether the results from different generators confirm each other and which variables are especially useful for the investigation of multiparton processes. The obtained Monte Carlo simulations will be compared to real data which was recorded in 2011 by the ATLAS detector. Finally the simulations will be used as so called templates in order to determine the fraction of multiple parton interactions in real data.

The first part of this study will serve as an overview over particle physics, the standard model and other theoretical and phenomenological properties that are important to know about for this study. The second part (Chapter three) will introduce the ATLAS detector which is used to record experimental results and some of the methods that are used to reconstruct specific properties. Chapter four covers Monte Carlo generators; the programs that are to simulate real particle collisions as accurately as possible. The final part, chapter five, will then present the results obtained in this study. Processed experimental data will be shown as well as results from Monte Carlo generators. The used generators will be compared with each other as well as generator results with the real data. Finally, the fraction of multiple parton interactions in the recorded data will be determined.

Chapter 2

Theoretical Background

This chapter will provide an overview over the theoretical background of particle physics. First the Standard Model will be introduced and all the particles and interactions associated with it. The succeeding sections about Quantum Field Theory (QFT) and Quantum Chromodynamics (QCD) will introduce the strong force from a more theoretical perspective. The chapter will close with a detailed description of proton-proton collisions and the phenomena connected with them. In particular the last section of the chapter describes multiple parton interactions (MPI), a phenomenon that is of major interest in this study.

2.1 The Standard Model

The Standard Model of particle physics [1, 2, 3] is a theory that describes all the known elementary particles and the interactions between them. The interactions between particles are mediated by exchange particles called gauge bosons. From a mathematical point of view it is based on a $SU(3)_C \otimes SU(2)_L \otimes U(1)_Y$ gauge theory. The current version of the Standard Model describes three of the four elementary forces namely, the electromagnetic, the weak and the strong force. The gravitational force, however, is missing and cannot be described by the Standard Model. The search for a unification of all four forces into a single theory of everything (TOE) (see Figure 2.1) is one of the main aims of particle physics research. So far however it has not been possible to develop such a theory but there are many promising approaches and much research is conducted on it. Additionally, there are also theories like Supersymmetry (SUSY) [4] or additional extra dimensions [5, 6] that aim at describing hypothetical particles or additional symmetries.
Theoretically the Standard Model is based on quantum field theory. It provides a

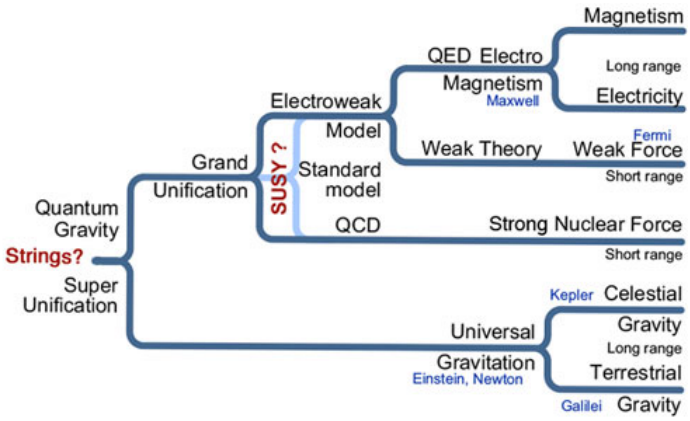

Figure 2.1: Unification of the fundamental forces [7]; A Theory of Everything would be a Super Unification

superstructure for the single theories it incorporates. These theories describe die aforementioned forces (electromagnetic, weak and strong) and the Higgs mechanism. The theory describing the strong force is called quantum chromodynamics and describes the interactions between elementary particles with colour charge. It will formally be introduced in Chapter 2.3 since it is of large interest in this thesis. Another pillar of the Standard Model is the electroweak interaction. It is a quantum field theoretic gauge theory that unifies the electromagnetic and the weak force. Finally the Higgs mechanism is the part of the Standard Model that describes the origin of the masses of the particles.

2.1.1 Particles and Their Interactions

The particles contained in the Standard Model can be separated into two groups. One representing fermions, those are the particles with half integer spin, the other representing bosons, which are the particles with integer spin.
The first group, the fermions (see Table 2.1), can further be divided into two groups - quarks and leptons. These two particle classes can, again, be divided into three groups, often referenced to as generations. Every generation consists of four fermions - two quarks and two leptons. Higher generations are considered to be heavier copies of the lowest generation since the particles in higher generations have exactly the same quantum numbers as the members of the lowest generation with one difference, their mass. A muon for example acts in its interactions very similar to an electron. Differences appear only due to the larger mass of the muon. The fermionic constituents of the Standard Model, quarks and leptons, are both

elementary particles, meaning, according to current knowledge they do not contain a substructure. Aside from apparent differences between quarks and leptons, like different masses or electric charges, only quarks interact strongly. In principal there could be even more generations but to this day there has been no evidence for further generations. On the contrary, a recent study [8] conducted in 2012 presented a very strong indication that, given a Standard Model Higgs boson at $m_H \approx 126$ GeV, there are exactly three generations.
Almost all the matter in the Universe contains quarks of the first generation which is due to the fact that, as aforementioned, larger generations are just heavier copies of the lightest generation. Members of higher generations are not stable and thus decay into members of a lighter generation. Quarks may be the constituents of all the matter in the Universe however, they only appear in very certain combinations. Single quarks for example do not represent stable matter particles. Even most combinations of quarks do not represent stable particles. This is due to one of the quantum numbers all quarks posses, colour. More on colour and the associated interaction in Chapter 2.3.
Another property that makes the situation even more complex is the fact that every fermion has an antiparticle. An antiparticle is an exact copy of the 'normal' particle in terms of mass, spin and magnetic moment except for two differences. The electric charge and the particle's parity are the opposite of the 'normal' particle.

Quarks				
Particle	Generation	Mass [MeV]	Electric charge [e]	Interaction
up (u)	I	$1.8 - 3.0$	2/3	strong, weak, EM
down (d)		$4.5 - 5.5$	-1/3	strong, weak, EM
charm (c)	II	$1,275 \pm 25$	2/3	strong, weak, EM
strange (s)		95 ± 5	-1/3	strong, weak, EM
top (t)	III	$173,500 \pm 0.6 \pm 0.8$	2/3	strong, weak, EM
bottom (b)		$4,180 \pm 30$	-1/3	strong, weak, EM
Leptons				
electron e	I	0.511	-1	weak, EM
electron neutrino ν_e		$< 2 \cdot 10^{-6}$	0	weak
muon μ	II	105.66	-1	weak, EM
muon neutrino ν_μ		< 0.17	0	weak
tau τ	III	$1,776.82 \pm 0.16$	-1	weak, EM
tau neutrino ν_τ		< 15.5	0	weak

Table 2.1: Fermions in the Standard Model [3], EM stands for electromagnetic; The mass unit is given in natural units, meaning $c = 1$. Where no uncertainties on the mass measurements are given they were omitted due to them being very small (in the order of 10^{-6} or smaller) and to maintain a better overall view

Gauge Boson(s)	N	Charge	Range	RS	Interaction	IP	Gauge Group
Gluons (g)	8	Colour	10^{-15}	1	Strong	Q	SU(3)
$W^{\pm}$, Z boson	2	Weak	10^{-18}	10^{-6}	Weak	Q, L	SU(2)
Photon (γ)	1	Electric	∞	10^{-2}	EM	EL	U(1)
Graviton (hypo.)	1	-	∞	10^{-40}	Gravity	Q, L, DM(?)	?

Table 2.2: Bosonic constituents of the Standard Model [3]; EM = electromagnetic; N = Number of bosons; The range is measured in meters; RS = relative strength; IP = interaction partners; hypo. = hypothetical; Q = Quarks; L = Leptons; DM = Dark Matter; EL = electrically charged particles

The other group of particles, the bosons, contains the gauge particles. These are the particles that mediate the elementary forces. In total the elementary forces provide 12 gauge particles, or 13 with the hypothetical graviton, the gauge particle of gravitation. Details on the gauge bosons can be seen in Table 2.2.

The exchange particle of the electromagnetic force is the massless photon. It only couples to particles with an electric charge while not having an electric charge itself. The force carriers of the weak force are the neutral Z ($m_Z \approx 91.187$ GeV) and the charged $W^{\pm}$ bosons ($m_W \approx 80.385$ GeV) which account to three in total.
The strong force is mediated by a massless exchange particle called gluon. Just as the particles they interact with, gluons carry a colour charge themselves. Colour is a characteristic property of the strong force and all strongly interacting particles (quarks and gluons) have a colour charge. However, where quarks only possess a single colour, gluons have two colours, a colour and a, not necessarily corresponding, anticolour. Considering that there are three colours (red, green, blue) and the same number of anticolours (antired, antigreen, antiblue) the total number of colour combinations gluons can take should be nine, however there are only eight different states gluons can hold. One of the nine possible states would make the gluon a colour singlet which could only interact with other colour singlet states. However at very close distances particles like quarks have a colour and thus would not interact with a colour singlet gluon. At very large distances on the other hand there is no strong interaction any more (see Chapter 2.3.1). An illustration of the couplings between quarks, leptons and the exchange particles can be seen in Figure 2.2. The, so far only theoretical, exchange particle of gravitation is called graviton. If it exists it will be a massless, spin 2 particle. It has not yet been discovered and it does not seem as if it will be detected in the near future due to its very small cross-section.
Finally, there is one more boson predicted in the Standard Model, the Higgs boson [10]. On the contrary to the other twelve bosons (eight gluons, three weak bosons and one photon) the Higgs boson is not the result of gauge symmetry

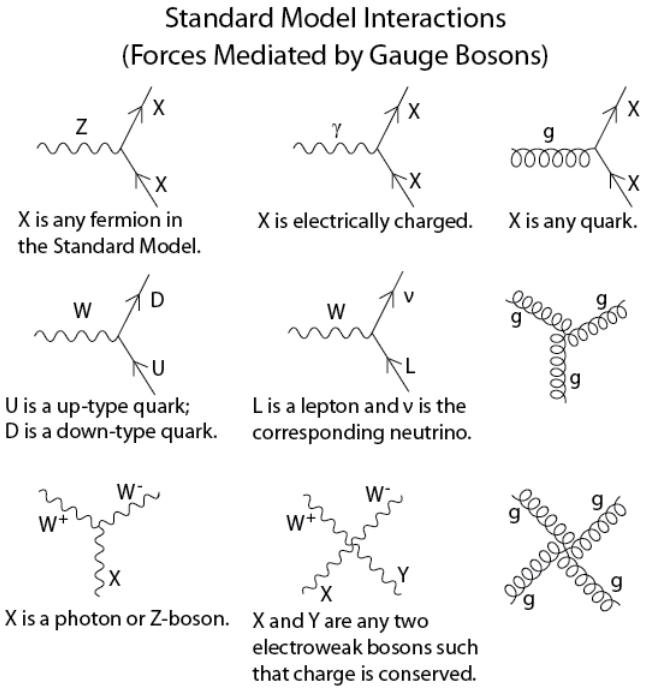

Figure 2.2: Feynman diagram of the interactions between the particles of the Standard Model [9]; The name originates from their inventor, Richard Feynman

and is thus not a force carrier. Nevertheless, it is a very important particle. It is needed to break the electroweak $SU(2) \otimes U(1)$ symmetry which then assigns mass to the Z and W bosons. With the introduction of Yukawa couplings it is also explainable how fermions get their mass by interacting with the Higgs field. The discovery of the Higgs boson is one of the main aims of the LHC. On the 4^{th} of July 2012 the discovery of a new boson was announced. The new particle shows all the properties of the sought after Higgs boson. The new boson was found in a mass range the Standard Model Higgs boson was expected in and it decayed, with about the correct frequency, through channels (e.g. $H \rightarrow W^+W^-$) that were predicted by theoretical calculations. However, it has not (yet) been declared the discovery of the Higgs boson as the measured precision was not (yet) high enough. The newly detected boson has, according to the results obtained by the ATLAS detector, a mass of $m \approx 126.5$ GeV [11] while CMS arrived at $m = 125.3 \pm 0.4$ (stat.) ± 0.5 (sys.) GeV [12]. Later in July, on the 31^{st} of July 2012 both collaborations published updated results from additional data. The ATLAS (CMS) collaboration was able to increase the significance to 5.9σ (5σ) and update the mass measurement to $m = 126.0 \pm 0.4$ (stat.) ± 0.4 (sys.) GeV [13]

($m = 125.3 \pm 0.4$ (stat.) ± 0.5 (sys.) GeV [14]). However, has not yet been declared the sought after Standard Model Higgs boson since the two experiments (CMS and ATLAS) reached a local significance of 5σ; however, a significance of 6σ is needed for a new discovery.

2.2 Quantum Field Theory

The Standard Model describing our current knowledge of particle physics is mathematically founded on a theory called quantum field theory (QFT) [2, 15]. Quantum field theories were first developed in the early twentieth century. They are combinations of classical field theories, like electromagnetism, with quantum theory (i.e. quantum mechanics) into a quantum field theory, in this case quantum electrodynamics. Merging these two theories became necessary since quantum mechanics alone could not deliver satisfying answers to some of the questions posed at the time, like how to describe physical systems with a varying number of particles. Today, there exist two different kinds of quantum field theories; relativistic and non-relativistic quantum field theories. The latter ones are of great importance in solid state physics while the former are the ones that are important for particle physics. The term relativistic means that the quantum field theory has been combined with the special theory of relativity (STR).
There are a number of things in quantum field theories that are fundamentally different from classical physics. For one thing, in QFT particles and fields are described by the same formalism; the Lagrange formalism. This is possible since QFT is a further development of quantum mechanics. Another feature distinguishing QFT from classical physics is the way the equation of motion is treated. In classical physics a method called the principle of least action is used to determine the equation of motion. However, to determine the equation of motion one first has to establish a function describing the dynamics of a physical system [16, 17] called the Lagrangian L. It is given by

$$L = T - V \ , \tag{2.1}$$

where T and V are the kinetic and the potential energy of the system. If a particle, described by the Lagrangian L, moves from a start- to an endpoint there are in principle various possible paths. In order to determine the path actually taken by

the particle it is useful to define a new function called action. It is defined by

$$S = \int \mathrm{d}t L(t, x(t), \dot{x}(t)) \ . \tag{2.2}$$

The action takes the dynamics of the system, represented by L, and allocates it with a real number. The path can now be determined by minimising the action $\delta S = 0$. This leads to the equation of motion

$$\frac{\mathrm{d}}{\mathrm{dt}} \left(\frac{\partial L}{\partial \dot{x}} \right) - \frac{\partial L}{\partial x} = 0 \ . \tag{2.3}$$

If, instead of a single particle, a field is considered the Lagrange function must be replaced by the Lagrangian density [18] in a volume element since the field fills the volume element. The relation between the Lagrange density and the Lagrange function is given by

$$L = \int \mathrm{d}^4 x \mathcal{L}(\phi, \partial_\mu \phi) \ . \tag{2.4}$$

The lagrange density depends on the quantum field $\phi(x, y, z, t)$ filling the space and its first derivatives. Performing the same steps analogously to the classical case, the equation of motion for quantum fields is obtained,

$$\partial_\mu \left(\frac{\partial \mathcal{L}}{\partial(\partial_\mu \phi)} \right) - \frac{\partial \mathcal{L}}{\partial \phi} = 0. \tag{2.5}$$

However, as opposed to classical physics in quantum field theory there might be several paths minimising the action. All these paths would be valid solutions and thus would have to be taken into account in order to determine the correct equation of motion. This is done by summing over all valid solutions by using a procedure called the Feynman path integral formalism.

2.3 Quantum Chromodynamics

Quantum chromodynamics (QCD) [2, 19, 20] is the quantum field theory describing the strong interactions of gluons and quarks. It is based on a non-abelian $SU(3)_c$ gauge theory and thus comes with $3^2 - 1 = 8$ exchange particles called gluons. The strong interaction is one of the four fundamental forces in nature and since its first

introduction there has been much affirming evidence [21].
It was introduced to describe the binding of the quarks within protons and neutrons. Initially quarks were considered as free particles which means that classically they would have had to repel and move apart from each other, thus dissolving as a composed particle. This is clearly not the case. Even worse, quarks, which were explained as free particles, were never observed as free particles but only as part of some larger particle consisting of several quarks. These composed particles came in two categories, baryons and mesons. Baryons are particles consisting of three quarks (or three antiquarks) while mesons contain a quark and an anti-quark.
However, there were also other indicators hinting that something with the existing description of particle physics was not in order. Over time several new hadrons were discovered. Some of those new particles however led to problems. The observed $\Delta^{++} = (u\uparrow, u\uparrow, u\uparrow)$ (the arrows denoting the spin) for example would have been forbidden according to the Pauli exclusion principle. It states that fermions, like quarks, which occupy the same space cannot match in all quantum numbers. The fact that the Δ^{++} baryon was in fact observed resulted in the introduction of a new degree of freedom called colour charge. There are three QCD colours named after ordinary colours - red, green, blue - although they do not have anything in common with them. The fact that there are exactly three might seem arbitrary but has been confirmed experimentally by the measurement of the fraction R_{had} [1, 19].

From a theoretical point of view QCD is represented by the following Lagrangian density:

$$\mathcal{L}_{QCD}(q, A) = \bar{q}(i\gamma^\mu D_\mu - m)q - \frac{1}{4}F^a_{\mu\nu}F^{\mu\nu}_a \ . \tag{2.6}$$

Inserting the covariant derivative

$$D_\mu = \partial_\mu + igT_aA^a_\mu \ , \tag{2.7}$$

the Lagrangian density can be rewritten as

$$\mathcal{L} = \bar{q}(i\gamma^\mu\partial_\mu - m)q - g\bar{q}\gamma^\mu T_a g A^a_\mu - \frac{1}{4}F^a_{\mu\nu}F^{\mu\nu}_a \ . \tag{2.8}$$

In more detail the Lagrangian is defined by the fermionic quark field q with $\bar{q}$ being the adjoint quark field. The γ^μs are the usual four Dirac matrices and the factor g is the coupling constant of the strong interaction. T_a stands for the generator of the

$SU(3)$ gauge group. A^a_μ are the bosonic gluon field of which there are eight. The last factor, $F^a_{\mu\nu}$, is the field strength tensor

$$F^a_{\mu\nu} = \partial_\mu A^a_\nu - \partial_\nu A^a_\mu + g f^{abc} A^b_\mu A^c_\nu \ . \tag{2.9}$$

The terms defining $F^a_{\mu\nu}$ are the same as already described above expect f^{abc} which is a term called structure constant of the gauge group. The field strength tensor describes a field in gauge theories and is also the term that causes the main difference between quantum electrodynamics (QED) and QCD. QED is an abelian gauge theory for which the commutator of the fields vanishes by definition. In non-abelian gauge theories, like QCD, on the other side the commutator does not vanish and thus leads to terms which indicate a self interaction of QCD's exchange particles [22].

2.3.1 Asymptotic Freedom and Confinement

In quantum field theories like quantum chromodynamics, it is possible to express physical observables by using perturbation theory. This means expressing the quantity as a series; in the case here in powers of the coupling parameter α_s. However, this approach can only be used if the coupling constant is very small ($\ll 1$) so that the series converges quickly enough. Depending on whether perturbation theory can be used QCD is split into to regimes - perturbative (pQCD) and non-perturbative QCD. While for pQCD calculations can be performed to obtain results, this is not the case for non-perturbative QCD. Thus one has to fall back on phenomenological models, like in the case of hadronisation. When calculating physical quantities renormalisation requires the introduction of an arbitrary energy scale to remove ultraviolet divergences. Ultraviolet divergence refers to cases where an integral has contributions that cause it to become infinite. In all these cases the infinite contributions make any result meaningless because infinite, thus a cutoff scale is required which removes these distorting contributions and allows a useful result. This leads to the conclusion that the strong coupling parameter depends on this energy scale (see Figure 2.3). Unlike in the case of the weak interaction where the energy dependence is almost negligible it does have a large effect on the strong coupling parameter. The large effect is caused by gluons which carry colour charge themselves and thus interact with each other. In first order perturbation theory the strong coupling constant is given by

$$\alpha_s(\mathrm{Q}^2) = \frac{12\pi}{(33 - 2\mathrm{N_f}) \cdot \ln(\mathrm{Q}^2/\Lambda^2)} \ . \tag{2.10}$$

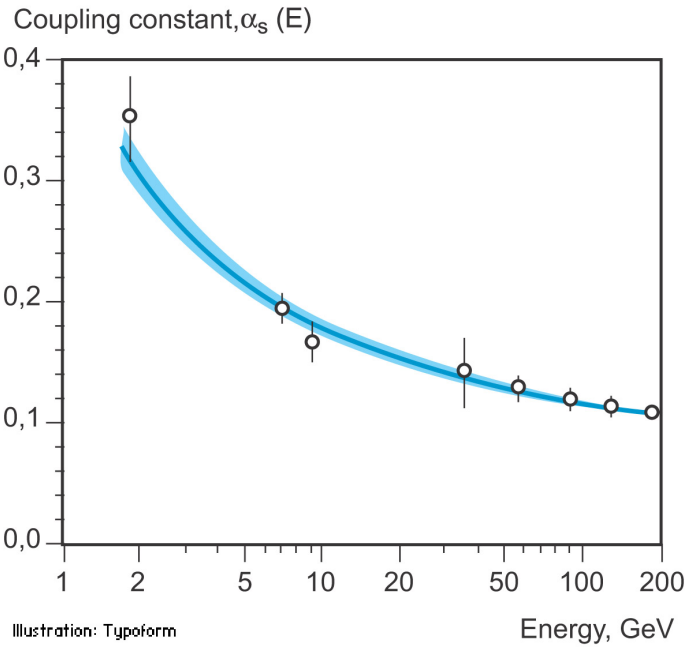

Figure 2.3: Results from the HERA experiment directly confirming asymptotic freedom [23]

In this expression N_f is the number of participating quark flavours which is usually between 3 and 6. Due to their large mass, heavy quarks are usually only very rarely produced. Λ is the only free parameter in QCD. It has to be determined by comparing experimental results with theoretical predictions.

The arbitrary energy scale Q^2 also has a second meaning, it describes the distance between interacting particles. The higher the energy of a parton the closer it can approach another parton which might repel it. Thus for small distances, or large values of Q^2, the coupling between colour charged particles becomes weaker and vanishes asymptotically. This means that in the limit $Q^2 \to \infty$ quarks can be considered as free particles. For large distances however (small Q^2 values) the coupling becomes very strong, and increases further with growing distance. This phenomenon of free quarks but only within bound composite particles, is called confinement. If two strongly bound particles move too far apart from each other, the gluon holding them together will split into two and produce a new $q\bar{q}$ pair at the endpoints out of the vacuum. The gluon splits into two because the energy stored between the two connected partons increases with distance.

2.4 Limitations and Open Questions

The Standard Model does a remarkably good job at describing particle physics. It has frequently been confirmed by experimental results, however even though it does already describe particle physics very well, there still remain open questions.
One of these open questions is whether the three forces of the Standard Model are unified at high energies. So far the Standard Model unifies two of the three forces, namely the weak and the electromagnetic forces, to the electroweak force. The next step towards a grand unified theory (GUT) would be to include the strong interaction. This could be done for example by using $SU(5)$ or $SO(10)$ symmetry groups. This way it is also possible to unify the coupling constants for mass scales higher than $\Lambda_{GUT} \sim 10^{16}$ GeV to one single coupling constant. The GUT scale Λ_{GUT} is the energy scale above which all the four forces are believed to become equally strong.
Of course, to fully describe all known forces, gravitation would have to be included and even a GUT does not include gravitation. The problem with gravitation is that at current energy scales it is too weak to have a discernible effect on physics results. Only from the Planck scale ($m_p \sim 10^{19}$ GeV) onwards does gravitation play a considerable role. However, working at the Planck scale poses new problems since general relativity which is the canonical theory of gravitation cannot be expressed as a quantum field theory. This is due to the fact that gravitation is not renormalisable. The great interest in the unification of all four forces comes from the assumption that at the big bang all four forces were combined in one single force.
Furthermore, the Standard Model is based on 18 free parameters and if massive oscillating neutrinos are included on another 7 free parameters. This means 25 free parameters in total. The values of these parameters have to be determined in experiments. This is at least considered as inelegant by many.
Neutrinos are an interesting topic by themselves. The Standard Model does predict neutrino masses, however it cannot predict their exact values but only their mass differences.
Another question arises from the asymmetry of matter and anti-matter. Astrophysical experiments [24] have shown that 23% of the Universe consist of dark matter. Another 72% consist of dark energy and only the remaining 5% of the Universe consists of baryonic matter, which can be described by the Standard Model. This asymmetry cannot be explained by CP violation alone.

2.5 Proton-Proton Collisions

While at low energies colliding hadrons, like protons which are used at the LHC, just scatter elastically the situation becomes much more complex at high energies, like the ones achieved at the LHC ($7 \leq \sqrt{s} \leq 14$ TeV). At these energies protons reveal a substructure which is made up of other (elementary) particles, namely quarks and gluons. Gluons are the already mentioned exchange particles of the strong force while quarks appear as two different types, as valence quarks and (virtual) sea quarks. The valence quarks are the quarks that determine the particles chemical properties while the sea quarks are the result of vacuum fluctuations. Particles arising from vacuum fluctuations are not permanent particles meaning that they are created out of the vacuum and annihilate shortly after their creation. This sort of behaviour is granted by Heisenberg's uncertainty relation. Aside from the valence quarks the sea quarks largely contribute to the physical properties (mass, momentum, spin) of the proton.
Thus, in a pp collision at LHC energies the protons will interact with each other but the actual physical processes will be carried out by the aforementioned constituents of the proton, the partons. An illustration of a proton-proton collision and the accompanying processes can be seen in Figure 2.4. The figure shows that it is not a hard interaction alone causing the particle spectrum recorded by particle detectors but various different processes. The hard interaction is just the process defining the collision since all hard processes are accompanied by secondary processes. These secondary processes are radiative processes like initial state radiation (ISR) or final state radiation (FSR). In ISR or FSR a parton emits a gluon or a photon prior or after the hard interaction respectively. Additionally, QCD forbids the beam remnant, the rest proton after the hard interaction, to remain in the colour charged state it holds after the pp collision. In the following a more detailed description of pp collisions will be presented. The processes defining an event is the hard scattering processes. Two partons, one from each proton, annihilate into an exchange particle which will decay again and thus producing final state particles. Such a hard scattering process that is very likely at the LHC at the same time is for example gluon-gluon fusion, or more specifically a process like $gg \to g \to q\bar{q}$. However, such a hard scattering process is always accompanied by secondary processes. These accompanying processes are usually soft processes meaning that the transverse momenta of the participating particles is comparatively small. Particles originating from a hard interaction on the other side have rather high transverse momenta.
More specifically, the secondary processes comprise various different processes. For one thing, the rest proton is no longer a colour neutral particle which it should be according to QCD's confinement property. In order to regain colour neutrality the rest proton which is mostly called beam remnant will undergo a process called hadro-

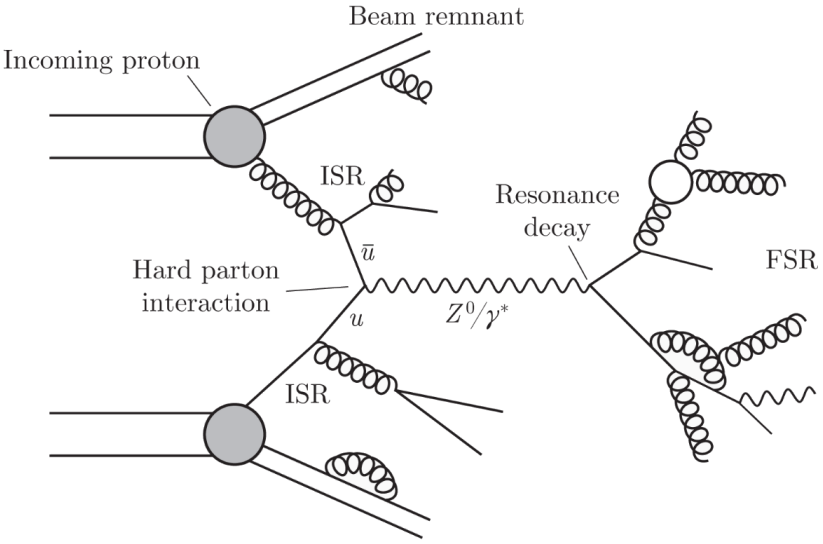

Figure 2.4: Schematic depiction of a single parton scattering in a proton-proton collision [25].

nisation. However, hadronisation is not process only affecting the beam remanants but all particles that participated or were created in the process. The coloured particles recombine with other coloured particles in order to regain colourlessness. These other coloured particles are either already existent through other processes or created out of the vacuum, for example by splitting gluons. This process continues until there are no more free coloured particles. Obviously the same has to happen after the main process. After two partons annihilated into an exchange particle the exchange particle again will decay into a permitted set of partons. Furthermore, partons can emit gluons basically at any point of the process (of course only if energetically permitted). The process of emitting a gluon prior to the hard interaction is called initial state radiation while the emission afterwards is called final state radiation. In real data the distinction between the two sorts of radiation is made by determining roughly the pseudorapidity (see Chapter 3.1.1) of the resulting particles.
All these processes not directly associated with the hard interaction are often summarised in the underlying event (UE). Even though there is no strict definition of it 'Everything but the hard interaction' usually describes it very well.
From a theoretical point of view, the cross-section for a specific single parton scattering process $i, j \to a, b$ in a pp collision can be described by

$$d\sigma^{SPS}_{ij\to ab} = \sum_{i,j} \int \mathrm{d}x_1 \int \mathrm{d}x_1^{'} f_p^i(x_1, \mu) f_p^j(x_1^{'}, \mu) \mathrm{d}\hat{\sigma}_{(ij\to ab)}(x_1, x_1^{'}, \mu) \ . \tag{2.11}$$

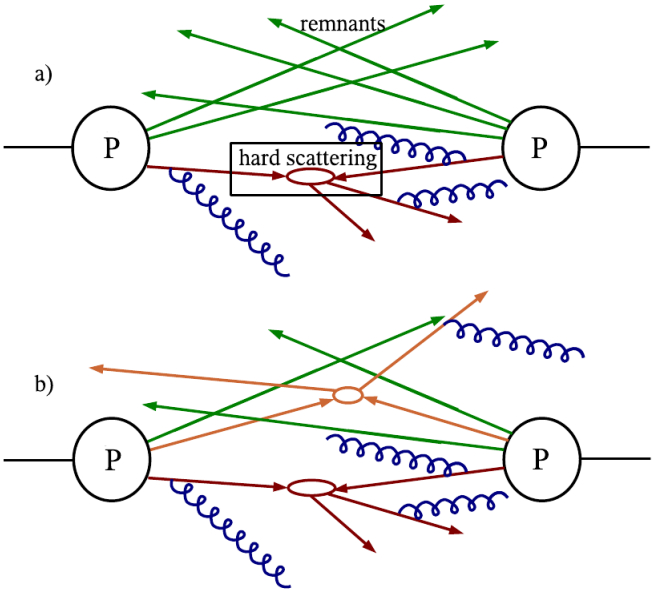

Figure 2.5: a) Single Parton Scattering (SPS): A single hard collision, b) Multiple Parton Interactions (MPI): A hard collision accompanied by a second hard collision

More specifically such a specific process can be something like $q\bar{q} \rightarrow l\bar{l}$. The cross-section is an expression for the likelihood of an interaction to occur. The single terms are the two parton distribution functions (see Chapter 4.2) for the two participating partons $f_p^i(x_1, \mu)$ and $f_p^j(x_1^{'}, \mu)$. Here x_1 and $x_1^{'}$ stand for the fraction of the protons momentum that is being carried by the parton, while μ is the partonic renormalisation scale. Often there is more than one possibility for the production of a specific particle (e.g. production of a Z boson by different quark flavours), in this case one has to sum over all those possibilities to calculate the total cross-section.
All the so far presented properties regarding pp collisions have only concerned single parton scatterings (SPS). At LHC energies however, there is also a considerable amount of events where the hard scattering process is accompanied by a second parton-parton interaction. Figure 2.5 depicts both situations. In part a) a single parton scattering is shown. It depicts the hard interaction (see 'hard scattering' box in Figure 2.5) and the accompanying processes. The proton rests are the green arrows, the blue spirals are ISR and FSR. Part b) of Figure 2.5 on the other hand depicts a multiple parton interaction. It can be seen that in this case there are to parton-parton interactions, one with the dark red arrows and the other with the pink arrows. Multiple parton interactions are of great importance in this thesis and will be introduced more thoroughly in the following chapter (see Chapter 2.6).

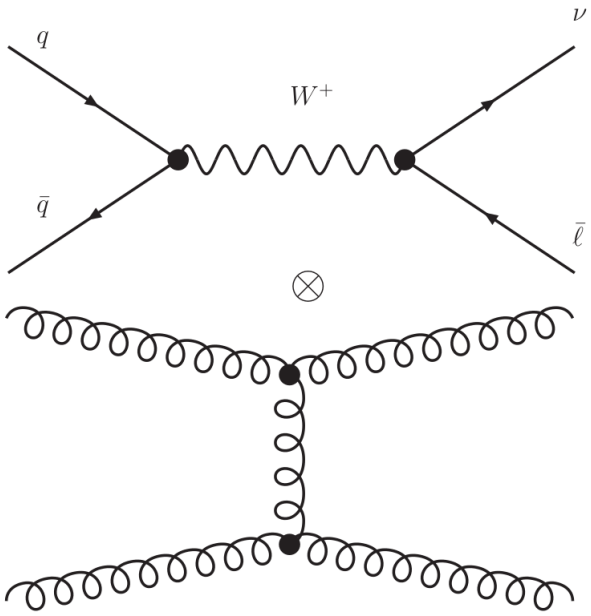

Figure 2.6: Theoretical perception of a multiple parton interaction [27]. A multiple parton interaction is considered as a hard scattering process accompanied by a second parton-parton interaction. The figure shows a first primary hard interaction ($q\bar{q} \to W^+ \to \bar{l}\nu$) which is accompanied by second interaction ($gg \to gg$)

2.6 Multiple Parton Interactions

Multiple parton interactions (MPI) as introduced in [26, 27, 28] are, together with beam remnant interactions, the least understood part of proton-proton collisions. A schematic depiction of a multiple parton process can be seen in Figure 2.6. MPI describe the phenomenon when a hard primary interaction is accompanied by a second scattering process. They are often split into two groups, soft and hard MPI. Just as for jets, there is no fixed cut-off value separating soft and hard interactions but the general rule is; if the resulting particles have a rather high transverse momentum (see Chapter 3.1.1) it is called hard MPI otherwise it is called soft MPI. While hard MPI occur rather rarely, soft MPI are very frequent phenomenons. In principal there can be even higher numbers of additional subprocesses which would lead to triple or even higher parton interactions. The probability for these processes is small and therefore the focus is usually on double parton scatterings (DPS)[1].

For several reasons multiple parton interactions are an important field of study. A

[1]Often also called double parton interactions (DPI) or double parton scattering (DPS). In this study MPI, DPS and DPI will be used interchangeably.

short answer to the question why MPI are important to study is because the LHC is basically a gluon collider. This is because the gluonic parton distribution function is, by far, the most dominant at high energies and small longitudinal momentum fractions (see Figure 4.2), thus the name gluon-gluon collider. More details on parton distribution functions can be found in Chapter 4.2. At the same time as the energies in particle colliders increase, so do the parton densities in the protons and with higher parton densities the probability for MPI increases. However, this is not the only reason for interest in this topic. MPI are also important for precision measurements and pose as backgrounds in other areas, like the Higgs search as well as in SUSY studies. Finally, the fact that they are theoretically not yet fully understood makes studies in this area even more important in order to support theorists in their development of new approaches.
Turning now to the more technical features of the description of MPI. The leading order partonic cross-section of a hard scattering process above some p_T is given by

$$\sigma^{\text{hard}}(p_T) = \int_{p_T^2}^{s/4} \frac{d\sigma}{dp_T^2} dp_T^2 \ . \tag{2.12}$$

At zero momentum $p_{T_{min}} \to 0$ the differential cross-section diverges due to the exchange of virtual massless gluons. To counter the problem of divergence, a lower bound, a minimum momentum transfer $p_{T_{min}}$, is introduced. For reasonable $p_{T_{min}}$ values however, the integrated gluon-gluon cross-section for example becomes very large. In fact so large that it supersedes the total cross-section for the pp collision. This might seem like a contradiction but it really is not, it only means that the average number of gg-interactions in a single pp collision is larger than one. This alone already indicates that MPI are not rare and this remark is only for gg processes. Taking subprocesses including quarks into account even increases the probability for MPI. As a result of the above the cross-section of the hard process alone and the total cross-section is used to determine the expected number of partonic collisions per event,

$$N_{\text{MPI}} = \frac{\sigma^{\text{hard}}}{\sigma^{tot}} \ . \tag{2.13}$$

The starting point for the theoretical description of MPI are single parton scatters (SPS) (as depicted in Figure 2.7). A single parton scatter can be a usual QCD $2 \to 2$ process. The differential cross-section for such a process is given by:

$$d\sigma^{SPS}_{ij\to ab} = \sum_{i,j} \int \mathrm{d}x_1 \int \mathrm{d}x_1^{'} f_p^i(x_1,\mu) f_p^j(x_1^{'},\mu) \mathrm{d}\hat{\sigma}_{(ij\to ab)}(x_1, x_1^{'}, \mu) \ . \tag{2.14}$$

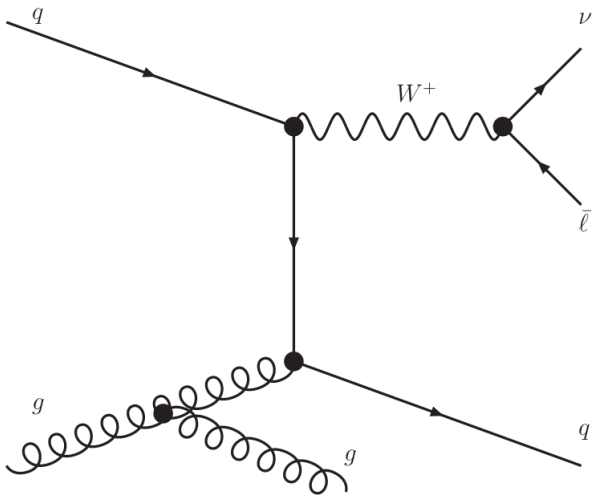

Figure 2.7: Illustration of a Single Parton Scattering [27]. This figure shows the no-MPI process generating the same final state as MPI in Figure 2.6.

This equation is based on the assumption that there are no parton correlations, also called factorisation assumption. This is a very important assumption as it is applied to single interactions where it is assumed that there is no correlation between the two process participants; as well as to the case with MPI where it is assumed that the two interactions are uncorrelated. The sum's indices i, j run over the different parton types in each of the colliding hadrons. The $\mathrm{d}\hat{\sigma}_{(ij\to ab)}(x_1, x_1^{'}, \mu)$ term is a subprocess cross-section which depends on the longitudinal momentum fractions of the two incoming partons x_1 and $x_1^{'}$ and the partonic renormalisation scale μ. In order to calculate the cross-section of a specific process one must also take the probability of merely finding such a parton into consideration. This is done by the $f(x, \mu)$ terms. They are parton density functions and represent the probability of finding the parton in question with a given longitudinal momentum x in a proton. Following a rather phenomenological approach for the description of DPS one now needs the joint probability for finding two partons in a proton $H^{i,k}(x_1, x_2, \mu_A, \mu_B)$. Analogously to before, $H^{i,k}$ represents the probability of finding two partons with specific momenta x_1 and x_2 in a proton while μ_1 and μ_2 are the hard scales of the two hard subprocesses. Only little is known about the joint probability $H^{i,k}$ so assumptions are required in order to proceed. The most common assumption is to assume that the probability function factorises, i.e. assuming the partons are not correlated,

$$H_p^{i,k}(x_1, x_2, \mu_A, \mu_B) = f_p^i(x_1, \mu_A) f_p^k(x_2, \mu_B) \ . \tag{2.15}$$

The partons are now considered as (seemingly) independent, therefore one has to introduce a constraint on the momentum fraction x. Obviously the sum of the momenta of the two partons cannot be larger than the total proton momentum, thus: $x_1 + x_2 \leq 1$. This requirement can be added into the expression for $H_p^{i,k}$ using the Heaviside step function $\Theta(x)$:

$$H_p^{i,k}(x_1, x_2, \mu_A, \mu_B) = f_p^i(x_1, \mu_A) f_p^k(x_2, \mu_B)(1 - x - y)\Theta(1 - x - y) \ . \tag{2.16}$$

The Heaviside step function is defined by

$$\Theta(x) = \begin{cases} 0 & x < 0 \\ 1 & x \geq 1 \ , \end{cases} \tag{2.17}$$

and thus automatically takes care of the momentum constraint. Quite obviously this means that this ansatz only works for small momenta fractions x_1 and x_2 which is fortunately what is expected.
Finally, assuming that the two subprocesses are uncorrelated, the differential DPS cross-section can be expressed as:

$$d\sigma_{Y+Z}^{DPS} = \frac{m}{2\sigma_{eff}} \sum_{i,j,k,l} \int \mathrm{d}x_1 \int \mathrm{d}x_2 \int \mathrm{d}x_1^{'} \int \mathrm{d}x_2^{'} \ H_p^{i,k}(x_1, x_2, \mu_A, \mu_B) \tag{2.18}$$

$$\times H_p^{j,l}(x_1^{'}, x_2^{'}, \mu_A, \mu_B) \mathrm{d}\hat{\sigma}_{i,j}^A(x_1, x_1^{'}, \mu_A) \mathrm{d}\hat{\sigma}_{k,l}^B(x_2, x_2^{'}, \mu_B) \tag{2.19}$$

The additional factor m is a symmetry factor and equals one if the two subprocesses are the same and two otherwise. The indices Y and Z represent the two different systems undergoing the two $2 \to 2$ processes. In this thesis Y stands for the dijet creating process and Z for leptonic process.
The total differential cross-section for a process like the one considered in this study ($Z \to l\bar{l} + 2$ jets) is of course the sum of the two possible processes creating such an outcome,

$$\mathrm{d}\hat{\sigma}_{Y+Z}^{(tot)}(s) = \mathrm{d}\hat{\sigma}_{Y+Z}^{(SPS)}(s) + \mathrm{d}\hat{\sigma}_{Y+Z}^{(DPS)}(s) \ . \tag{2.20}$$

This means the outcome can either originate from DPS or from a single parton scatter accompanied by radiation processes like ISR or FSR. Using the same assumption

used throughout this section, the total cross-section factorises to:

$$\mathrm{d}\hat{\sigma}^{(tot)}_{Y+Z}(s) = \mathrm{d}\hat{\sigma}^{(dir)}_{Y+Z}(s) + \frac{\mathrm{d}\hat{\sigma}_Y(s) \times \mathrm{d}\hat{\sigma}_Z(s)}{\hat{\sigma}_{eff}(s)} \ . \tag{2.21}$$

Rewriting this in a form more suitable for this analysis, the integrated cross section is given by

$$\int_{cuts} \mathrm{d}\hat{\sigma}^{(tot)}_{Y+Z}(s) = \int_{cuts} \mathrm{d}\hat{\sigma}^{(dir)}_{Y+Z}(s) + \frac{1}{\hat{\sigma}_{eff}(s)} \left(\int_{cuts^Y} \mathrm{d}\hat{\sigma}_Y(s) \times \int_{cuts^Z} \mathrm{d}\hat{\sigma}_Z(s) \right) \ . \tag{2.22}$$

In the case of MC simulations there are further aspects to be considered. The so called impact parameter is one of these important aspects. It represents the degree to which the transverse planes (in the order of 1 fm^2) of the two collision partners overlap. Obviously the transverse planes are the important areas since they are the colliding areas. If the impact parameter is large it means the two transverse areas do not overlap much and thus that the probability for MPI is rather small. If, on the other hand, the impact parameter is small it indicates that there is a considerable overlap of the two particles and thus there is a higher probability to observe MPI. There are however some points that remain a concern. Using the factorisation approach introduced earlier one is ignoring (very) possible strong correlations in the longitudinal momenta of partons in the same proton. In recent time it has become an increasing concern if this assumption should remain in use. There have been several studies [28, 29] which argue that it is in fact a false assumption. If future results support this view a new approach or rather a modified approach to the theoretical description of MPI must be found.

Chapter 3

The LHC and the ATLAS Detector

The Large Hadron Collider (LHC) is the world's largest particle accelerator and is situated in Geneva, Switzerland at the border to France as seen in Figure 3.1. It is operated by CERN[1] and houses four major particle detectors, namely ATLAS[2], CMS[3], LHCb[4] and ALICE[5]. The LHC [30] is a ring collider with a circumference of 27 km and is situated about 100 m below the surface in the tunnel formerly used for the Large Electron-Positron Collider (LEP). As of 2012 the LHC runs with a beam energy of $E_{\text{beam}} = 4$ TeV which sums up to a centre of mass (CM) energy of $\sqrt{s} = 8$ TeV. In 2011 the LHC was still running with a center of mass energy of $E_{\text{CMS}} = 7$ TeV, thus $E_{\text{beam}} = 3.5$ TeV per beam. On their way to the detectors the particle beams are transported through the ring in beam pipes (see Figure 3.2). The beam pipes are contained within a cryodipole. The cryodipole is a magnet system that keeps the particle bunches on track on their way around the ring. The particle beams that are eventually brought to collision do not consist of single protons but of so called bunches. Bunches are groups of protons travelling along the beam pipe. By design the distance between the bunches is approximately 7.5 cm. The proton bunches are to consist of about $1.15 \cdot 10^{11}$ protons [31] that travel approximately at the speed of light ($v \approx c$) and follow each other in about 25 ns. On average there are about 25 particle interactions per bunch crossing. The values presented here are design values and can differ during operation. In 2011 [31], the year the data used

[1] CERN = Conseil Européen pour la Recherche Nucléaire
[2] ATLAS = A Toroidal LHC Apparatus
[3] CMS = Compact Muon Solenoid
[4] LHCb = Large Hadron Collider beauty
[5] ALICE = A Large Ion Collider Experiment

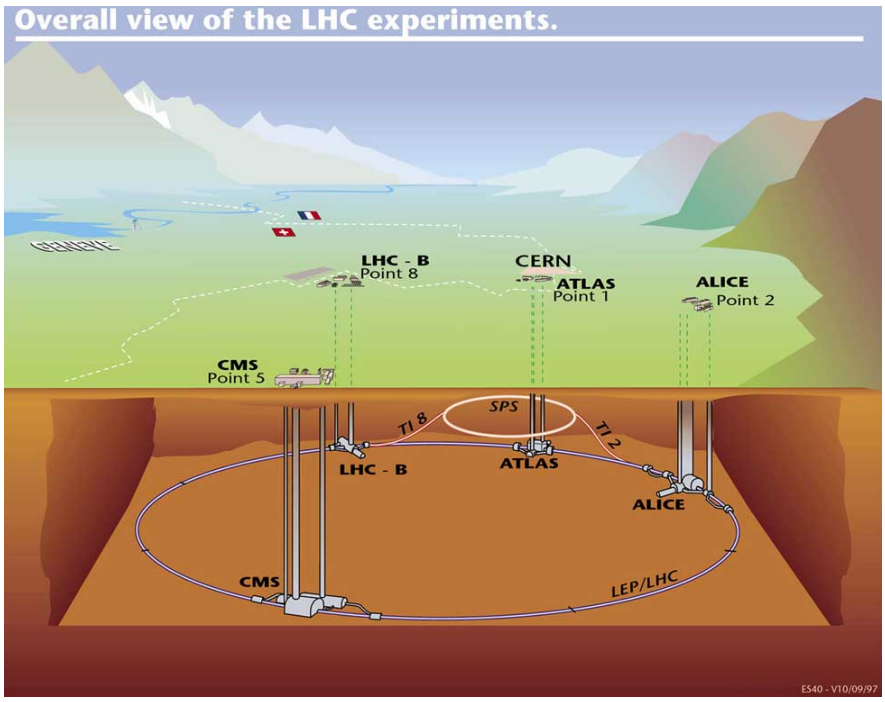

Figure 3.1: Geographical view of the LHC [32] and the participating experiments

in this thesis was recorded, the LHC operated with $1.5 \cdot 10^{11}$ protons per bunch that were separated by 50 ns.

Unfortunately, single protons travelling almost at the speed of light are not readily obtainable. It takes several complicated steps and complex machines to accelerate protons to these velocities (see Figure 3.3). The acceleration process begins with a gas tank filled with H_2 molecules. These molecules are split into single hydrogen atoms and cleared of their electron using an electric field. The electron strapped H_2 molecules (protons) now have to be accelerated almost to the speed of light, unfortunately, it is not possible to do this using a single accelerator, or rather, it is possible but very inconvenient and uneconomical. A linear accelerator, would require an enormously large apparatus which is not very convenient to build. A cyclic accelerator called synchrotron on the other hand keeps the particles on their tracks by inducing a magnetic field and accelerates the particles through an electric field. However, a synchrotron can only operate in a specific range of particle energies, due to the limitations imposed by the magnets and the geometry of the ring. The magnets are limited by the maximum field strength they can exert, while the geometric constraint comes from the curvature of the ring. The solution is to use several different synchrotrons of different size and accelerate the particles gradually. The protons are first accelerated to 50 MeV using the LINAC2. This is a linear

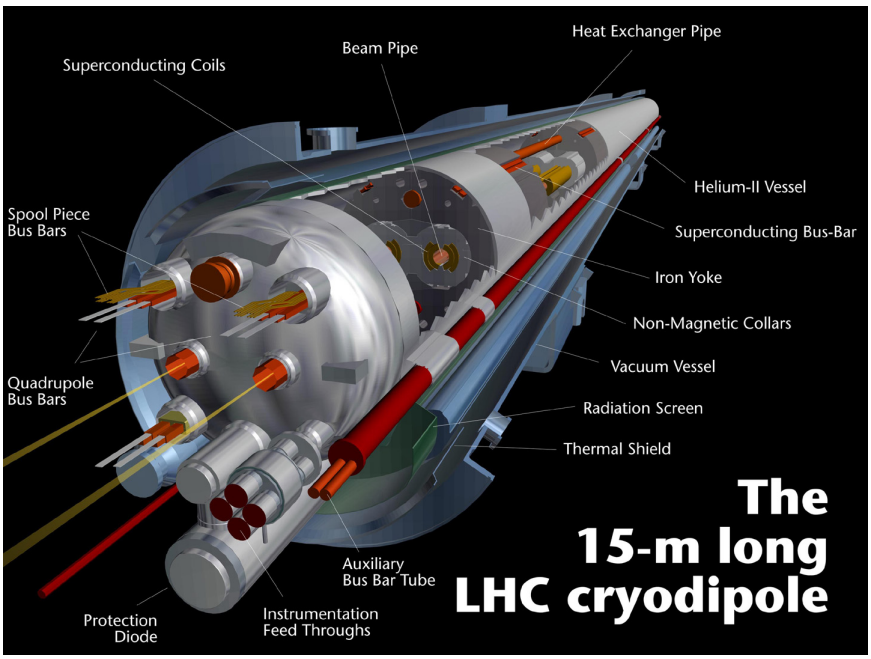

Figure 3.2: The LHC cryodipole [33] carrying the two beam pipes. The cryodipole keeps the protons (yellow beams in the figure) on track on their way around the ring.

accelerator which at the same time bunches the protons into packages. Afterwards they are fed into the PS booster (Proton Synchrotron booster) to further accelerate the bunches to 1.4 GeV whereupon the particles are accelerated to 26 GeV using the PS. Before finally injecting the bunches into the LHC ring the bunches get their final boost to 450 GeV by the Super Proton Synchrotron (SPS). The LHC then does the final job of accelerating the bunches to their designated energy. That was $\sqrt{s} = 7$ TeV in 2011, $\sqrt{s} = 8$ TeV in 2012 and, expectedly, $\sqrt{s} = 14$ TeV in 2014.
In order to estimate the number of particle interactions the detector luminosity is calculated. The LHC is, by design, expected to achieve a luminosity of $\mathcal{L} = 10^{34} \frac{1}{cm^2 s}$ [31]. In 2011 an instantaneous luminosity of $\mathcal{L} = 3.6 \cdot 10^{33} \frac{1}{cm^2 s}$ [31] was reached. It is calculated by

$$\mathcal{L} = n_b \frac{n_1 n_2}{A_{eff}} f \tag{3.1}$$

and describes as such the number of particle, or rather bunch interactions per time and area. Hence, the higher the number of interactions per bunch crossing the larger the luminosity. The luminosity is thus a product of the number of bunches n_b with the number of protons in bunch one n_1 and two n_2. f is the collision frequency and

A_{eff} the effective interaction area, which is given by:

$$A_{eff} = 4\pi\sigma_x\sigma_y \ . \tag{3.2}$$

The σ factors are the standard deviation of the transverse distributions of the interacting beams. In addition, the luminosity can be used to determine the number of expected events in a collider experiment by:

$$\frac{\mathrm{d}N}{\mathrm{d}t} = \mathcal{L}(t) \cdot \sigma_p \tag{3.3}$$

The above introduced luminosity $\mathcal{L}$ is not to be confused with the integrated luminosity L, defined by:

$$\mathrm{L} = \int_{t_0}^{t_1} \mathrm{d}t \ \mathcal{L}(t) \tag{3.4}$$

The integrated luminosity is a measure for the number of interactions happening in a specific time range. High integrated luminosities are eagerly sought after, since it means many interactions were observed and thus, much data was recorded. Since the integrated luminosity L is obtained by integrating the luminosity $\mathcal{L}\left[\frac{1}{cm^2 s}\right]$ over time the unit of the integrated luminosity is obviously an inverse area $\left[\frac{1}{cm^2}\right]$ called (inverse) barn. The beams are collided inside the different detectors along the ring. As mentioned at the beginning of this chapter, there are four major experiments and two smaller ones. The aims of the different experiments are:

- **ALICE**: In this detector heavy ions are collided at up to $\sqrt{s} = 2.76$ TeV. The aim of the examination of these pb-pb collisions is a deeper understanding of a quark gluon plasma (QGP) [35].
- **LHCb**: Through the analysis of bottom quark events, CP violation is measured. This is done to gain a further understanding of the matter-antimatter-asymmetry in the Universe [36].
- **LHCf**[1]: This LHC experiment uses particles generated in the 'forward' (see Chapter 3.1.1) direction to gain a deeper understanding of cosmic radiation [37]. It is also used to gain experience in calibrating particle detectors and the hard interaction models that are used to study cosmic radiation.

[1] LHCf = Large Hadron Collider forward

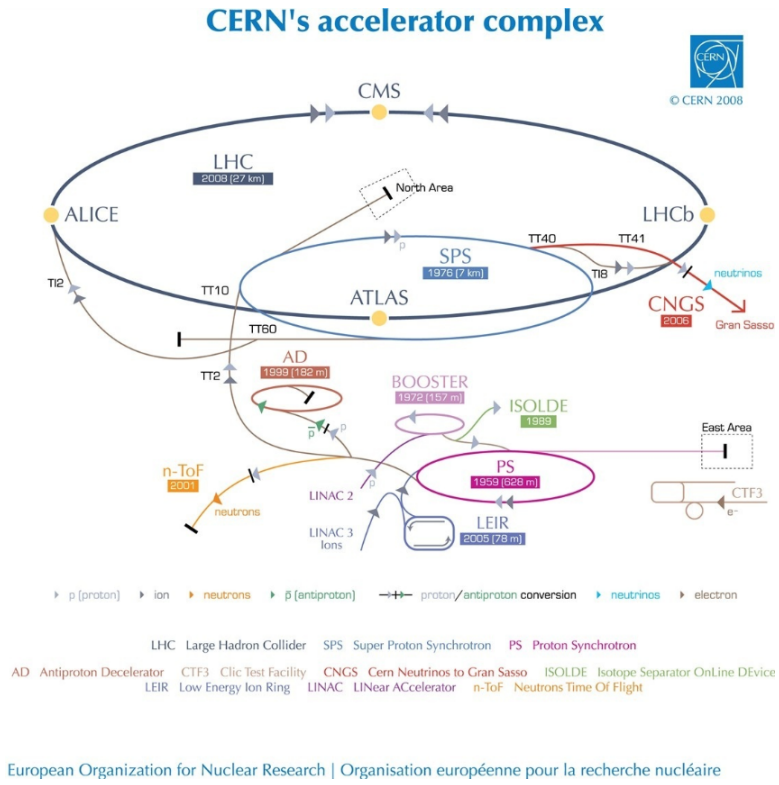

Figure 3.3: Schematic view of CERN's accelerator complex [34]

- **TOTEM**[1]: 'Forward' (see Chapter 3.1.1) particles properties are studied to gain further knowledge about cosmic events. The knowledge gained here is used for the improvement of detector calibrations. Another aim is a precise measurement of the total cross-section in pp collisions [38].
- **MoEDAL**[2]: First deployed in January 2011, the aim of this detector is the search for magnetic monopoles, dyons or other highly ionising stable massive particles (SMP) [39].
- **CMS**: CMS is one of the two general detectors. Its aim is to confirm prevailing physical knowledge as well as exploring new physics [40].

The ATLAS detector is the other universal detector and has been left out here due to its importance for this thesis. It will be introduced in more detail in the following chapter.

[1]TOTEM = TOTal Elastic and diffractive cross-section Measurement
[2]MoEDAL = Monopole and Exotics Detector At the LHC

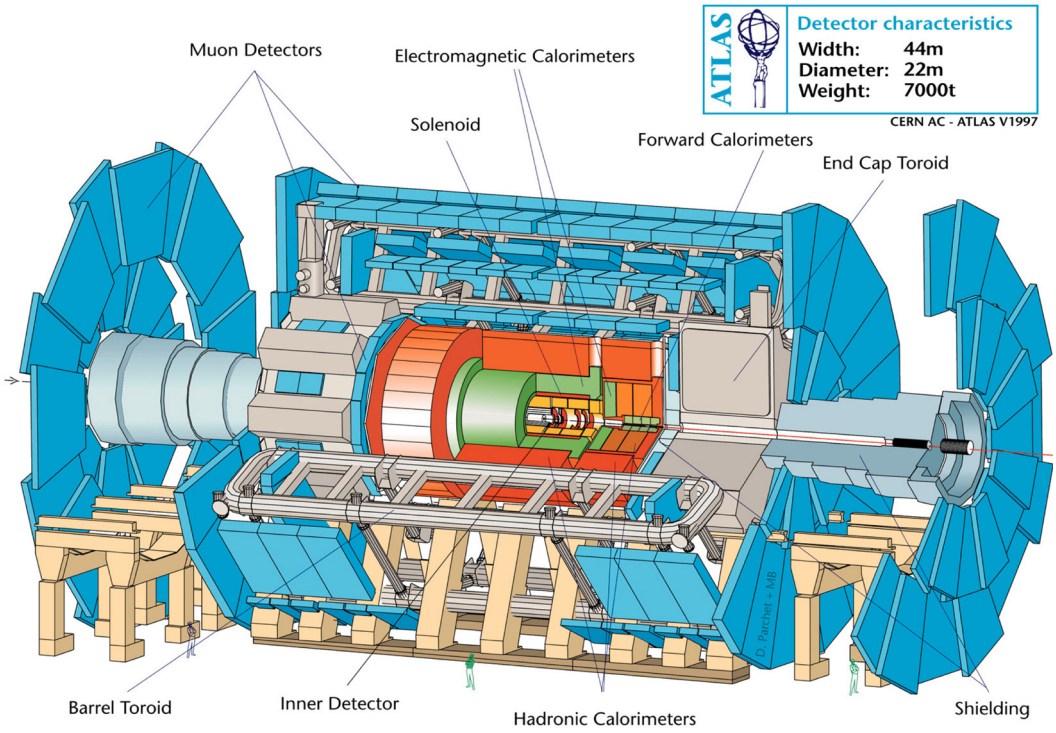

Figure 3.4: Schematic view of the ATLAS Detector [43]

3.1 The ATLAS Detector

The ATLAS detector, as depicted in Figure 3.4, is the largest detector at CERN [41, 42]. It is 44 m long, has a diameter of 22 m and weighs about 7,000 t. The detector consists of a number of sub-detectors performing different jobs.

Moving radially outwards from the collision point (see Figure 3.5), particles first pass the inner detector which is used for particle tracking. Thereafter particles pass the calorimeters. There are two different types of calorimeters - electromagnetic (E-CAL) and hadronic calorimeters (H-CAL). The difference between the two is their aim and therefore their structure. The E-CAL focuses on measuring electromagnetically interacting particles while the H-CAL is aimed at strongly interacting particles. Light particles, like electrons, will thus already get stopped in the E-CAL by depositing all their energy in the calorimeter. Heavier particles, like hadrons, will pass through the electromagnetic calorimeter as they do not deposit much of their energy in the E-CAL. They will however get stopped in the hadronic calorimeter. The last detector is the muon spectrometer. As the name already indicates its task is the identification of muons which are the only identifiable particles that make it

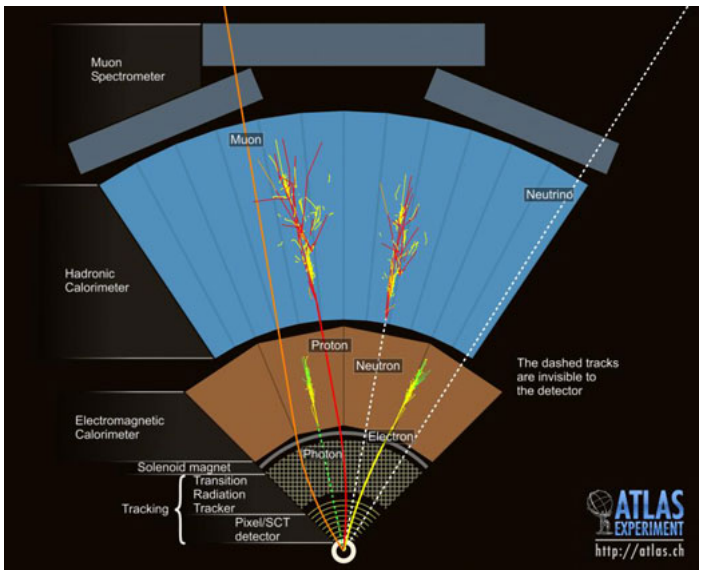

Figure 3.5: Depiction of different particles passing the ATLAS detector outwards in the transverse plane [44]

this far because they hardly interact at all with the detector material in the E-CAL and H-CAL. Nonetheless, there is one group of particles that cannot be detected at all - neutrinos. These particles hardly interact with the detectors due to their physical properties.
The ATLAS detector is constructed as a so called 4π detector which means it covers almost the entire region around the collision point. However, there are limitations preventing the otherwise complete coverage of the region around the interaction point. The coverage region of the inner detector, for example, is already limited by the beam pipe to pseudorapidities $|\eta| < 2.5$.

3.1.1 Detector Specific Definitions

Particle physics uses a very specific coordinate system in order to simplify working in such an environment. The z-axis is aligned along the beam axis while the x-axis points towards the centre of the accelerator ring. Consequently the y-axis points upwards. The $x-y$-plane which is perpendicular to the beam axis stretches out an area called transverse plane. The angle between a vector in the transverse plane and the x-axis is called azimuthal angle ϕ. The x-axis is oriented towards the centre of the LHC ring, thus a vector pointing parallel to the x-axis towards the centre of the LHC ring would have an azimuthal angle $\phi = 0$ with the x-axis. The angle a particle has with the beam axis (z-axis) is called polar angle θ. A plot of the ATLAS

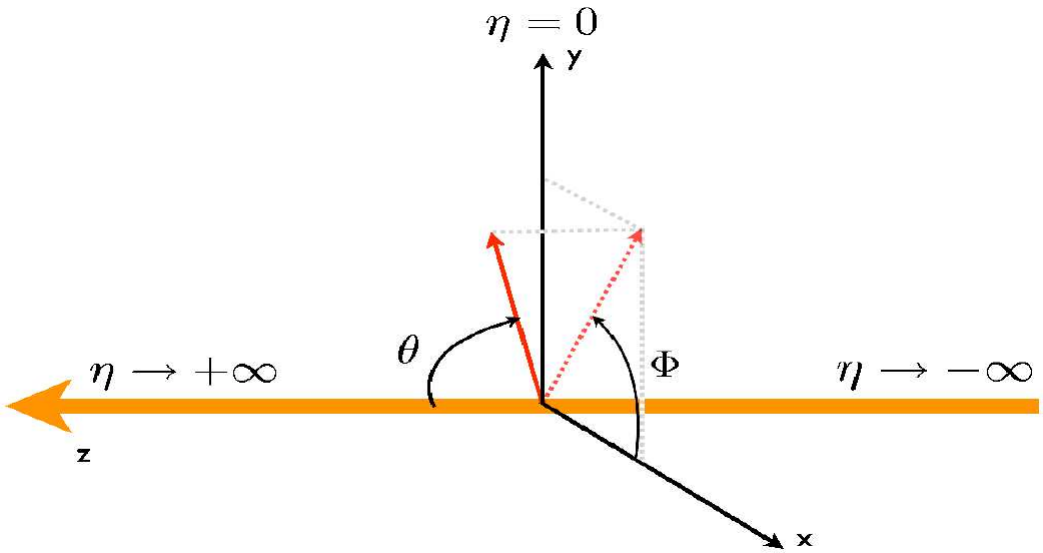

Figure 3.6: Depiction of the ATLAS coordinate system [45]

coordinate system can be seen in Figure 3.6.
In particle physics the polar angle is almost always replaced by a different, more suitable, variable called pseudorapidity η.

$$\eta = -\ln \tan\left(\frac{\theta}{2}\right) \tag{3.5}$$

Replacing the polar angle with pseudorapidity is motivated by the pseudorapidity being invariant under Lorentz boosts. The definition of a so called 'forward' particle is closely connected to the pseudorapidity. 'Forward' particles are particles travelling very close to the beam axis, thus with high pseudorapidites. Using ϕ and η it is possible to define a new variable R which determines the angular separation between two particles.

$$R = \sqrt{(\phi_1 - \phi_2)^2 + (\eta_1 - \eta_2)^2} \tag{3.6}$$

The indices indicate the two particles that are considered. The transverse plane is of considerable significance in particle physics which is why it is useful to define the transverse momentum of particles.

$$p_T = \sqrt{p_x^2 + p_y^2} \tag{3.7}$$

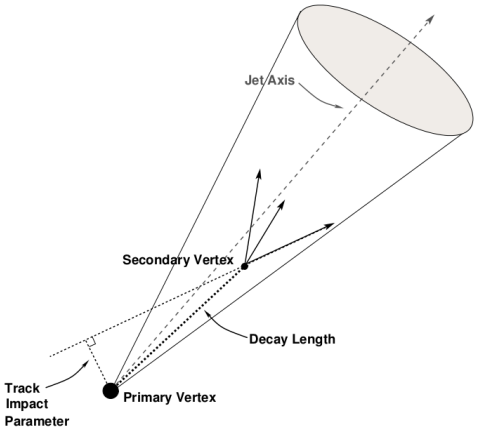

Figure 3.7: Illustration of primary and secondary vertices.

The objects particle detectors are to measure have to originate from a particle physics process, may this be a hard interaction or a radiative process. The point where a particle originates from is called a vertex [46]. There are two different types of vertices - primary and secondary ones (see Figure 3.7). A primary vertex is a vertex created by a hard interaction, thus the charged tracks originating from this vertex will have a high total p_T. Charged Tracks are the trails particles leave in the detectors when traversing them. In principle and especially in cases with a large contribution from multiple proton interactions there can be various primary vertices. In this study however, the primary vertex is considered as the one with the maximal sum of transverse momenta of the charged tracks associated with it. A secondary vertex on the other hand is created by particles decaying in the detector after having already moved some distance (see Figure 3.7).

3.1.2 Inner Detector

The inner detector is the innermost part of the ATLAS detector and has as such a relatively small dimension. Only 7 m long and 2.3 m in diameter does it still provide a vital part of the detection process. Its task is the reconstruction of tracks and vertices, primary and secondary (explained in Chapter 2.5). To gain information as detailed as possible it is important that the inner detector has a high resolution. This is achieved by dividing the inner detector into three components. A pixel detector, a semi-conductor detector (SCT) and finally a transition radiation tracker (TRT) (see Figure 3.8). These three parts composing the inner detector will be explained in more detail in the following subsections. The momentum of the particles passing the inner detector is measured by their bending in the applied 2 T magnetic field

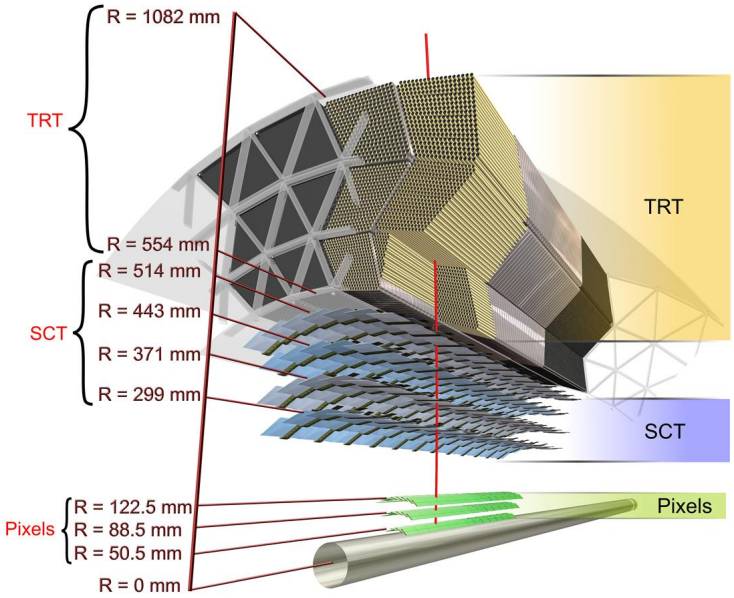

Figure 3.8: Construction view of the inner detector [48]

which is aligned parallel to the beam axis. The magnetic field is exerted by a superconducting solenoid. Per definition the three different sub-detectors together produce 43 space points for each track, 3 from the pixel detector, 4 from the SCT and the remaining 36 from the TRT [47].

The Pixel Detector

The pixel detector is the innermost part of the inner detector and has the highest resolution of the entire detector set-up. It can provide a resolution of (50×400) μm and can be seen as the white part at the very centre of the detector in Figure 3.4 and in Figure 3.8. It consists of three cylindrical layers around the beam axis and two end caps which again consist of three disks. The different layers carry modules which are arrays of pixels. In total there are $1,744$ modules ($1,456$ in the three barrels and 288 modules in the end-caps), each of which has a size of approximately 2×6 cm. These modules further consist of $46,080$ pixels which are read out by 16 readout chips. Each read out chip covers an array of 18×160 pixels [49]. The inner detector's read out channels accout for approximately 50% of the entire experiment's

read out channels. The information gained from the pixel detector is mainly used to determine the positions of vertices.

The Semi-Conductor Detector (SCT)

The SCT [42], which can be seen in Figure 3.4 and Figure 3.8, consists of four coaxial cylindrical layers and two end caps which cover a region of $|\eta| < 2.5$ and $1.4 < |\eta| < 2.5$ respectively. Within this region the SCT provides a space resolution of $(R - \phi) \times z = (17 \times 580)$ μm. It measures charged particles using $15,912$ sensors which are spread out over $4,088$ modules which provide about 6 million readout channels. The working method of the SCT is similar to the pixel detector but uses long, narrow semi-conducting silicon strips instead of pixels. Each silicon strip measures 80μm $\times$ 12cm.

The Transition Radiation Tracker (TRT)

This is the last and outermost component of the inner detector as can be seen in Figure 3.4 and Figure 3.8. As the other sub-detectors it consists of a cylindrical barrel component and two end-caps. The TRT consists of $370,000$ drift straw tubes which are aligned parallel to the beam axis. Each of these tubes is 1.44 m long and 4 mm in diameter [42]. They are filled with a mixture of gases. The main component being Xenon which makes up for 70% of the gas mixture. The other 30% are CO_2 with 27% and O_2 with 3%. If particles traverse a drift tube they will ionise the gas. Since the drift tubes are kept on a potential difference of $-1,500$ V the electrons, which are the results of the ionisation process, will drift towards the wire. Measuring the time it takes the electrons to reach the wire makes it possible to determine their initial distance from the wire, called drift radius. Since there are several layers of drift tubes it is possible to reconstruct the track of a particle using measurements from all the tubes a particle traversed. In total, this detector has about $400,000$ readout channels and covers a region of $|\eta| < 2.0$.

3.1.3 The ATLAS Calorimeters

The calorimeters of the ATLAS detector [50] measure deposited energy. Furthermore, using the measured energy the missing transverse energy $\not{E}_T$ can be calculated. The calorimeters are situated around the inner detector and the solenoid magnets. At the ATLAS detector the calorimeter is split into two parts, an electromagnetic and a hadronic calorimeter. It makes sense to split the calorimeter

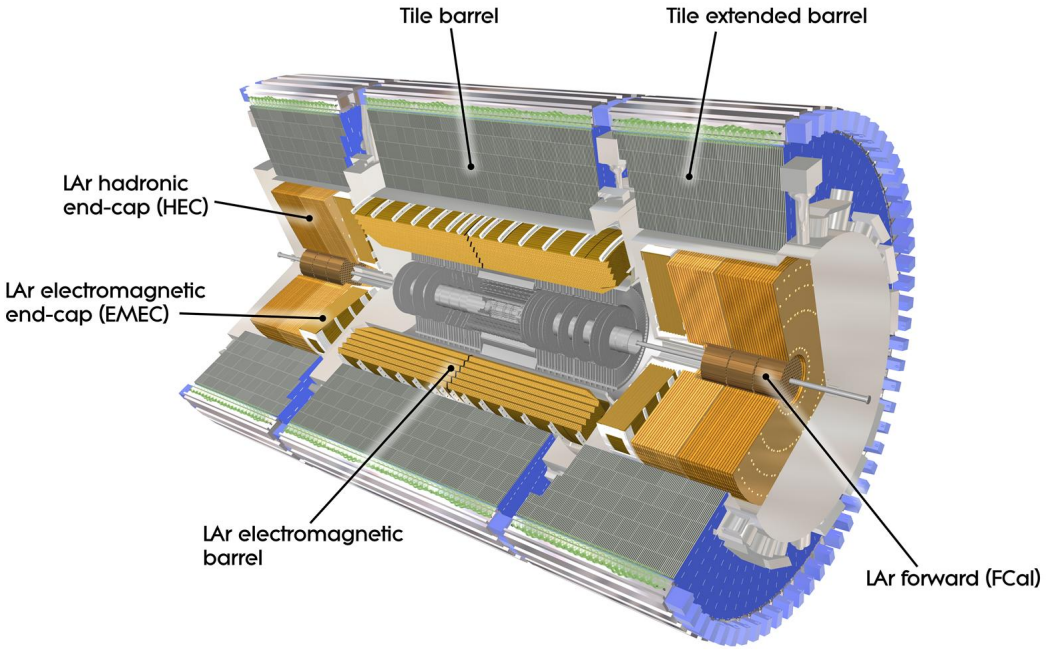

Figure 3.9: A computer generated image of the ATLAS calorimeter [51]

into different components since the various objects created in particle collisions interact differently with the detector material. However, the underlying working principle is in both cases the same. Particles traversing a calorimeter will interact with it and produce a shower of secondary particles which can be measured. In general a calorimeter consists of two alternating parts, an active and and a passive part. This construction method is also called sampling method. It is the active part's task to record all incoming particles and measure their energy while the passive part has to produce the showering process. Therefore the passive part is built of a very dense material like lead in order to provide the best possible shower (development) while the active material is made out of liquid Argon (LAr). Liquid Argon was used as active material due its resistance to radiation.

The Electromagnetic Calorimeter

The electromagnetic calorimeter [42] which is situated closer to the beam line than its hadronic counterpart has the task of identifying and measuring electrons and photons. It does this by stopping traversing particles which is already the motivation

for the thickness of this detector part. Particles that are to be measured in the E-CAL should not pass through the E-CAL but stay contained within it. Thus the thickness of the E-CAL is chosen to be 24 radiation lengths (X_0) for the central E-CAL and $X_0 = 22$ for the end caps. The E-CAL system consists of two main parts. A barrel part which is situated around the inner detector and covers a region of $|\eta| < 1.475$ (LAr el.mag. barrel in Figure 3.9) and two endcap calorimeters covering $1.375 < |\eta| < 3.2$ (EMEC in Figure 3.9). The endcaps and the barrel part are both constructed of alternating layers of active and passive material which are combined into an accordion like shape. This construction method allows a full ϕ detector coverage independent of a particle's angle of incidence.
The central E-CAL region is split into three parts. For physical and technical reasons the layers are built up of smaller cells ($\Delta\eta \times \Delta\phi$) with different granularity in the different layers. The first layer has a very fine segmentation ($\Delta\eta \times \Delta\phi = 0.0031 \times 0.098$) which also makes it possible to distinguish between prompt photons and photons produced in pion decay processes ($\pi^0 \to \gamma\gamma$). The second layer has a granularity of $\Delta\eta \times \Delta\phi = 0.025 \times 0.025$ and a depth of 10 radiation lengths. It is this second layer where the particles that are to be measured in the E-CAL deposit most of their energy. The third and last layer part is to collect the remaining tails of the electromagnetic shower. It is the least segmented detector part ($\Delta\eta \times \Delta\phi = 0.05 \times 0.025$) with a thickness of only $X_0 = 2$. Before particles enter the calorimeter however they pass a presampler covering $|\eta| < 1.8$. It corrects particle properties for energy losses they experienced when passing through the inner detector, the cryostats and the solenoid before reaching the calorimeter.
Electrons entering the E-CAL interact with the electric field of the nuclei in the passive material. They become diverted from their incoming direction and emit a photon as a result of this ($e^- \to e^- + \gamma$). Since this could also be interpreted as slowing down electrons the process is called Bremsstrahlung. This process repeats itself until there is not enough energy left for further bremsstrahlung processes. Photons on the other hand are dominated by pair production processes ($\gamma \to e^- e^+$).

The Hadronic Calorimeter

It is the hadronic calorimeter's (H-CAL) task to measure and identify particles that interact through the strong force. The particles of concern for the H-CAL, hadrons (jets), are measured by stopping them, which is the same way particle properties are measured in the E-CAL. The H-CAL can cover a total region of $|\eta| < 4.9$ but is split into smaller sub-detectors. One of these sub-detectors covers the central barrel region $|\eta| < 1.7$ however, this sub-detector is itself again split into three components, a central tile calorimeter covering $|\eta| < 1.0$ and an extended tile barrel on each side of the central tile calorimeter covering $0.8 < |\eta| < 1.7$ (see Figure 3.9). As mentioned

earlier the working principle of the H-CAL is similar to the E-CAL however, it does use some different materials. The main barrel tile calorimeter uses steel as absorber material instead of lead as in the E-CAL. These (passive) absorbers alternate with the active parts which are scintillator tiles. Aside from the barrel calorimeter there are also two end-cap calorimeters called LAr hadronic end-cap (HEC) and LAr forward (FCal) (HEC and FCal in Figure 3.9) which cover the region $1.5 < |\eta| < 3.2$. Both of them are constructed of alternating active and passive layers. Furthermore, both of them also use liquid Argon as sampling material. They do however differ in their choice of the passive material. In case of the HEC copper is used while the FCal uses copper and tungsten. The HEC covers a region of $1.5 < |\eta| < 3.2$ but shows different granularities within this range. In the region of $1.5 < |\eta| < 2.5$, $\Delta\eta \times \Delta\phi = 0.1 \times 0.1$ while between $2.5 < |\eta| < 3.1$ a lower granularity is sufficient $\Delta\eta \times \Delta\phi = 0.2 \times 0.2$. The forward calorimeter covers $3.1 < |\eta| < 4.9$. It covers such a large region because the H-CAL is also used in the determination of missing energy $\not{E}_T$. For such a measurement no (measurable) energy must escape the detector undetected, thus the large range.
The processes generating the particle shower are not, as in the case of the E-CAL, produced by the electromagnetic force but the strong force. Particles interact directly with the nuclei of the detector material via inelastic scattering. The working principle of the H-CAL is more complicated than the E-CAL due to the higher number of possibly occurring processes.

3.1.4 Muon Spectrometer

The outermost and largest part of the ATLAS detector is the muon spectrometer [42] (see Figure 3.10). Its sole task is the identification and precise measurement of muons. Muons are minimal ionising particles and as such they hardly interact with the calorimeters. That is the reason why an entire sub-detector is required for them. The muon spectrometer is situated in a toroidal magnetic field with a strength of 2 T. The magnetic field is used to bend the muon trajectories as they pass through the spectrometer. The recorded trajectories are then used for the measurement of the muon's momentum in a region up to $|\eta| < 2.7$.
The spectrometer consists of four parts: Monitored drift tubes (MDT), cathode strip chambers (CSC), resistive plate chambers (RPC) and thin gap chambers (TGC). MDTs and CSCs are mainly used for precision measurements while the RPCs and the TGCs are part of the Level1 muon trigger system. A trigger is used to make rapid decisions about which events are to be recorded and which not. However, the RPCs and TGCs are also used to measure the muon momentum perpendicular to the transverse momentum measured by the MDTs and CSCs.

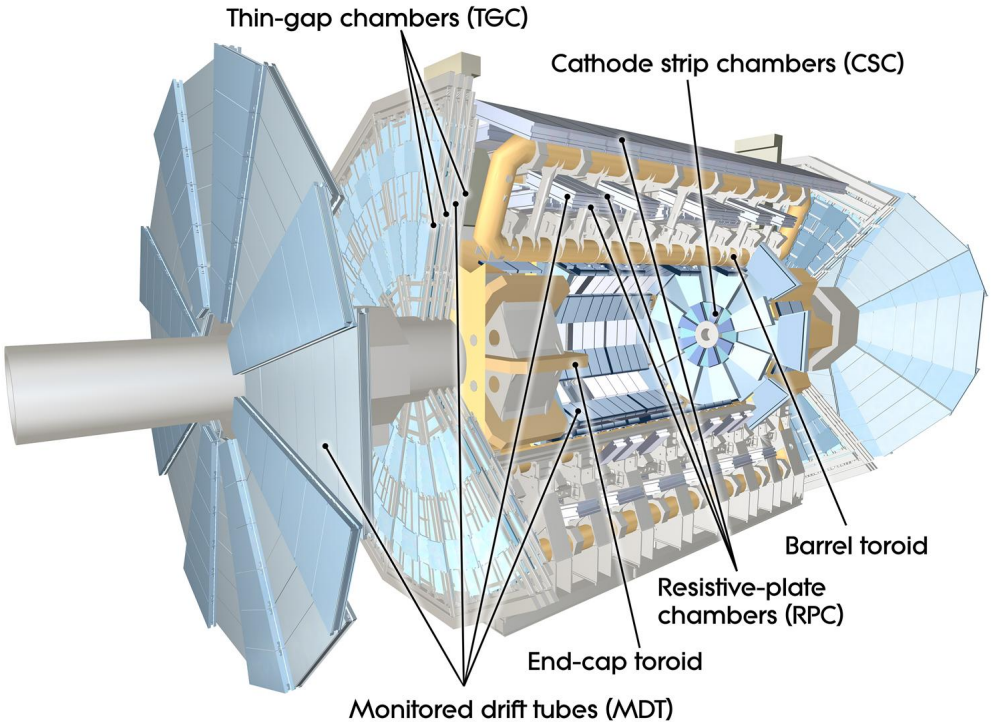

Figure 3.10: Schematic view of the ATLAS muon spectrometer [52]

3.2 Object Reconstruction

Particle detectors cannot record pure physical processes. For one thing because many of the occurring processes happen so fast that they cannot be recorded technically but what the detector can record are final state particles like hadrons and leptons (see Figure 3.5). Of course the real data by itself cannot identify particles. This is why object reconstruction algorithms are necessary in particle physics experiments to interpret the raw data. Each particle interacts differently with the different detector components. In the end the gathered data of each sub-detector are taken and put together with the data from the other sub-detectors. Different algorithms are used to combine and interpret (in terms of reconstruct objects) the collected data.
In this section some important algorithms will be presented. Since reconstruction and identification algorithms are by no means trivial procedures there exist several different approaches. The focus here will be on the algorithms used in this study.

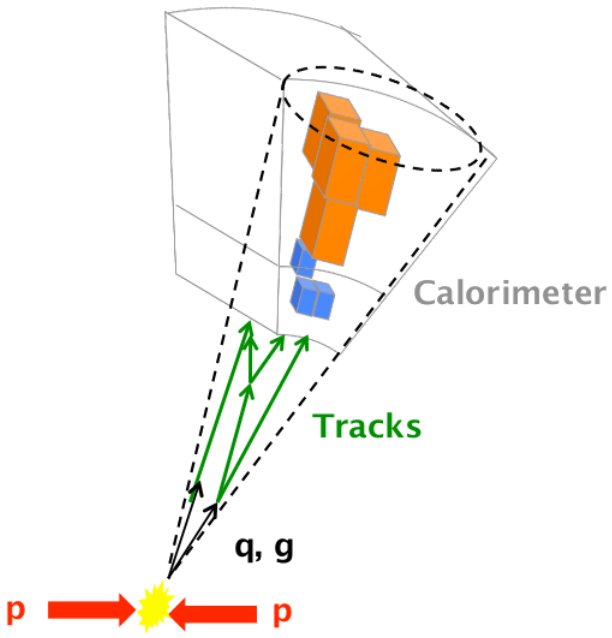

Figure 3.11: Schematic depiction of a jet; The jet being the content of the black cone [53]

3.2.1 Jets

Jets are not elementary particles, like leptons for example, but artificial products. Electrons for example have lifetime that is long enough to detect them directly while this is not possible in the case of quarks due to their colour confinement. If partons are produced after a hard interaction (e.g. $gg \to g \to q\bar{q}$) they will move away from the interaction point and hadronise on their way. The particles created in this process will be boosted roughly in the direction of the parent parton, so that in end a group of particles moves in (roughly) the same direction. These particles can be summarised into a single object called jet (see Figure 3.11).

In principle, jet algorithms come in two different types. There are cone and cluster algorithms. Cone algorithms are rather simple algorithms following the idea that a jet ideally looks and evolves like a cone (see Figure 3.11). To find jets they usually begin by creating a list of proto-jets which usually are objects with a transverse momentum p_T above some threshold (seed) energy. Starting from the highest p_T proto-jet, a cone with a predefined opening radius R is constructed around it to create the first jet. It is very probable that the highest p_T proto-jet does not define the centre of the jet, the constructed jet could thus neglect important objects that

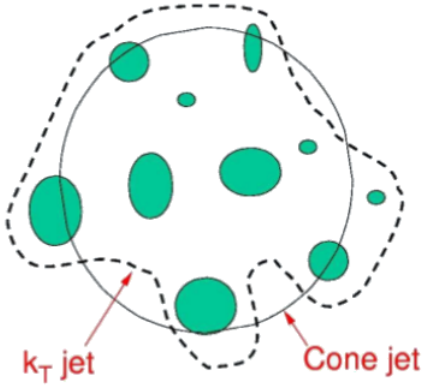

Figure 3.12: Depiction of cone and k_T-jet algorithm. It shows a situation where a cone algorithm constructs a jet but misses some relevant information due to the fixed opening radius of the cone. The k_T algorithm's approach is more complex and introduced in Chapter 3.2.1.

contribute to the jet. To avoid this, after the first version of the jet was created an E_T weighted centre is calculated and a new cone around the new centre is constructed. This step is repeated until the jet centre is stable and does not change any more. These jet creation steps are then repeated for all other proto-jets as well. At the end, after all proto-jets have been transformed into real jets, it can happen that jets are overlapping. There is no built-in method to avoid this, therefore in a last step overlapping jets either have to be merged together or split into two separate jets.
Cone algorithms do however have some weak spots. For one thing, cone algorithms are purely driven by geometry. This can lead to the situation where the algorithm creates a jet that neglects some of the information that actually belongs to the jet (see Figure 3.12). Furthermore, in the basic version cone algorithms are not infrared safe, which means that the emission of an infinitely soft parton changes the number of detected jet (see Figure 3.13 (left)). Another cause of concern, which can be seen on the right in Figure 3.13, is called collinear safety. The absence of it describes the case when the splitting of a proto-jet into two collinear jets causes the algorithm to ignore it because neither of the two new proto-jets surpasses the threshold.

There are methods to improve several of the mentioned drawbacks (e.g. SIS-cone algorithm), but since cluster algorithms were used in this study an in depth description of these algorithms will be omitted.
Cluster algorithms like the k_T algorithm work by pairwise grouping nearby objects

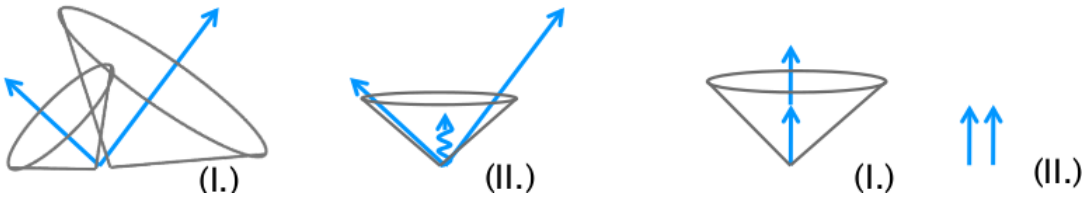

Figure 3.13: Left: Infrared safety; Right: Collinear safety [53]

first. Alternatively the grouping can also be done by grouping highest p_T objects first [54]. Pre-grouping objects to potential jets has some distinct advantages. Objects are now uniquely associated to their jet. This means that there is no need to take care of splitting or merging jets since there are no overlapping jets.
The Anti-k_T jet algorithm is the one used in this study, therefore an overview of the working principles of the algorithm will follow. The algorithm is a further development of the k_T jet algorithm and the Cambridge/Aachen algorithm. The algorithm begins by calculating the distances between all reconstructed tracks d_{ij} and the distances between track i and beam B, d_{iB} [54]

$$\begin{aligned} d_{ij} &= \min(k_{t_i}^{2p}, k_{t_j}^{2p}) \frac{\Delta_{ij}^2}{R^2} \ , \\ d_{iB} &= k_{t_i}^{2p} \ . \end{aligned} \tag{3.8}$$

where $\Delta_{ij}^2 = \Delta\phi^2 + \Delta y^2$. The factors k_{t_i} and k_{t_j} are the transverse momenta of the two particles and R is the radius parameter. The algorithm repeatedly calls the above equations and minimises the distances. If d_{ij} is the minimum the two objects are considered very close to each other and are thus merged together. If the minimum is d_{iB}, i is turned into a jet and removed from the list of particles and pseudojets because it means there are no more particles nearby that could sensibly be merged together with this object. These steps are repeated until all objects are contained within one of the resulting jets.
The parameter p in equation 3.8 is equal to minus one in the case of the Anti-k_T algorithm. When $p = 0$ or $p > 1$ the equations describe the Cambridge/Aachen and the usual k_T algorithm respectively.

3.2.2 Electrons

Electrons are identified by a method that uses information from the inner detector (ID) and the electromagnetic calorimeter (E-Cal). The method is called Calorimeter-seeded reconstruction [55]. As the name already indicates, at the beginning E-Cal

	Muon type		
	Standalone muons	Combined muons	Tagged muons
Staco family	Muonboy	Staco	MuTag
MuID family	Moore	MuID	MuGirl

Table 3.1: Muon reconstruction algorithms with respect to their family [57]

clusters with an energy of approximately 3 GeV are identified as potential electrons. Secondly a potential cluster is matched with tracks in the inner detector. Since there are always several different tracks the track that minimises $\Delta R = \sqrt{\Delta\phi^2 + \Delta\eta^2}$ is chosen to be the correct match. At a $E_T > 20$ GeV and within the coverage region of the inner detector ($|\eta| < 2.5$), approximately 93% of true electrons are selected as electron candidates.
Since only E-Cal clusters and ID-tracks are used for the reconstruction, it can also happen that other particles (e.g. jets) are falsely identified as electrons because their signatures in the detectors are similar. Misidentification can be avoided or at least reduced by using a cut-based method. Depending on how stringent the selection should be there are three methods provided. These methods apply loose, medium or tight cuts, which mainly concern the shape of the cluster and the quality of the ID-track. The reason for the different methods is that the cuts will of course also remove real electrons which might reduce the identification efficiency to an intolerable level.

3.2.3 Muons

Muons can be identified in three different ways [56]. Either as standalone, combined or tagged muons. The first type only uses the information from the muon spectrometer which is then extrapolated back to the beamline. In the case of tagged muons the inner detector tracks the muons leave are matched with calorimeter information. The method used in this study is the one for combined muons. In this case, the signatures the muons leave in the muon spectrometer are combined with the tracks that are left in the inner detector. For the reconstruction of the different types of muons there exist two main groups of algorithms. They are called Staco and MuID (Muon identification). Each of them provides a separate algorithm for each muon type (see Table 3.1).

Both algorithm groups show very similar performance in terms of reconstructing efficiency. There are however some small differences. Both algorithms show a drop in reconstruction efficiency for combined muons as compared to standalone muons while the fake rate also decreases. The fake rate is the rate at which other par-

ticles are falsely identified as muons. While both algorithms behave similarly for low transverse momenta, MuID does perform better than Staco for high transverse momenta in terms of fake rate reduction. At the same time MuID's efficiency is worse than Staco's in $t\bar{t}$ events. In this thesis MuID and thus combined muons are chosen since the algorithm for combined muons shows the best performance. MuID works much better than Moore for transverse momenta $p_T < 15$ GeV and better than MuGirl. MuGirl provides a lower efficiency and higher fake rates than MuID. MuID was preferred over Staco since it provides a slightly better performance (in terms of fake rate reduction). Of course, it is at the same time worse than Staco in $t\bar{t}$ events but this is acceptable since this study is not concerned with top quarks.
The MuID algorithm works by first reconstructing potential muons in the inner detector using a method called Moore. These tracks are then combined with the muon's hits in the muon spectrometer using a full track refit. This combination improves the transverse momentum resolution of the muons so that they fulfill all of ATLAS' physics requirements. At common muon energies, between 10 GeV and 100 GeV (at least in hard scatterings), the algorithm works with a precision of $2 - 3\%$. However, because of the coverage area of the inner detector, which is used by MuID, the algorithm can only work in a pseudorapidity range of $|\eta| < 2.5$.

Chapter 4

Monte Carlo Simulations

Monte Carlo simulations take a vital role in particle physics. They make it possible to compare experimental results with theoretical predictions in particle physics experiments. In general most Monte Carlo generators take a similar approach to describing particle collisions and the subsequent processes. There are four important aspects in the simulation of particle physics processes using Monte Carlo models. A schematic view of a particle collision and subsequent processes can be seen in Figure 4.1. Moving outwards from the collision point, the first thing that matters is the hard scattering process. The partons participating in the hard scattering process are, in the case of a pp collision, constituents of the proton. Parton distribution functions (pdf) describe the probability of finding a specific parton with a given longitudinal momentum in a proton. Thus, the pdfs describe the probability for a parton to participate in the hard scattering process. They are introduced in Chapter 4.2 and are illustrated as $f_{i,p}(x, \mu^2)$ in Figure 4.1. The hard scatter is a clearly perturbative process with an energy scale of usually several GeV. It is described by the matrix element corresponding to the hard process (see 'ME' in Figure 4.1). Since the matrix element can only describe the hard scattering, the succeeding processes are described by a parton shower (see 'PS' in Figure 4.1). The parton shower consists of processes like final state radiation where particles emit further particles (e.g. a quark emitting a gluon). To be precise, this order is not entirely correct. Even before the hard scatter radiation processes like initial state radiation can occur. They are as well described by the showering model. However, this order - hard scattering before showering model - was chosen as the hard scattering process can be considered as the starting point of the main process. Following the parton shower many particles exist as forbidden, coloured states. Real physics takes care of this by turning those particles into colour neutral composite states. The simulation of this process part is done by fragmentation models (see 'HADRONIZATION' in

Figure 4.1) which are briefly described in Chapter 4.4. Many of the newly formed hadrons will be instable. Thus, the final step is called hadron decay. It decays instable hadrons until all hadrons are stable. The hadron decay process is not depicted in Figure 4.1 but would succeed the hadronisation.
It has been outlined above that several different steps are required to simulate a particle collision. A single method describing the entire particle collision is not available since a particle collision includes various physical processes, some being perturbatively calculable while other processes cannot be described perturbatively. This is why a combination of perturbative calculations and phenomenological models has to be used to describe an entire particle collision. The innermost part - the collision process - can be described by perturbation theory due to the prevailing very high energy scales [58]. As distances increase after the hard interaction and thus moving to different energy scales, the occurring processes cannot simply be described by perturbtive QCD (pQCD) any longer. The finite divergences at the hard scale now become finite and thus have to be accounted for. These finite remainders enter every term of the perturbative series and thus prevent it from converging. Previously this was guaranteed due to the very small nature of the coupling constant. In order to recover convergence the higher orders in the perturbative series must be resummed. An easy and convenient way to perform the resummation is to use a numerical method called parton shower (see 'PS' in Figure 4.1). This method is widely used in Monte Carlo generators. However, for the sake of completeness it should be added that the resummation can also be done analytically. As described earlier, the parton shower is followed by the hadronisation process which can be connected to the parton shower. However, moving from the energy scale of the parton shower to the hadronisation scale, pQCD breaks down. Therefore completely phenomenological models have to be used to describe this part of the collision process. Two of these models will be described in Chapter 4.4. Finally, the hadron decays are usually simulated by effective theories and simple symmetry arguments.
In the following some crucial parts of the simulation process will be outlined.

4.1 Monte Carlo Generators

MC generators [59, 60] (also called event generators) are computer programs written to simulate high energy physics experiments. They are needed to compare real physics data as recorded by particle detectors with theoretical predictions, which are implemented in the MC generators. Furthermore, MC simulations are also used to design the particle detectors and to determine a suitable approach to conducting physics analysis with real data. Event generators exist for various different processes, like heavy ion events or neutrino events. In this thesis however, the focus is

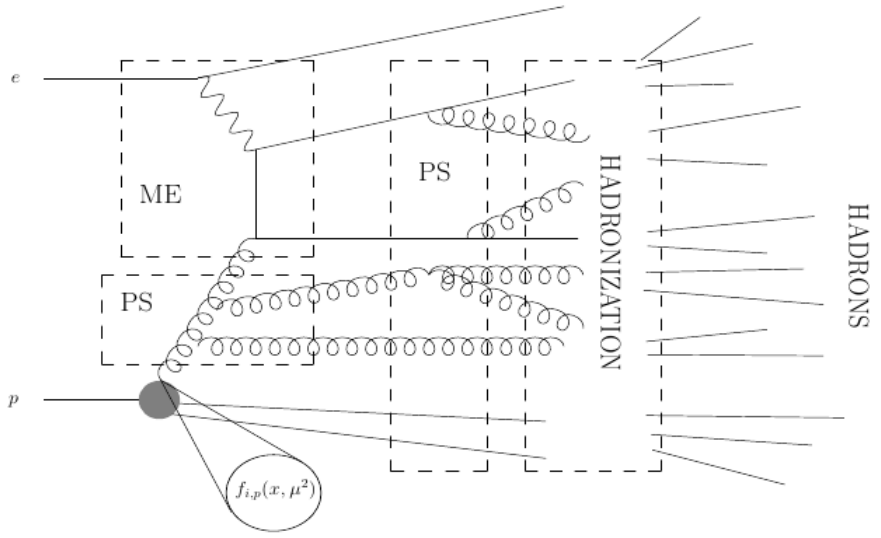

Figure 4.1: Depiction of a particle collision with indications of the corresponding simulation processes. The function $f_{i,p}(x, \mu^2)$ is the parton distribution function, ME = Matrix element; PS = Parton shower; $f_{i,p}$ standing for the parton distribution function (see Chapter 2.5)

on hadron scattering processes, i.e. the simulation of pp collisions. The aim of these event generators is to simulate a proton-proton collision and all subsequent processes as accurately as possible. To do this the generators use a mixture of perturbation theory calculations and phenomenological models. These were already introduced in Chapter 4.
In order to make the output generated be the simulations intelligible, reconstruction algorithms have to be applied. These algorithms identify and determine the properties of objects created in the simulation. The tools used for reconstructing objects is the same as used in the reconstruction of objects in real data.
Monte Carlo simulations alone produce the real physics particle spectrum, i.e. the spectrum a perfect detector would record. At this point detector influences have not been accounted for. Detector simulations are available, however, they require very much time (in the order of one hour per event). The most notable detector simulation program is arguably *Geant*4 [61]. Nevertheless, it must be kept in mind that these MC generators are not only influenced by physical effects but also by technical effects, like computing related limitations.
Over time several different event generators have been developed. Two of them, Pythia and Sherpa, will be used in this thesis to perform the necessary simulations. These two generators will briefly be introduced in the following two subsections.

4.1.1 Pythia

Pythia is arguably the most prominent MC generator. The first version, version 6 [62], was still written in FORTRAN, while the most recent version, version 8 [63], is now written in C++. Pythia8 is the version used in this thesis. It is a general purpose generator that simulate pp, $p\bar{p}$-collisions as well as ep and e^+e^--collisions. The hard interaction is calculated by using leading order (LO) matrix element calculations. Hard parton-parton interaction are simulated down to a scale of $Q = 2$ GeV. Below this scale perturbative calculations are not possible any more due to colour screening effects. The subsequent parton showering process is called dipole showering as opposed to the formerly used virtuality ordered showering process. It is also responsible for initial and final state radiation. Pythia8 uses CKKW-L merging to connect the matrix element with the parton shower. The working method of CKKW-L matching will be explained in Chapter 4.3. The hadronisation model implemented in Pythia8 is called the Lund String model and will be discussed in the corresponding section of Chapter 4.4. The underlying event is simulated by separate $2 \to 2$ scattering processes in LO matrix elements. Pythia8 provides a large variety of switches to adjust the parameters required and used in the process simulation. Several groups and people work on describing real physics data as accurately as possible by adjusting those switches. Notable contributors are in this respect Rick Fields [64] or Peter Z. Skands developing the Perugia tunes [65].

4.1.2 Sherpa

In the long list of MC generators, Sherpa [66] is the most recent one and was written, from scratch, in C++. It can simulate $2 \to 2$ as well as $2 \to N$ events in lepton-lepton collisions and hadron-hadron collisions by using inclusive calculations of matrix elements. It also provides methods for describing the parton shower and the hadronisation process. The parton shower and the hadronisation are merged together by CKKW merging (introduced in Chapter 4.3). The hadronisation itself is simulated by cluster fragmentation (see Chapter 4.4). The description of multiple parton interactions is based on Pythia's implementation, does however show some differences.

4.2 Parton Distribution Functions (PDFs)

To describe proton-proton collisions accurately it is of vital importance for physics analysis to know which particles actually do interact with each other. To determine

their nature on a statistical level parton distribution functions (pdf) are used. They represent the probability to find a specific parton in the proton with a given longitudinal momentum fraction $|x|$ (see Figure 4.2). The pdfs cannot be calculated perturbatively since they include long-distance factors which are not perturbatively calculable. Several different collaborations, like CTEQ [67], MSTW [68], NNPDF [69] or HERAPDF [70], work on determining pdfs by using experimental results which are recorded by different experiments and different experiments (like DESY, CERN, Fermilab). Figure 4.2 depicts the pdfs for various different quark types and the gluons. The plot shows the probability density of finding a specific parton, like a quark or a gluon, with a specific longitudinal momentum fraction x at some energy scale Q^2 (in Figure 4.2 for example 10 GeV). It can clearly be seen that at small longitudinal momenta the gluon contribution dominates; while at larger x values especially the valence quark contribution grows, even dominates. Partons in a proton usually do not have large longitudinal momentum fractions x. Especially when going to higher energies x decreases. This also explains why the LHC is sometimes referred to as a gluon collider. The higher the energy gets the smaller x becomes or expressed differently at LHC energies of 7 TeV an $x = 0.01$ would require the parton in the proton to have a longitudinal momentum of $0.01 \cdot 7$ TeV $= 700$ GeV. From this point on, the proton's valence quarks would become dominant however, requiring these quarks to have even higher longitudinal momenta.
In order to compare the data recorded by the ATLAS detector with theoretical predictions, event generators (also called Monte Carlo generators) are used. These are computer programs aiming at simulating particle collisions based on theoretical and phenomenological knowledge of particle physics. PDFs are thus a very important part of all event generators since they influence the process to be simulated.

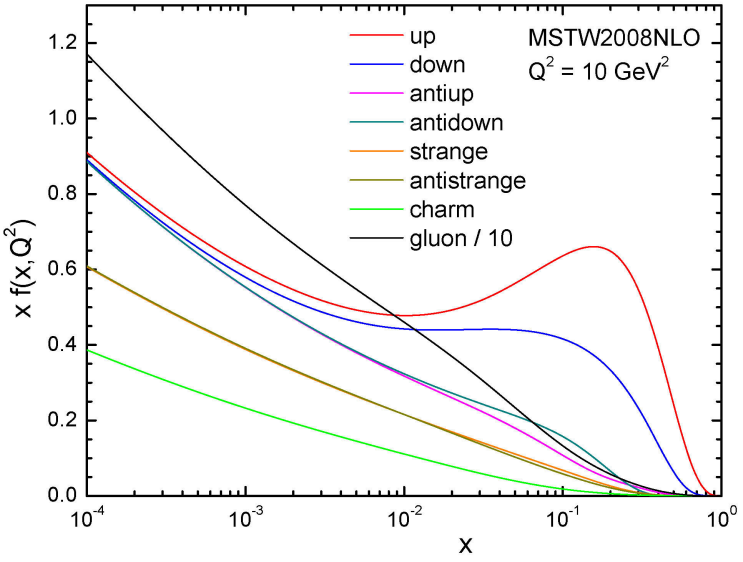

Figure 4.2: Illustration of the parton density functions generated by the MSTW collaboration; MSTW2008NLO [71]; The property on the x-axis x is the longitudinal momentum of a parton. The y-axis shows the probability density of finding one of the partons in the figure.

4.3 Merging Algorithms

As described at the beginning of Chapter 4, the primary $2 \to N$ hard collision is described by using matrix elements. They are good at describing high-p_T processes. Unfortunately, matrix element calculations become very complex at high particle multiplicites. For the parton showers (see 'PS' in Figure 4.1) on the other hand the complexity does not increase as much with the particle multiplicity as for the matrix element. This is because the branching probability is evaluated separately for every particle. Additionally, due to the leading-log approximation of the parton shower, does it deliver good results for smaller transverse momenta. It can thus be seen that the matrix elements and the parton shower complement each other very well. To achieve a good overall description of collision processes and their evolution both are merged together. These algorithms that connect the ME and the PS are therefore called merging algorithms. It is their task to take the results the ME produces and hand them over to the PS. However, overlapping phase space regions where both the ME and the PS return results complicate the merging procedure. A major problem of overlapping phase space regions is that particles can potentially be double counted

(double counting problem). To avoid the problem of double counting the matrix elements are reweighed by the running of the coupling constants and Sudakov form factors. The general approach to jet merging can be summarised in the following four steps [72]:

1. A matching scale Q_0 and a jet algorithm (for example the k_T algorithm) is defined. Then all relevant cross-sections including jets are calculated using matrix elements. For example, for a process with a specific final state X this would mean that all cross-sections for $pp \to X + n$ jets are calculated $(n = 0, 1, 2, \ldots)$.

2. A hard parton configuration is produced based on the contribution of the $X+n$ jets to the total cross-section. The corresponding kinematic configuration is calculated from the matrix element.

3. The selected parton configuration is accepted or rejected with a certain probability. The probability is based on the running of the coupling constant and Sudakov-type suppressions. In case the particle configuration is rejected step two is repeated and a different parton configuration, probably with a different number of jets, is selected.

4. Finally, starting from the chosen parton configuration, the parton shower using suitable initial conditions is performed. This is done separately for each leg. In all cases the parton shower must not produce any additional jets. Any configuration that would have to be calculated with matrix elements due to different number of jets is forbidden, meaning emissions above the matching scale Q_0 are forbidden.

Several methods are available to avoid this, however in the following only two methods will be introduced, namely those important in the generators used in this study. That is, CKKW matching in Sherpa [66] and a CKKW-L approach in Pythia [73]. Both algorithms have been extensively checked at the LEP [74, 75], the Tevatron and the LHC [74, 76]. Evaluations and comparisons of CKKW, CKKW-L and others (like MLM matching) have shown that CKKW-L shows the best performance.

4.3.1 CKKW Matching

In principle CKKW matching [72, 76, 77, 78] uses the matrix element and the parton shower exactly for what they are good at. It uses the matrix element for large transverse momenta and angles and the parton shower for small transverse momenta and small angles. The phase space separation between the PS and the

ME is done by introducing a new scale, the resolution scale. The CKKW merging algorithm in particular has initially been used for e^+e^- collisions and has been proven to be correct to a precision of next-to-leading-logarithms(NLL). Since then it has been extended to describe hadron-hadron collisions as well.
The merging algorithm begins by separating the phase spaces of the ME and the PS for different multijet processes by using a k_T measure. However, first different emission scales Q_i for different numbers of jets (i) are defined. In the case of hadron-hadron collisions, two final state particles belong to two different jets if their relative transverse momentum is larger than some cut-off value $k_{T,0}^2$ given by [72]

$$k_{T,ij}^2 = 2 \cdot \min\left(p_{T,i}^2, p_{T,j}^2\right)^2 \left[\cosh(\eta_i - \eta_j) - \cos(\phi_i - \phi_j)\right] \ . \tag{4.1}$$

The transverse momenta $p_{T,i}$ and $p_{T,j}$, the pseudorapidities η_i and η_j and the azimuthal angles ϕ_i and ϕ_j are the properties of particle one and two respectively. Hence a reconstruction of the shower history is created by clustering all initial and final state particles of a configuration given by a matrix element together by using the k_T jet algorithm. As can be seen by comparing with the table above, this is an extension of step three. Additionally, the p_T of each of the two jets has to be larger than $k_{T,0}$. After this step the matrix elements are reweighed by coupling weights and Sudakov form factors. The reason for weights on the matrix elements is to take effects into account that would appear in the corresponding parton shower evolution.The weights on the coupling constants are given by

$$w_{\text{coupling}} = \prod_{i=1}^{n} \frac{\alpha(Q_i^2)}{\alpha(Q_0^2)} \ . \tag{4.2}$$

The reweighing with NLL Sudakov form factors [72] is also done by calculating a weight factor, given by

$$w_{\text{sudakov}} = \frac{\Delta(Q_i^2, Q_0^2)}{\Delta(Q_j^2, Q_0^2)} \ . \tag{4.3}$$

The $\Delta(Q_k^2, Q_0^2)$ factors in equation 4.3 are defined by

$$\Delta(Q_i, Q_0) := \exp\left[-\int_{Q_0}^{Q_i} \mathrm{d}q \Gamma_{q,g}(Q_i, q)\right] \ . \tag{4.4}$$

The $\Gamma_{q,g}$ term is the integrated splitting function and contains the coupling constant and the two logarithmically enhanced terms in the limit $Q_0 \ll Q_i$. The coupling

constant entering $\Gamma_{q,g}$ is itself also subject to reweighing. The α_s terms are the strong coupling constants depending on different scales Q_i and were defined earlier. The Sudakov form factors represent the probability of no branching happening at Q_0 between the scales Q_i and Q_j.
After the matrix elements have been reweighed, the matrix elements and the parton shower are properly connected. The only thing left is a suitable choice of initial parameters.

4.3.2 CKKW-L Matching

As the name already indicates, CKKW-L matching [74, 79, 80] is based on CKKW matching, however, there are some differences. For one thing, while CKKW merging uses Sudakov weights for the reweighing and the k_T jet algorithm for the reconstruction of the jet history, the CKKW-L algorithm relies solely on the parton shower.
As in the case of CKKW merging, the merging process begins by producing a parton configuration at a specific initial energy scale Q_0^2, but as opposed to CKKW, the succeeding generation of the shower history is not performed by a jet algorithm. Instead it is created by the dipole cascade and the parton configuration that corresponds to the initial situation is chosen. The shower history contains intermediate states $S_0, \ldots, S_n$ and the corresponding emission scales $Q_1^2 > \ldots > Q_n^2$. In the CKKW-L algorithm the PDF's, the coupling constant and the Sudakov form factors become reweighed. To begin with the PDF's, events are reweighed with the PDF ratios so that all parton configurations have the same starting point S_0. The weighing parameter is given by

$$w_{\text{pdf}} = \frac{x_+^{'} f_q(x_+^{'}, m^2) \cdot x_-^{'} f_{\bar{q}}(x_-^{'}, m^2)}{x_+ f_i(x_+, Q_0^2) \cdot x_- f_{\bar{q}}(x_-, Q_0^2)} \ . \tag{4.5}$$

This is then followed by another reweighing with PDF's for each dipole splitting

$$w_{\text{pdf}} = \prod_{i=1}^{n} R_i^{PDF} \ . \tag{4.6}$$

Thirdly, the reweighing for the coupling constant has the same form as in CKKW merging, namely

$$w_{\text{coupling}} = \prod_{i=1}^{n} \frac{\alpha_s(Q_i^2)}{\alpha_s(Q_0^2)} \ . \tag{4.7}$$

Finally, the reweighing from Sudakov form factors is done by a vetoing algorithm. The form factors $\Delta_{S_i}(Q_i^2, Q_{i+1}^2)$ correspond to the probability of not having emissions from a state S_i between the scales Q_i^2 and Q_{i+1}^2. The veto algorithm reproduces all these probabilities for all intermediate states S_i by performing trial emissions with the dipole cascade. The algorithm begins with a certain state S_i at the corresponding scale Q_i^2. If the trial emission the veto algorithm produces is above Q_{i+1}^2 the state S_i is rejected.
For the initial state S_0 the starting scale is given by $Q^2 = m_{\text{inv}}^2/4$, where m_{inv} is the total invariant mass of the hadronic interaction. For a specific final state S_n with $n < N$, events are accepted as long as none of the parton pairs is larger than a merging scale Q_{merge}^2. N is the maximum number of partons. For the case of $n = N$ all events are accepted.

4.4 Fragmentation

Fragmentation [81] is an important part in the simulation of particle physics processes. After a particle collision and the subsequent parton shower many coloured particles exist. These particles must undergo further processes to achieve coulour neutrality as they cannot exist on their own due to colour confinement (see Chapter 2.3.1). Hadronization and fragmentation aim at simulating these processes. There are three models describing the hadronisation process; the 'Lund-String model', the 'Cluster fragmentation', and 'Independent fragmentation'. However, only the 'Lund String model' and 'Cluster fragmentation' are used at the ATLAS detector. These two models will be described more thoroughly in the following sections due to their importance for the generators used in this thesis. Cluster fragmentation is the model used by Sherpa while Pythia uses the Lund String model.

4.4.1 Cluster Fragmentation

Cluster fragmentation models are based on a property called pre-confinement [82]. It implies that the particles resulting from the parton shower can be grouped into colourless quark antiquark ($q\bar{q}$) pairs called clusters (see blue blobs in Figure 4.3). If gluons are among the objects resulting the shower, these are split into $q\bar{q}$ pair and then also included into the clusters (see the objects entering the blobs in Figure 4.3). However, these clusters are not yet real hadrons and are therefore called protohadrons. As a result of this the clusters are required to decay independent of each other into real hadrons. Most of the clusters decay into two hadrons which are only

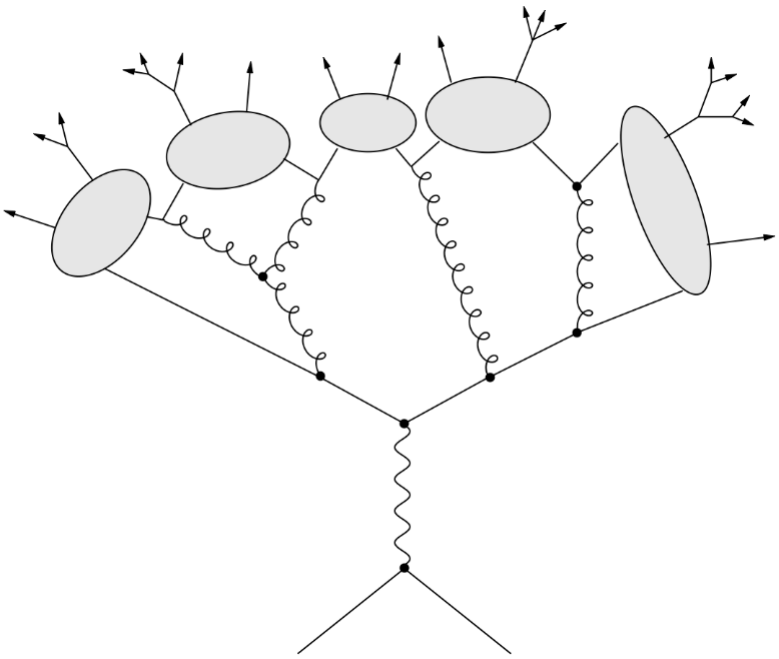

Figure 4.3: Schematic hadron collision depicting cluster fragmentation [84]. The blue blobs being the distinguishing property for this fragmentation model.

subject to flavour conservation.
There are two special cases that can occur in cluster fragmentation and have to be treated separately [83]. On the one hand clusters can be too light, i.e. not have enough energy, to decay into hadrons. In these cases the whole cluster, consisting of a $q\bar{q}$ pair is transformed into a single hadron and the remaining momentum is transfered to a neighbouring cluster. On the other hand clusters can also be too heavy meaning that the resulting hadrons would have unrealistically high momenta. To counter this issue new $q\bar{q}$ pairs are introduced and the original (high-energy) cluster is forced to split into two new clusters. Obviously each of the clusters receives only a fragment of the total momentum.

4.4.2 The Lund String Model

The Lund string model is probably the most sophisticated fragmentation model but also more complex than the independent or the cluster fragmentation model. It describes the evolution of particles after the parton shower. At very short distances the strong force between two quarks becoms negligible due to asymptotic freedom while the electromagnetic force becomes dominant. However, in the aftermath of a

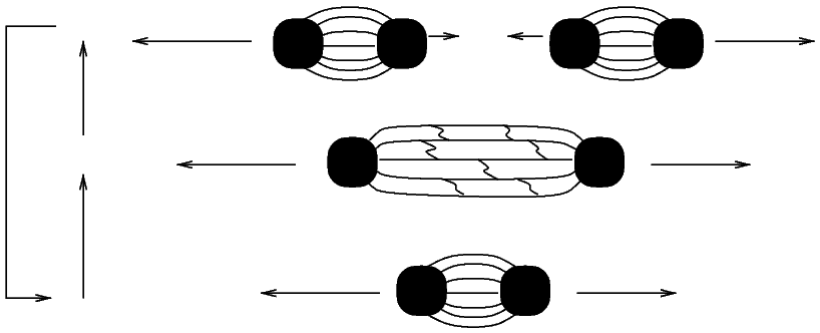

Figure 4.4: Illustration of the working method of the Lund String Model [85]. From bottom to top; particle connected by the string get moved apart until the energy stored in the string between them is large enough to break and create to new particles at the endpoint where the string broke. This creates two new particle pairs connected by a string meaning the process begins again, indicated by the arrow on the left pointing from the top of the figure to the bottom.

particle collision particles move apart from each other and QCD dictates that this increases the strong force between the particles. At some point the force between a colour connected $q\bar{q}$ pair will be large enough to create a new quark anti-quark pair out of the vacuum (see Figure 4.4). To simulate this, the Lund String Model reduces the colour field between the $q\bar{q}$ pair to a colour flux tube, which is again approximated by a relativistic massless string. The energy stored in the string between the two particles is proportional to the distance between them and is given by

$$V(r) \propto kr \ . \tag{4.8}$$

The factor k in the formula represents the tension of the string and given by $k \approx 1$ GeV/fm. A connected $q\bar{q}$ pair moving apart from each other transforms the kinetic energy of their translation into potential (string) energy. Once the string's potential energy becomes large enough, the string 'rips' apart and creates a new $q\bar{q}$ pair out of the vacuum (see Figure 4.4).

If the string's potential energy does not become large enough to create a $q\bar{q}$ pair out of the vacuum, the two end quarks turn around and move towards each other again. This happens when all the kinetic energy has been transformed into potential energy. Due to the particles repeatedly moving towards and apart from each other this kind of behaviour is called yo-yo effect (see Figure 4.5 and Figure 4.6). Particles entering the yo-yo mode can be considered as hadrons as no further string splitting can happen.

All the treatment so far has been for colour connected $q\bar{q}$ pairs. The other strongly

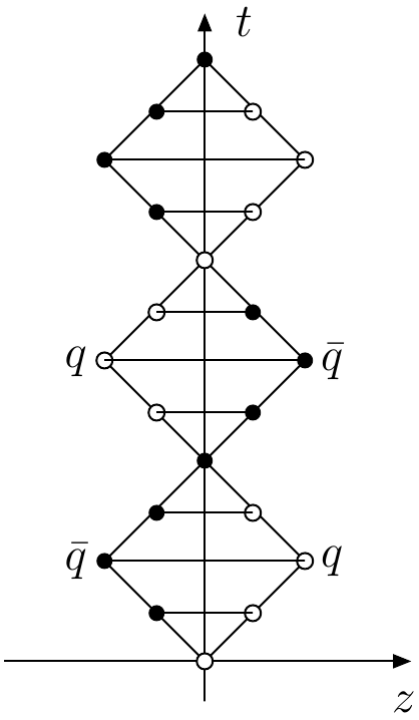

Figure 4.5: Schematic depiction of the yoyo-mode [83].

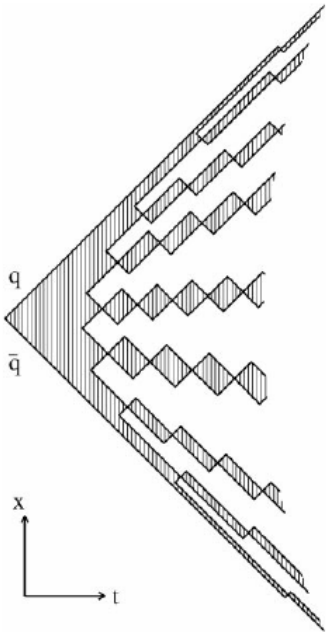

Figure 4.6: Depiction of yoyo-modes in the context of a fragmentation evolution [86]

interacting particles, the gluons, are in contrast to the quarks not described as an end point but as a kink in one of the strings [83]. As in the case of $q\bar{q}$ pairs, a gluon will stretch a string until there is enough energy stored in the string to produce a new $q\bar{q}$ pair out of the vacuum. The resulting hadron will then continue moving into the direction of the initial gluon. Conveniently this property automatically makes the string model IR-safe since soft gluons do not have enough energy to break strings. At the same time, the string model is also collinear safe. Collinear safe means that, splitting a proto-jet into two separate jet should not have an effect on the jet finding (see Chapter 3.2.1 and Figure 3.13). To be concerned with collinear safety the gluon has to be close to one of the string ends. As can be seen in equation 4.8 the potential energy stored in the string is proportional to the distance, meaning that once the string rips into two it will be on the side with the larger distance to the end quark. The proto-jet with the close gluon is therefore not split into two and thus collinear safe.

Chapter 5

Analysis

The aim of this analysis was to study multiple parton interactions in pp collisions. The focus will be on the determination of the frequency of MPI in collisions recorded by the ATLAS detector in 2011. However, since this thesis relies largely on MC generators several variables are compared between data and MC simulations in order to assess the reliability of the MC generators.
The MC generators used in this study were Pythia v8 [63] and Sherpa v1.4.2 [66]. Initially Jimmy + Herwig + AlpGen was also included in this study, however, during the study it turned out that the simulations using AlpGen required too much CPU time, thus rendering it impossible to obtain a meaningful amount of data in the given time. Even without AlpGen the time required to perform all the necessary simulations was unexpectedly long. The first step in this study was the accumulation of enough data, simulated and real. The gathering of centrally produced data also included large parts of data processing, meaning the application of measures like slimming, skimming, data quality considerations and finally the production of information relevant to this study. Slimming refers to the process of reducing the amount of data by applying data quality cuts and keeping only useful information while skimming means the reduction of data by applying physically motivated cuts. The Monte Carlo simulation part consisted of producing all the data sets necessary in this analysis. This means, an MC sample requiring two jets (dijets) and another sample focused on $pp \to Z \to l\bar{l}+jj+X$ events where $l = \{\mu^{\pm}, e^{\pm}\}$ that were produced in a single bunch crossing but where the jets did not come from MPI. These are the datasets required for the main aim of this work. Finally another data set was created where MPI were specifically simulated using methods provided by the different MC generators. This was done in order to determine the functionality of the different generators regarding MPI. The accumulation of data, real and MC, is outlined in Chapter 5.1.

This study was conducted at the hadron level which was due to the very long time a full detector simulation would have taken. In order to compare real data with MC simulations the real data had to be corrected back to the hadron level which was done by using a method called unfolding (see Chapter 5.2).
After the real data samples have been unfolded they can be compared with the results from the hadron level Monte Carlo simulations. Various properties providing useful information about the simulated processes are compared in Chapter 5.3 in order to determine whether the simulations have produced expected results. Additionally, these results are also compared with the distributions produced by real data.
Finally moving on to the main aim of this study, variables suitable for the evaluation of multiple parton interactions are introduced in Chapter 5.4 and using these variables the amount of MPI was calculated in Chapter 5.5.
As this is a study relying on simulated as well as real data uncertainties due to systematic as well as statistical effects distort the distributions. These effects are discussed in Chapter 5.6.

5.1 Data Sets and Monte Carlo Simulations

The goal of this work was an evaluation of multiple parton interactions. As already mentioned earlier, this requires real data samples as well as simulated data. Two different MC generators were used in this study to extract information about MPI in proton-proton collisions. However, real data comes in a raw format which makes additional steps necessary to obtain a usable data sample. For the case of MC generators the situation is different. The generators provide various different switches and levers to customise the process one is looking for. In the following I will explain the requirements and switches I set to obtain data sets, real and MC, that contain only information relevant for this study.

5.1.1 Event Selection

Minimum bias data is used in this analysis in order to compare the results obtained by the simulations with the results from a different study where the MPI contribution was determined in $W \to l\nu + jj$ events [27]. In that study minimum bias data was used as well to extract the fraction of multiple parton interactions. Minimum bias events are triggered by a signal in one of the MBTS scintillator counters which works at a very high efficiency (almost 100%) for non-diffractive inelastic proton-proton collisions [87]. In diffractive pp scatterings most final states do not leave

Run number	Period	#Events (before)	#Events (after)	P (%)	Type
178044	B2	2,139,509	1,631,999	76.27	Min. bias
178109	B2	2,517,368	2,356,523	93.61	Min. bias
180164	D4	493,977	481,212	97.42	Min. bias
180400	D6	588,514	515,726	87.63	Min. bias
183780	H2	659,067	659,067	100.00	Min. bias
186923	K1	815,394	802,476	98.41	Min. bias
186877	K1	728,590	534,199	73.32	Min. bias
186934	K1	705,498	292,081	41.40	Min. bias
186965	K2	877,890	872,269	99.35	Min. bias
189822	L6	474,341	460,999	97.18	Min. bias
190934	M4	1,256,123	2,985	0.23	Min. bias
178109	B2	1,436,534	1,386,637	96.53	Muons
179044	B2	1,032,381	898,623	87.04	Muons
191635	M10	2,391,862	2,391,862	100.00	Muons
191676	M10	621,972	532,547	85.62	Muons
191715	M10	3,600,586	3,600,586	100.00	Muons
191920	M10	1,795,015	1,728,001	96.27	Muons
191933	M10	3,004,542	2,948,984	98.15	Muons

Table 5.1: List of data sets used in this study; 'Before' and 'After' in columns two and three stand for before applying all the data processing measures and after; P = percentage of events passing the applied measures; Min. bias = minimum bias

any tracks in the acceptance range ($2.09 < |\eta| < 3.84$) of the MBTS counters but diffractive processes are not interest here.
After gathering a large amount of minimum bias data and performing all slimming, skimming, data quality and analysis steps only rather few events remained. To increase the amount of useful statistics another dataset was used which was specifically triggered for muons. The used data sets are presented in Table 5.1.
After the datasets were fetched, first slimming jobs were applied, where only events passing data quality requirements were kept. In the same step all information (variables, branches ...) not useful to this analysis were removed. In a second step called skimming, measures were applied directly to the remaining variables. The cuts applied at this level were early preselection cuts aimed at reducing the amount of data to less data but with a higher fraction of events passing the selection criteria. Thus also reducing the file size. The cuts were chosen in a way that events outside of areas interesting in this study were abandoned. The applied data cuts can be seen in Table 5.2.

Variable name	Cut value	Variable name in dataset
Jets		
Number of jets	$N_j > 1$	jet_AntiKt4TopoEM_n
Jet vertex fraction	jvtxf > 0.75	jet_AntiKt4TopoEM_jvtxf
Pseudorapidity η	$\lvert\eta\rvert \leq 2.8$	jet_AntiKt4TopoEM_eta
Transverse momentum	$p_T > 15$ GeV	jet_AntiKt4TopoEM_pt
Number of primary vertices	$N_{\text{vxp}} \geq 1$	vxp_n
Leptons ($e^{\pm}, \mu^{\pm}$)		
Number of leptons	$N_{e,\mu} > 1$	mu_muid_n or el_n
Pseudorapidity η ($\mu^{\pm}$ only)	$\lvert\eta\rvert < 2.4$	mu_muid_eta
Pseudorapidity η ($e^{\pm}$ only)	$\lvert\eta\rvert < 2.47$	el_eta
	$1.37 < \lvert\eta\rvert < 1.52$	
Transverse momentum	$p_T > 15$ GeV	mu_muid_pt or el_pt
Number of primary vertices	$N_{\text{vxp}} \geq 1$	vxp_n
Distance to primary vxp [mm]	$d_{0\text{pv}} > 10$	track_z0pv

Table 5.2: Applied requirements for data; Natural units were used ($\hbar = 1, c = 1$); vxp = primary vertex; Pseudorapidity $\eta = -\ln\left(\tan\left(\frac{\theta}{2}\right)\right)$

Jet cuts

Jets were reconstructed from clusters of connected energetic calorimeter cells, so called topological clusters, using the Anti-k_T jet algorithm introduced in Chapter 3.2.1 with a radius parameter of $R = 0.4$. Requiring more than one jet with a p_T higher than 15 GeV is motivated by the process considered here. Initially the p_T cut was set to $p_T \geq 20$ GeV however, this cut proved to vastly reduce the amount of usable data. A similar situation was observed in the MC simulations where a p_T as high as this reduced the amount of useful events coming from the simulations. Considering both, the low data statistics and the time it would have taken to simulate enough data using a $p_T \geq 20$ GeV cut it was decided to decrease the cut to 15 GeV. For the sake of enough statistics it was even considered to lower the cut to $p_T \geq 10$ GeV. Eventually the idea was rejected since in these energy regions there are also other processes contributing which might obscure the measured results.
Finally jets were required to have a jet vertex fraction larger than 0.75. The reason for applying this cut is explained in Chapter 5.1.1. In short, it is applied to ensure that the jets come from the primary vertex.
A very important cut was the requirement for $\Delta R > 0.5$. In the case here ΔR stands for the separation between leptons and jets and is defined as $\Delta R = \sqrt{\Delta\phi^2(j_m, l_n) + \Delta\eta^2(j_m, l_n)}$. As already mentioned, jets are not single objects but clusters of smaller objects moving in the same direction. Directly after a collision

many of the objects within a jet are colour charged. They will thus undergo a series of processes turning coloured partons into colourless hadrons. This is called fragmentation and was introduced in Chapter 4.4. Jets can also contain heavy quarks like bottom quarks, especially if they have a large momenta. One of the decay channels of the bottom quark is leptonic: $\mathrm{b} \rightarrow c + W^{*-} \rightarrow c + e^- + \bar{\nu}_e$. The semileptonic decay of heavy quarks could, accidentally, be misidentified as leptons coming from a separate process. Requiring this cut reduces the possibility for leptons arising from semileptonic quark decay within a jet.

Lepton cuts

After ensuring that there are potentially enough leptons in the data sample ($N > 1$), further requirements were applied. Both categories of leptons, electrons and muons, had to fulfill the same p_T requirements, namely $p_T \geq 15$ GeV. Initially this threshold was set to 20 GeV however, this reduced the number of usable events very much, which is why the p_T threshold was loosened. Furthermore the detected leptons were required to lay within specific, yet different pseudorapidity regions. The difference in these cuts comes from the different detector layers in which electrons and muons are measured. Electrons leave a track in the inner tracking system of the detector and finally deposit all their energy in the electromagnetic calorimeter. Thus electrons must have an $|\eta| < 2.47$ in order to lie within the coverage region of the inner detector. Due to the design of the electromagnetic calorimeter the region between the barrel component of the E-Cal and the end-caps cannot detect particles. In order to avoid this region an additional η cut had to be implemented, all electrons with $1.37 < |\eta| < 1.52$ were excluded from the analysis. This last cut was not necessary for muons, since they hardly interact at all with the detector material and do not deposit considerable amounts of energy in any of these detector parts. Lastly, leptons were required to pass the beam line within 10 mm from the primary vertex. This cut was implemented to increase the probability that the lepton came from the primary vertex. For the identification of muons, the Muid algorithm, as introduced in Chapter 3.2.3, was used while for the reconstruction of the electrons the standard ATLAS reconstruction algorithm was used. The electron reconstruction algorithm was introduced in Chapter 3.2.2.

Data Quality

The data sets used in this analysis were recorded by the ATLAS detector in 2011. The ATLAS detector works at a very high efficiency, however, it still is a technical machine, which means that it will not work properly at all time. Aside

from technical drawbacks, sometimes detector parts might be switched off due to maintenance or might not be working on full scale because of earlier calibrations. It is not always obvious from just looking at the data whether the detector was running properly. Therefore so called good runs lists (GRL) are used. These point out which luminosity blocks of a data set can be used (detector running properly) for physics analyses and which blocks should not be used due to problems with the detector or maintenance. A luminosity block is defined as a collection of events that succeeded each other in time. A further collection of luminosity blocks is called a run. In this analysis information from all parts of the detector were used so that only blocks with a fully functioning detector were used. The luminosities of the different data samples before and after applying the GRLs can be seen in Table 5.3.

Run number	Period	Del. Luminosity [pb^{-1}]	Int. Luminosity [pb^{-1}]
178044	B2	5.027	4.907
178109	B2	6.880	6.749
180164	D4	21.704	20.959
180400	D6	16.649	16.015
183780	H2	46.972	46.078
186923	K1	78.353	76.097
186877	K1	68.999	67.802
186934	K1	35.062	34.090
186965	K2	83.805	82.162
189822	L6	87.853	86.528
190934	M4	0.512	0.496
178109	B2	6.880	6.749
178044	B2	5.027	4.907
191635	M10	31.540	31.001
191676	M10	7.575	7.272
191715	M10	48.062	47.323
191920	M10	24.759	23.767
191933	M10	41.429	40.290

Table 5.3: Integrated Luminosity of the used data samples; Del. Luminosity = Delivered Luminosity; Int. Luminosity = Integrated Luminosity

Jet Vertex Fraction

After 2010, with increasing collision energy and luminosity, pile-up events contributed in ever larger numbers to *pp* collisions events. This turned into a serious

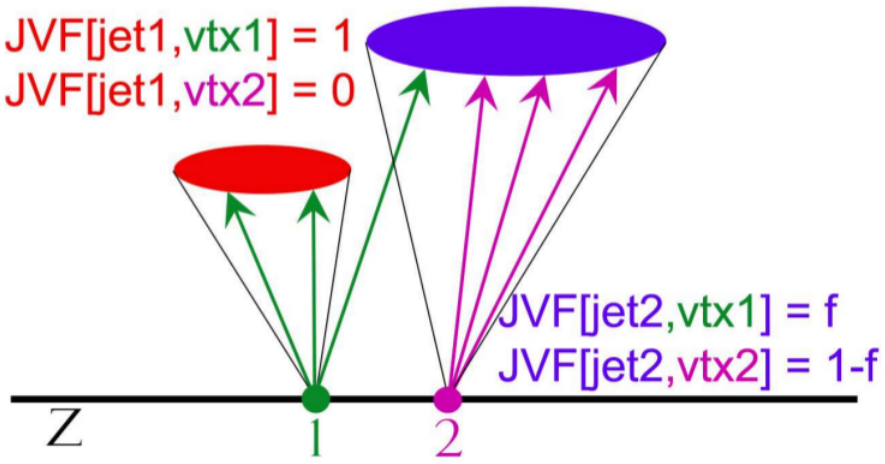

Figure 5.1: Jet vertex fraction; JVF[jet_i, vtx_j] stands for the fraction of tracks in jet_i coming from vertex j.

concern which is why methods to reduce the pile-up contribution were introduced. Remembering that at the LHC bunches of 10^{13} protons are collided rather than single protons (see Chapter 3) it is plausible to assume that more than one pp collision can occur in a bunch crossing. These additional pp collisions are called pile-up events.
Jets are nothing more than tracks concentrated within a certain structure. This structure can be a cone, as in the case of a cone algorithm, or more sophisticated structures like in the case of the k_T jet algorithm (these algorithms have been introduced in Chapter 3.2.1). In Figure 5.1 the definition of a jet is shown. In principle the radius parameter comprising the tracks is variable, however usually only two settings are used ($R = 0.4$ and $R = 0.6$). In a single pp collision all the tracks come from the only primary vertex. If bunches of protons are collided several pp collisions can occur, thus producing several primary vertices. In such a case a jet can have contributions from tracks originating from a different primary vertex as can be seen in Figure 5.1. Of course contributions from other primary vertices limit the information a jet can provide about a specific pp collision. Therefore, the JVF makes a statement about the fraction of charged tracks originating from a primary vertex [88].

The jet vertex fraction is formally defined as:

$$\text{JVF}(\text{jet}_i, \text{vtx}_j) = \frac{\sum_k p_T(\text{trk}_k^{\text{jet}_i}, \text{vtx}_j)}{\sum_n \sum_l p_T(\text{trk}_l^{\text{jet}_i}, \text{vtx}_n)} \tag{5.1}$$

In cases where there is no pile-up at all the situation is fairly simple. The JVF can be either one or minus one. If the jet is measured and all the tracks are coming from the primary vertex, the JVF = 1. If, on the other hand, the jet is very soft and falls outside of the tracking region, or, is not matched to any charged tracks, then the JVF is minus one. An example for a case with no pile-up can be seen in part a) of Figure 5.2.
In a collision with pile-up the situation becomes more complex. As can be seen in Figure 5.1 it is possible that some of the tracks that are concentrated within a jet originated from a different vertex. The JVF can thus take any value between 0 and 1, indicating the fraction of tracks from the primary vertex. Part b) of Figure 5.2 illustrates such a case.
The cut set in the event selection is thus used to ensure or at least increase the probability that the interactions happened in the same *pp* collision. However, even if a jet is reconstructed and passes the selection cut its measured energy might still be affected by pile-up events. This can be seen later on in the analysis (see Chapter 5.6) where the uncertainty due to pile up events almost contributes the largest overall uncertainty.

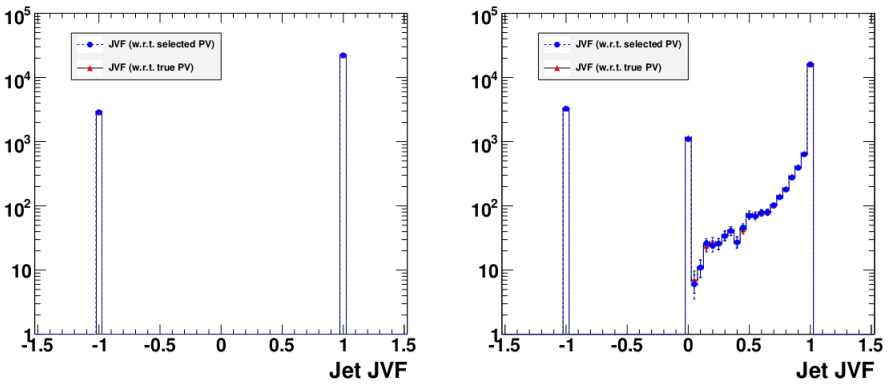

(a) No pile-up (b) With pile-up ($\langle N_{MB} \rangle$=2.3)

Figure 5.2: Jet vertex fraction plots with (b) and without pile-up (a). No pile-up means there are no other vertices and thus no contributions from other vertices; in a case with several vertices a jet can have track contributions from other vertices.

The value of the jet vertex fraction was chosen to be 0.75 because jets with a jet vertex fraction equal or larger than this are likely to be correctly reconstructed with a probability larger than 90%. Monte Carlo data was used to determine this fraction. The idea is that if a jet is reconstructed within a cone with $\Delta R(reco, MC) \leq 0.3$ around the truth jet than the measured jet is correctly reconstructed. For the MC data set used this corresponded to a correct identification rate of 90.04% which can be seen in Figure 5.3.

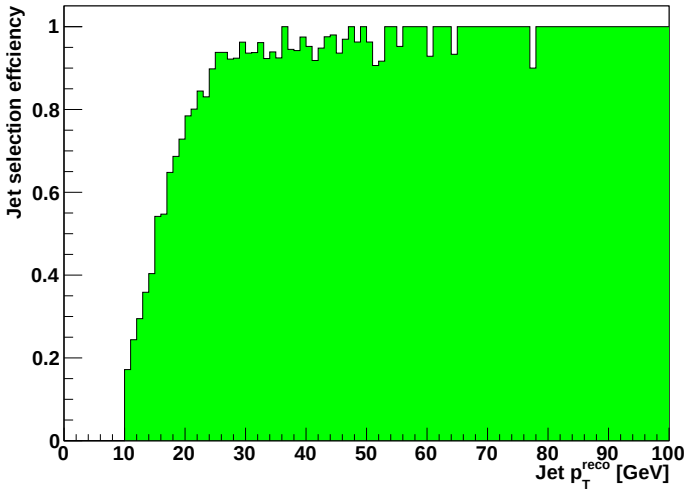

Figure 5.3: Jet vertex fraction selection efficiency for reconstructed jets with JVF ≥ 0.75 matched within ΔR(reco, MC) ≤ 0.3 to hard-scatter truth jets. The total integrated efficiency above $p_T^{\text{reco}} = 15$ GeV is 90.04%.

5.1.2 Event Simulation

The simulation of the required datasets was done on the CERN computer cluster (called Lxplus) and on the local university computer cluster called Steno by using the Athena framework. The used ATLAS releases were 16.6.2 and 17.2.4. The simulations and the immediate analysis were done using a package called HepMCAnalysis. Using release 16.6.2 this was version HepMCAnalysis_i-00-00-27 and in release 17.2.4 it was version HepMCAnalysis_i-00-00-62. The simulations were conducted using the Monte Carlo generators Pythia v8.145 and Sherpa v1.4.0. Initially the idea was also to include AlpGen + Jimmy + Herwig into the study however, after it was found out that simulations with AlpGen required very much time and had a very low efficiency in terms of useful events it was decided to drop AlpGen. For $9,000,000$ simulated events about $2,000$ survived a necessary process called unweighting. This part of the simulation procedure alone took many hours. After these two steps (simulation and unweighting) the resulting files had to be copied to HepMCAnalysis to perform the actual simulations and the analysis. After running with HepMCAnalysis on average one event was left of the initial $2,000$. To create meaningful data samples with AlpGen more resources and faster machines would have been needed.
The simulations in Pythia and Sherpa on the other side worked faster. They were repeated until a significant amount of data was generated; in this case set to

at least 100,000 events per data set. Each of the event generators comes with a specific set of switches which can be used to specify the process one wants to simulate. Table 5.4 and Table 5.5 depict the chosen settings for several of the switches in the different generators. If not stated otherwise, the remaining parameters were left with their default values. This study requires three Monte Carlo data sets per generator, thus six in total. This is, per generator, one with and one without multiple parton interactions switched on and another data sample simply simulating dijets. The MC generators provide switches and parameters to specify the process that is to be simulated. In the first MC data sample, the one containing multiple parton interactions, the reconstruction of an $e^{\pm}$ or $\mu^{\pm}$ pair passing all the requirements in addition to two jets has been required while MPI was switched on. In the second MC data sample (without MPI) the same objects have been required as in the first data sample but with the difference that here MPI had been switched off. An alternative approach to the simulation of MPI events is the motivation for the dijet data sample. The assumption is that the two interactions in the case of MPI are not correlated and can thus be considered as independent interactions. If the two interactions (here $Z \to l\bar{l}$ and the two jets) are independent then each of them should behave like single parton interaction. Thus a data sample containing only dijet events should be enough to pose as an MPI data set.

	Value			
Parameter	MPI	no-MPI	dijets	Explanation
Beams:eCM	7,000	7,000	7,000	CM energy of the beams
PhaseSpace:$\hat{\mathrm{p}}_{\mathrm{T}_{\mathrm{min}}}$	15.	15.	15.	Minimum invariant p_T
PhaseSpace:$\hat{\mathrm{m}}_{\mathrm{min}}$	80	80	-	Minimum invariant mass
PhaseSpace:$\hat{\mathrm{m}}_{\mathrm{max}}$	100	100	-	Maximum invariant mass
PDF:pSet	8	8	8	pdf for p beams; 8 = CTEQ6L1
SecondHard:Generate	On	Off	Off	Main switch for second hard scatter
SecondHard:TwoJets	On	Off	Off	Second hard = QCD $2 \to 2$ process

Table 5.4: Switches used in Pythia (see [73] for details)

For Sherpa the situation was slightly different as it uses so called 'run cards' as input files. The run cards already allow a sort of pre-analysis during the simulation process.

Parameter	Value		
	MPI	no-MPI	dijets
BEAM_1	2212	2212	2212
BEAM_ENERGY_1	3,500	3,500	3,500
BEAM_2	2212	2212	2212
BEAM_ENERGY_2	3,500	3,500	3,500
CKKW	$\sqrt{(30/E_{CMS})}$	$\sqrt{(30/E_{CMS})}$	$\sqrt{(30/E_{CMS})}$
Order_EW	2	2	0
Mass selector	$m_\mu \in [80, 100]$	$m_\mu \in [80, 100]$	-
NJetFinder	2 15 0 1 -1	2 15 0 1 -1	2 15 0 1 -1
ME_SIGNAL_GENERATOR	Comix	Comix	Comix
FRAGMENTATION	Ahadic	Ahadic	Ahadic
DECAYMODEL	Hadrons	Hadrons	Hadrons
MI_HANDLER	Amisic	None	None
SCALE_MIN	10.	-	-

Table 5.5: Switches used in SHERPA; explanations for the parameters can be found in Table 5.6 (see [66] for details)

BEAM_1	ID: beam part. 1 (2212 = p)
BEAM_ENERGY_1	CM energy of beam 1
BEAM_2	ID: beam part. 2 (2212 = p)
BEAM_ENERGY_2	CM energy of beam 2
CKKW	Sets up multijet merging
Order_EW	Process specific electroweak order
Mass selector	m_μ requirement
NJetFinder	Anti-k_T type algorithm to select #jets
NJetFinder	# jets - $p_{T_{min}}$ - $E_{T_{min}}$ - D para. - Algorithm
ME_SIGNAL_GENERATOR	Used matrix element generator
FRAGMENTATION	Used fragmentation model
DECAYMODEL	Module responsible for hadron and τ decays
MI_HANDLER	Central switch for MPI
SCALE_MIN	Minimum p_T for MPI

Table 5.6: Explanations on the switches set in SHERPA [66]

Following the event simulation an analysis program was used to pick only useful events. The explanations for the following cuts are more or less the same as for the objects in the real data samples. Therefore, only a short explanation for the cuts will be given here. Objects had to pass the following requirements:

- Electrons: Candidates were required to have a $p_T > 15$ GeV and to be within a suitable pseudorapidity region $|\eta| < 2.47$. To take care of the region between the barrel region and the end-cap region of the electromagnetic calorimeters, electrons falling into this region were excluded ($1.37 < |\eta| < 1.52$).
- Muons: A $p_T > 15$ GeV as well as a pseudorapidity of $|\eta| < 2.4$ were required. Muons were also required to be close to the primary vertex, requiring a distance to the primary vertex of $z_0 < 10$ mm.
- Z boson: To increase the probability of the two leptons originating from a Z boson an invariant mass between 80 GeV and 100 GeV was required.
- Jets: Jets were reconstructed from generated stable particles using the Anti-k_T algorithm with a distance parameter of $R = 0.4$. Stable particles meaning in this case particles with a lifetime greater than 10^{-10} s. Furthermore, a $p_T > 15$ GeV was required as well as an $|\eta| < 2.8$. Another very important requirement was $\Delta R = \sqrt{\Delta\phi^2(\mathrm{j}_m, \mathrm{l}_n) + \Delta\eta^2(\mathrm{j}_m, \mathrm{l}_n)} > 0.5$. This means that there must be a minimum separation between reconstructed jets and reconstructed leptons. The importance of this cut comes from the possibility of heavy quarks within jets to decay semi-leptonically (e.g. $b \to c + W^{*-} \to c + \mu^- + \bar{\nu}_\mu$). Without this last cut these semi-leptonic decay products can be misidentified as leptons coming from a hard primary interaction, even though they originate from a secondary vertex.

5.2 Unfolding

In every experiment the main interest is always on the undistorted underlying scientific processes. Nevertheless, experiments always require a setup, for example an apparatus, to measure and record the results. What all experimental setups have in common is that they are not perfect. The setup used here is the ATLAS detector which might reconstruct a particle or jet in the wrong calorimeter cell or produce an error when determining the deposited energy. If the focus is now on pure undistorted physical processes one has to undo (unsmear) the detector influence.
There are several methods called unfolding methods that provide functions to do this. The most common method is presumably bin-by-bin unfolding. It is a rather simplistic method with some inconvenient drawbacks. It requires, for example, the inversion of the migration matrix which can lead to problems if some bins are only sparsely populated, it could even be singular meaning an inverse matrix would not even exist. To overcome the shortcomings of the bin-by-bin method a new method called 'regularised unfolding' [89] was invented. Unfortunately this method is only applicable to one dimensional problems and has never been used very widely. The method used here is called Bayesian unfolding [90] and is considered to be the best working unfolding method, since it overcomes several of the other method's problems.

5.2.1 Bayesian Unfolding

This unfolding method is based on Bayes' theorem and is widely approved by statisticians as the most powerful tool for unfolding. It was developed in order to include migration effects and has several additional advantages over the other aforementioned methods. The main advantages are that it is theoretically well grounded, can be applied to multidimensional problems and does not require a matrix inversion. However, the most important advantage is probably the fact that this method produces the best results in terms of seeking a true unsmeared distribution. From a theoretical point of view this method provides, in a sense, a way to reverse conclusions.
In short, Bayes' theorem makes a statement about an event A happening given that another event B has already happened ($P(B) > 0$). It states:

$$P(A|B)P(B) = P(A \cap B) = P(B|A)P(A) \tag{5.2}$$

In words this means that the probability that event A and B will happen ($P(A \cap B)$) is equal to multiplying the probability for event B given that event A has already

occurred with the probability for event A alone. Of course, it works the same way the other way round, exchanging event A and B. Thus Equation 5.2 can be rewritten to obtain the most common form of Bayes' theorem:

$$P(A|B) = \frac{P(B|A)P(A)}{P(B)} \ . \tag{5.3}$$

At the LHC the ATLAS detector records huge amounts of detector influenced data. The following method can be used to reverse the influence of the detector.
The data the detector records are effects E_i $(i = 1, 2, \ldots, n_E)$, that can be an energy or a track variable or many others more. After N_{obs} experimental observations the result of the recording will often be a histogram filled with the number of times a specific effect E_i was measured $n(E) = (n(E_1), n(E_2), n(E_3), \ldots, n(E_{n_E}))$. The histogram $n(E)$ is of course influenced by detector effects. The effects measured by the detector are thus the outcomes of a set of causes C_j $(j = 1, 2, \ldots, n_C)$ that would produce a different histogram $n(C) = (n(C_1), n(C_2), n(C_3), \ldots, n(C_{n_C}))$.
The aim is now to correct the distribution of measured effects back to the cause level, which is, without detector effects. Using Bayes' theorem the probability that a given effect E_j was produced by cause C_i can be stated as:

$$P(C_i|E_j) = \frac{P(E_j|C_i)P_0(C_i)}{\sum_{l=1}^{n_c} P(E_j|C_l)P_0(C_l)} \ . \tag{5.4}$$

The probabilities $P(E_j|C_i)$ are the properties where the detector effects are taken into account and are usually determined from Monte Carlo simulations. The $P_0(C_i)$s are the initial probabilities of the causes C_i to occur and are usually taken from the best knowledge of the physical process involved. If however, no information about the process is available a uniform distribution, given by $P_0(C) = 1/n_C$, must be used instead. Using the initial probability $P_0(C)$ the initial number of true events can be calculated by

$$n_0(C_i) = P_0(C_i)N_{obs} \tag{5.5}$$

and by taking the detector inefficiencies via $P(C_i|E_j)$ into account the expected number of true events can be calculated as,

$$\hat{n}(C_i) = \frac{1}{\epsilon_i} \sum_{j=1}^{n_E} n(E_j)P(C_i|E_j) \qquad \epsilon_i \neq 0 \ . \tag{5.6}$$

The ϵ_i factors stand for the efficiency which is the probability that a given cause will evoke any effect at all and is thus given by

$$\epsilon_i \equiv \sum_{j=1}^{n_E} P(E_j|C_i) \tag{5.7}$$

The efficiency can be $0 \leq \epsilon_i \leq 1$ which means there is no certainty that a cause will create any effect. An $\epsilon_i = 0$ for example would mean that there is no possibility for a measurement. In other word, it means that the experiment is not sensitive to the cause C_i.
Using equations 5.4 and 5.7, equation 5.6 can be rewritten as:

$$\hat{n}(C_i) = \frac{1}{\sum_{l=1}^{n_E} P(E_l|C_i)} \sum_{j=1}^{n_E} P(C_i|E_j) n(E_j) = \sum_{j=1}^{n_E} M_{ij} n(E_j) \tag{5.8}$$

where M_{ij} are the elements of the unfolding matrix $\mathbf{M}$ and given by:

$$M_{ij} = \frac{P(E_j|C_i) P_p(C_i)}{[\sum_{l=1}^{n_E} P(E_l|C_i)][\sum_{l=1}^{n_c} P(E_j|C_l) P_0(C_l)]} \tag{5.9}$$

Using this the true total number of causes can be calculated as

$$\hat{N}_{true} = \sum_{i=1}^{n_C} \hat{n}(C_i) \ , \tag{5.10}$$

and the probabilities for these causes to occur as

$$\hat{P}(C_i) \equiv P(C_i|n(E)) = \frac{\hat{n}(C_i)}{\hat{N}_{true}} \ . \tag{5.11}$$

To gain a satisfying result some of these calculation steps have to applied repeatedly. The first step, however is always to calculate $P_0(C_i)$ and $n_0(C_i)$. The following three steps are the steps that have to be applied repeatedly until the χ^2 value between the old number of causes and the new number of causes (see step 2) becomes small enough.

1. Calculate $\hat{n}(C)$ and $\hat{P}(C)$
2. Perform a χ^2 comparison between $\hat{n}(C)$ and $n_0(C)$

3. Replace $P_0(C)$ by $\hat{P}(C)$, and $n_0(C)$ by $\hat{n}(C)$

The program used in this study to perform the unfolding is called RooUnfold [91]. To perform the unfolding the program requires a response matrix R_{ij} which maps the true distribution T_j on the measured distribution M_i. To generate the response matrix a full MC simulation is necessary. That is, with truth and reconstructed data. In the first step, which is also called training, the matrix is generated. In a second, optional, step a 'closure' test can be performed. By using for example only parts of the MC simulation for the training, the generated response matrix can be applied to the remaining simulation data in order to determine how good the response matrix works. Alternatively, a different (MC) dataset could be used for the closure test. Finally after the closure test has produced satisfying results the response matrix can be applied to a real data set in order to gain distributions a perfect detector would produce. In this context satisfying means a minimised χ^2.
In this study the response matrix was created by using MC truth and measured MC information. The response matrices for Δ_{Jets} and Δ^n_{Jets} can be seen in Figure 5.4 and Figure 5.5 respectively. Since the response matrix for Δ^n_{Jets} has a high amount of entries in high bins ($\Delta^n_{\text{Jets}} > 0.9$ or higher) Figure 5.6 shows the distribution for $\Delta^n_{\text{Jets}} \leq 0.9$. The MC data set used was a full simulation meaning that it consisted of two parts, truth and reconstructed (reco) information. The truth information is what a perfect detector would have recorded. The plot obtained from reconstructed information, also called measured information, is the distribution the ATLAS detector, which is influenced by technical effects, would have recorded. These two parts are required to predict the detector behaviour. Before applying the obtained response matrix to a real data set it is reasonable to apply it to MC data again. Just this time not training the response matrix but applying it to the reconstructed data and afterwards comparing the obtained distribution with the corresponding MC truth distribution. This is done to confirm that the unfolding works correctly. Therefore the unfolded distribution should resemble the distribution using truth data very well. This is called a closure test. The result of the closure test can be seen in Figure 5.8. It can be seen that the detector only has a very small influence on Δ^n_{Jets}, furthermore that the unfolding works correctly. Only at high $\Delta^n_{\text{Jets}} \approx 1$ does the detector have a significant effect. However this did not pose any problems as, in the fit performed in Chapter 5.5, bins accounting for high Δ^n_{Jets} values were ignored for physical reasons. Finally applying the response matrix to the real data distribution of Δ^n_{Jets} produces Figure 5.10 and Figure 5.9, for the muons and the minimum bias data sets. It can be observed that, using the response matrix created from MC data the real data distribution was not influenced largely by the detector. This is especially true for the muons data sample. The situation was not as clear for the minimum bias data set, however this was rather due to limited statistics than problems with the unfolding.

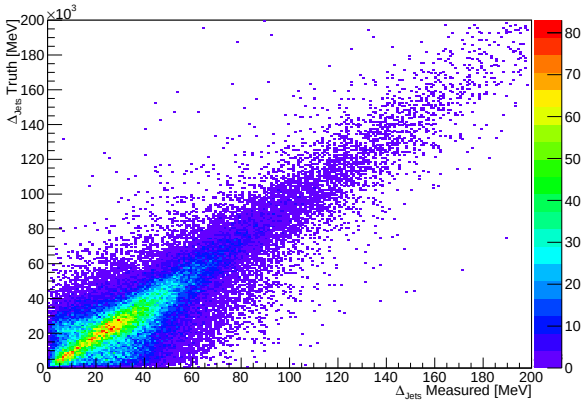

Figure 5.4: Monte Carlo response matrix generated from MC data. For each event Δ_{Jets} was calculated from truth and reconstructed information. The results were then fill into this matrix.

In Chapter 5.5 two different distinguishing variable will be introduced, Δ_{Jets} and Δ^n_{Jets}. Δ^n_{Jets} was selected as the variable of choice for the further proceedings of this study as it showed a higher resilience to detector effects. This can be seen, by comparing Figure 5.7 and Figure 5.8.

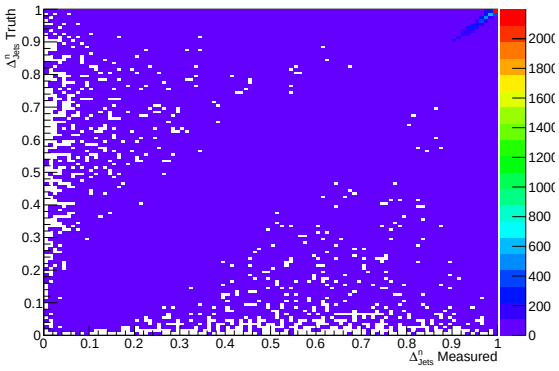

Figure 5.5: Monte Carlo response matrix generated from MC data. For each event Δ^n_{Jets} was calculated from truth and reconstructed information. The results were then filled into this matrix.

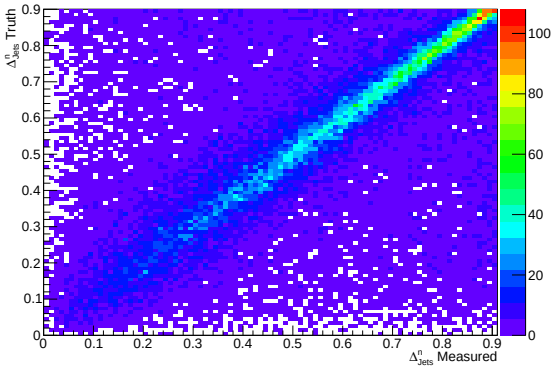

Figure 5.6: Zoomed in Monte Carlo response matrix generated from MC data. For each event Δ^n_{Jets} was calculated from truth and reconstructed information. The results were then filled into this matrix. Very high contents in bins close to 1 made the remaining plot unintelligible. Excluding high bins restored contrasts.

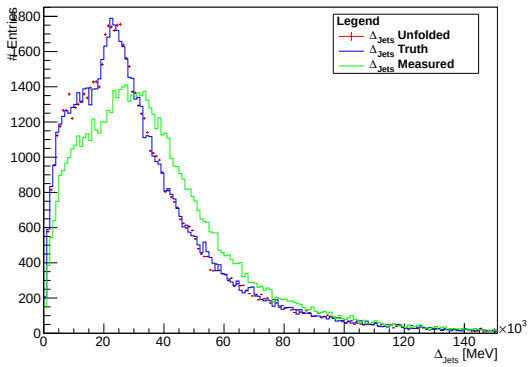

Figure 5.7: Closure test results for Δ_{Jets} using MC data. The green distribution is with detector effects while the blue distribution is without detector influences. The red distribution shows the unfolded distribution after the response matrix has been applied to the distribution with detector effects.

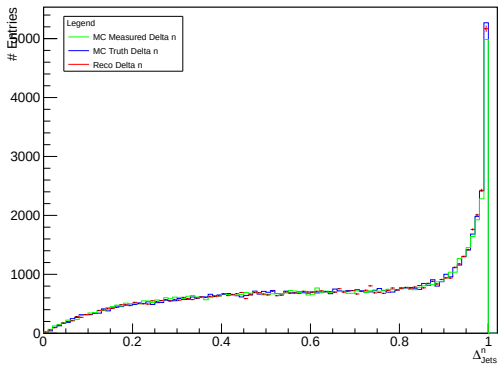

Figure 5.8: Closure test for Δ^n_{Jets}; The green distribution is what the ATLAS detector would have recorded. Applying the response matrix to it, the red distribution was the results. It should and does resemble the blue, truth, distribution very well.

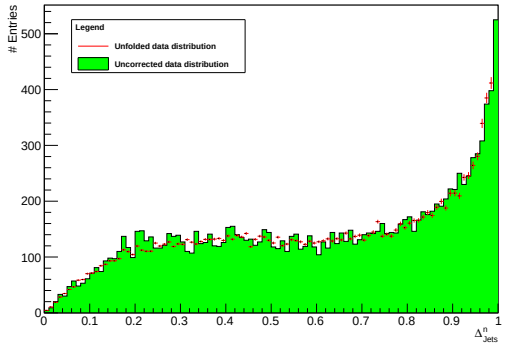

Figure 5.9: Unfolded Δ_n^{jets} distribution; used data sample: Minimum bias

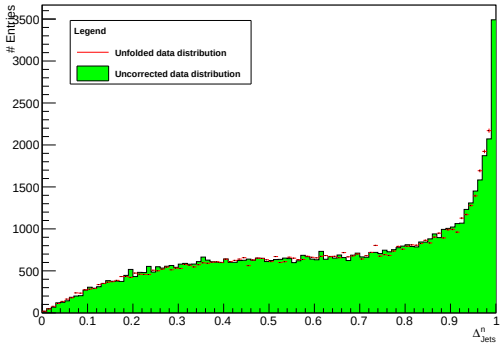

Figure 5.10: Unfolded Δ_n^{jets} distribution; used data sample: Muons

5.3 Comparison of Monte Carlo Data with Real Data

The theoretical physical knowledge acting as the foundation of Monte Carlo simulations is the same for all generators. There are however differences in their approach to simulating particle physics processes. Often there are processes (e.g. MPI) that are not yet fully understood or aspects that cannot easily be modeled. In these cases assumptions had to be made in the simulation software. There are working groups working solely on tuning these parameters so that they better resemble real data. Furthermore, various processes of the Standard Model can only be calculated in the limit where perturbation theory is valid. For processes in the non-perturbative regime, such as hadronisation of partons that have been scattered or radiated, phenomenological models must be used. These phenomenological models are usually different for the various generators, although often based on each other. Finally, the input syntax, which controls the program is different for the various generators as well. Some generators might have settings that enable the user to specify parameters that cannot be adjusted in other generators. All this makes it very possible that the generators produce different results, even if not by much. It is therefore worthwhile to compare the output the generators produce with each other. In the following subsections the results obtained by two different MC generators, Pythia and Sherpa, are compared with each other. The focus will, however, be on variables of interest in this study.
Ideally Pythia and Sherpa would produce the same results, however, the different assumptions made and technical restrictions (machine precision etc.) render this

unlikely. As already described in Chapter 4, the two generators differ in some crucial points (e.g. hadronisation). Nevertheless as the generators are to simulate the same processes similar results were expected. The following subsections will however show that this was not always the case. In some cases the differences could be explained by physical reasons while in other cases the differences are not likely to come from physical effects but from technical issues during the simulation process.

Leading Jet p_T

The obtained distributions for the transverse momentum of the leading jet $p_{T\text{lead}}$, can partly confirm theoretical expectations. It was expected that the leading jet p_T peaks much more sharply at comparatively small values for jets coming from MPI. This type of behaviour was expected from earlier studies like [26] and can be seen confirmed in the PYTHIA results. Figure 5.11 shows the leading jet p_T for PYTHIA and SHERPA with a simulation of MPI while Figure 5.12 shows the same properties just this time for events with no MPI contribution. The SHERPA results do not show a significant increase in the transverse momentum of the leading jet when moving from MPI (see Figure 5.11) to no-MPI (see Figure 5.12). In fact both distributions look very much alike which is most likely due to technical problems experienced during the simulations.
Since, theoretically, the transverse momenta of events with and without MPI demonstrate different behaviour for the leading jet p_T, it could be used as an early discriminator between the two interaction types. There are however other, more suitable, variables that will eventually be preferred.

In the case of simulated dijets the situation is clearer. In these simulations only two jets passing all cuts were required. Both simulations confirm each other very well which can be seen very well by comparing the PYTHIA and SHERPA simulation, shown in Figure 5.13. Finally considering the real data samples it can be seen that the minimum bias data sample (see Figure 5.14) is much better described by the simulations with no-MPI (generated by Pythia). Thus indicating, that, if the real data distribution consists of different fractions of events with and without MPI the fraction of events with MPI must be rather small. For the muons data sample (see Figure 5.14) the situation looks different. The transverse momentum of the leading jet peaks at smaller p_T values than the minimum bias data sample and falls off much faster when moving to higher p_T values.

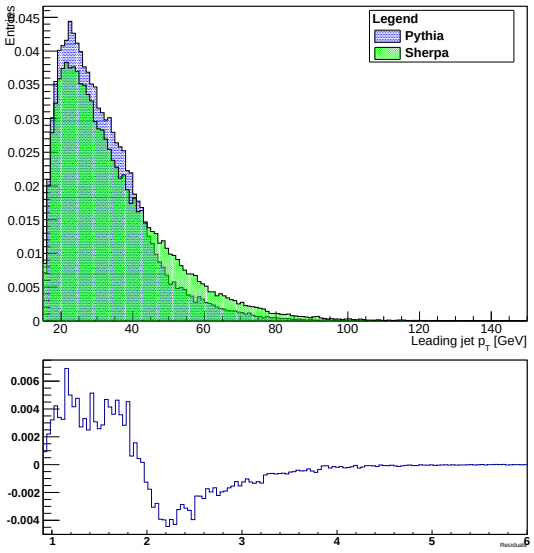

Figure 5.11: Leading jet transverse momentum distribution for Pythia and Sherpa. Simulation with MPI

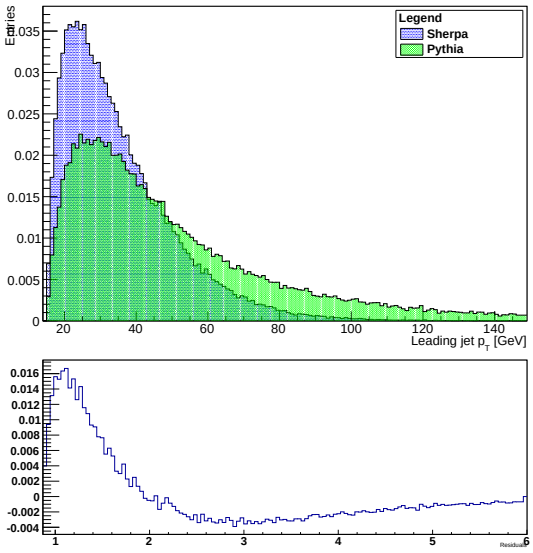

Figure 5.12: Leading jet transverse momentum distribution for Pythia and Sherpa. Simulation without MPI

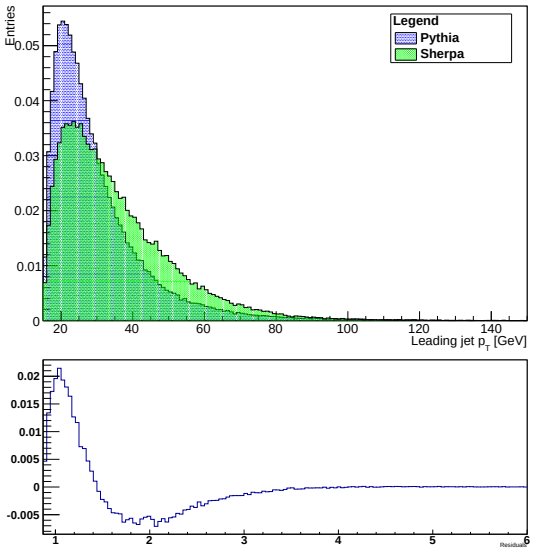

Figure 5.13: Leading jet transverse momentum distribution for Pythia and Sherpa simulating dijet events

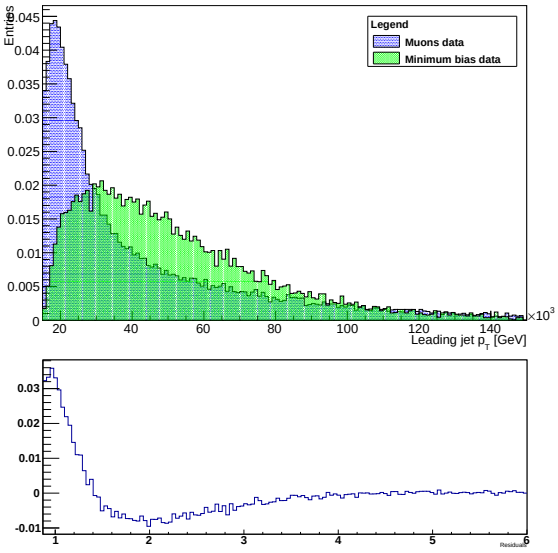

Figure 5.14: Leading jet transverse momentum distribution for the two real data sets.

Angular separations $\Delta\phi$

In this study, three different situations were of interest. In the simulations switches could be used to specify the process of interest thus obtaining three different distributions. One with a full MPI simulation, another without MPI and finally a simulation of dijets.
The two jets generated in the dijet simulation must show a distinct peak at $\Delta\phi \approx \pi$. In the simulation there is only the signal process without any influences. The jets should thus balance each other very well. Of course there can be minor distortions from soft radiative processes or non-negligible initial transverse momenta eventually causing slightly boosted jets.
In the simulation without MPI the $Z \to l\bar{l}$ process was considered the signal process. In this case the two jets originate from radiative processes of the signal process, like initial state radiation, where one of the collision partners emits a boosted (usually soft) gluon. The gluon decay products will thus be affected by the boost, resulting in the two jets not being as balanced as in the dijet production case. Of course, since one of the collision partners emitted a particle the emitting particle must recoil against it, thus introducing a non-negligible transverse momentum on the leptons. As a result of this, the leptons, the results of the signal process, should not balance each other perfectly either.
One of the main assumptions in the simulation of MPI is that the two processes, here $Z \to l\bar{l}$ and the jet producing process, are not correlated and should thus not influence each other. Each of the processes should thus produce a distribution that resembles a single parton interaction. The following plots show the angular difference $\Delta\phi(j_1, j_2)$ between the two jets for different generators and data samples; first for the MC generators followed by the real data plots.
Figure 5.15 depicts the angular difference for a full MPI simulation generated by Pythia. It can be seen that Pythia reproduces this expectation very well while Sherpa (see Figure 5.15) shows a similar distribution but has significant contributions in lower bins meaning lower angular differences. This behaviour can be checked by comparing with the angular difference between the two jets in the dijet samples. Figure 5.17 depicts $\Delta\phi(j_1, j_2)$ for the case of dijet simulations performed by Pythia or Sherpa respectively. Dijets are two jets originating from a single hard interaction (see part a) in Figure 2.5). Momentum conservation dictates that the outgoing particles must roughly balance each other. Only roughly because effects like final state radiation or effects introduced earlier in this section can divert particles. Further inaccuracies can originate from the particle reconstruction and the jet algorithms.
Pythia simulations of MPI (see Figure 5.15) and dijets (see Figure 5.17) look alike thus suggesting that, at least from this point of view, a full simulation of MPI can

be replaced by dijet simulations. SHERPA on the other hand shows significant differences (see Figure 5.15 and Figure 5.17). In both cases a peak at high angular differences can be observed, however the distribution for MPI does show large contributions in lower $\Delta\phi(j_1, j_2)$ bins. SHERPA thus suggests that a simulation of MPI cannot simply be replaced by a dijet simulation. However, there were some technical problems during the simulation process, in some respect, unexpected behaviour. The SHERPA results must thus be considered with caution.
For a simulation without MPI a much flatter distribution without a distinct peak was expected. The jets in events without MPI are the result of radiation processes like ISR. The objects, for example gluons, emitted by processes like this do not favour certain angular differences. In contrast these objects would be emitted with a boost meaning that balanced jets are very rare. The corresponding distributions generated by PYTHIA and SHERPA can be seen in Figure 5.16. The PYTHIA plot shows a much flatter distribution than in the case of MPI or dijets. This means that the produced jets do not balance each other very well, thus confirming the expectation. The distributions do however also show a small peak at $\Delta\phi(j_1, j_2) \approx \pi/4$. There are two possible explanations for this peak. It can either come from gluon splitting or a real physics process. In case of the gluon splitting, the jet algorithm recognises a gluon and (falsely) splits it into two separate objects. This usually produces two almost collinear jets. The peak at $\pi/4 \approx 0.8$ comes from the radius parameter of the jet algorithm, $\Delta R = 0.4$. Two almost collinear jets would thus produce the minimum $\Delta\phi$ difference possible: $2 \cdot \Delta R = 0.8$. This peak comes from gluon splitting processes like $g \to gg$ or $g \to q\bar{q}$. After the hard scattering process all scattered partons are permitted to emit final state radiation. However, because of the jet algorithm's radius parameter $R = 0.4$ the additional jets are prone to appear at $\Delta\phi \approx 0.4$. Thus the angular difference between the two jets would be $\Delta\phi \approx 0.8$. The jet algorithm recognises a gluon and splits it into two separate objects which usually produces two almost collinear jets.
Real data distributions were expected to be a combination of events with and without MPI. Therefore the distribution of the angular difference between the jets should look like a combination of events with and without MPI. The domination of one or the other effect depends on the amount of the corresponding event type (MPI or no-MPI) in the data set. Figure 5.18 shows the distribution obtained from the real data samples. Both data distributions show a peak at $\Delta\phi(j_1, j_2) \approx \pi/4$. It is the same peak that can be observed in the MC simulation plots and comes, as in the MC case, from gluon splitting. The only difference being a larger contribution at large $\Delta\phi(j_1, j_2)$ values in the minimum bias data set which is not observed in the muons data sample. This suggests that the jet pair in the minimum bias data set has a higher contribution from well balanced jets than the muons data sample.

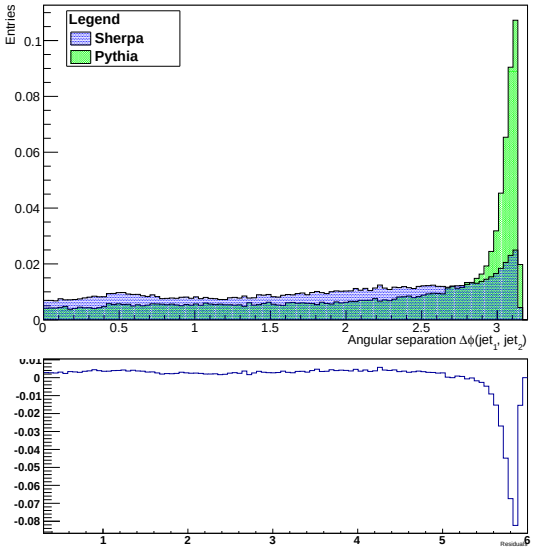

Figure 5.15: Angular separation between jet one and jet two generated by PYTHIA and SHERPA simulating MPI.

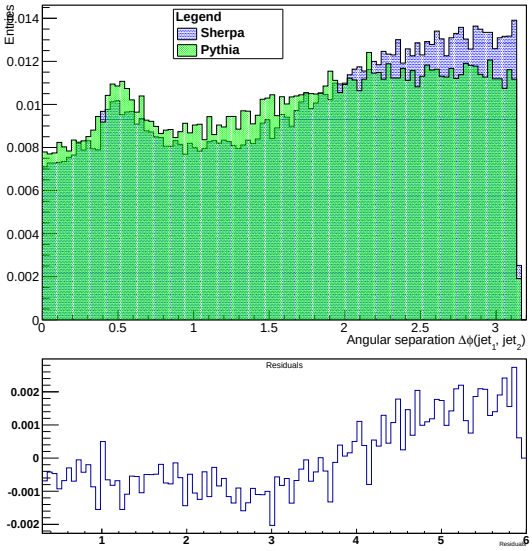

Figure 5.16: Angular separation between jet one and jet two generated by PYTHIA and SHERPA simulating events without MPI.

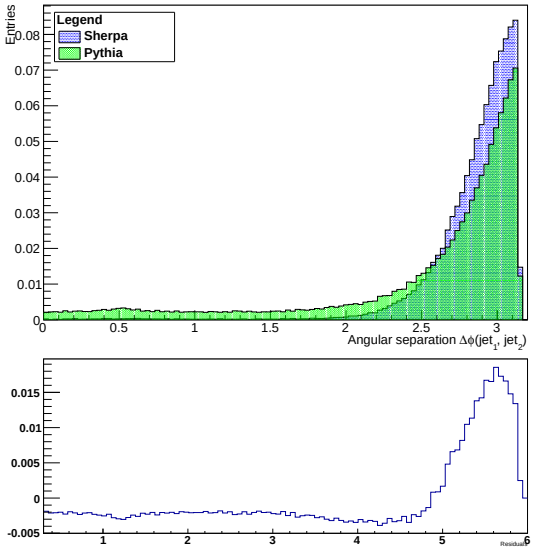

Figure 5.17: Angular separation between jet one and jet two generated by PYTHIA and SHERPA simulating dijets.

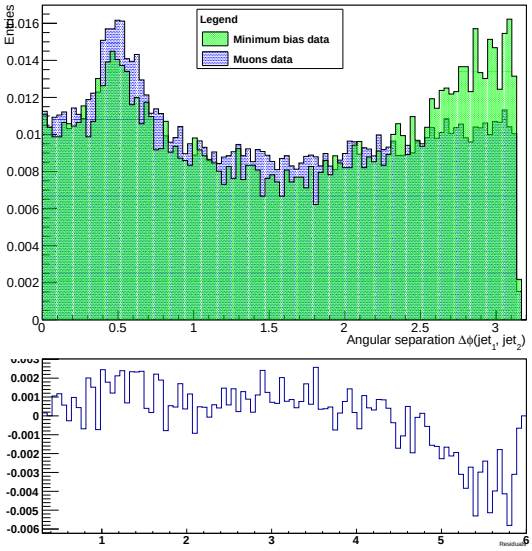

Figure 5.18: Angular separation between jet one and jet two generated with the real data samples.

Z Boson Mass

The two leptons produced in the signal process are required to originate from a Z boson, thus the invariant mass of the two reconstructed leptons must be in a range around the correct Z boson mass ($m_Z \approx 91.186$ GeV). The reasons why a clear peak at the correct mass was not expected were distorting processes like radiative processes and the limited measurement accuracy. It can for example be seen that the distributions produced by the MC simulations are much more narrow than those from real data. All the MC simulations produce distributions with peaks at the correct Z boson mass. Especially the PYTHIA simulations produce very clean distributions. This can be seen in Figure 5.19 for the case with a simulation of MPI and in Figure 5.20 for the case without MPI. SHERPA on the other hand suggests a significant contribution from invariant masses larger than the correct Z boson mass (see Figure 5.19 and Figure 5.20). There is no physical explanation for this kind of behaviour. During the simulations with SHERPA several technical problems occurred, thus it is imaginable that the excess at high Z boson masses comes from these technical problems during the simulations.
The real data samples also show distinct peaks at the correct Z boson mass and can be seen in Figure 5.21. The real data distributions are however broader than those obtained from MC simulations. This was expected and is most likely caused by detector effects since the plots presented in this section are not unfolded.

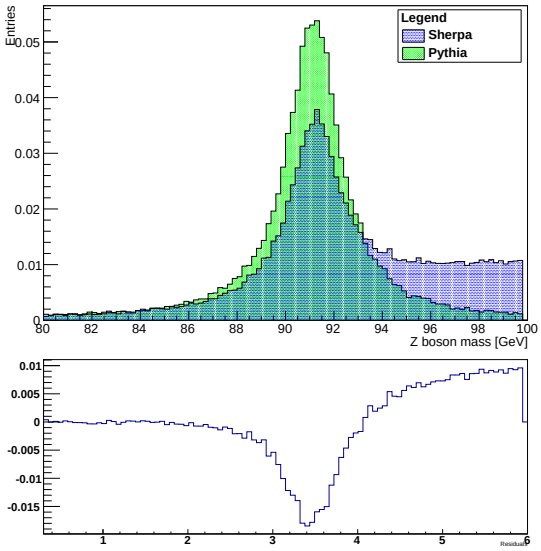

Figure 5.19: Z boson mass generated with PYTHIA and SHERPA simulating MPI

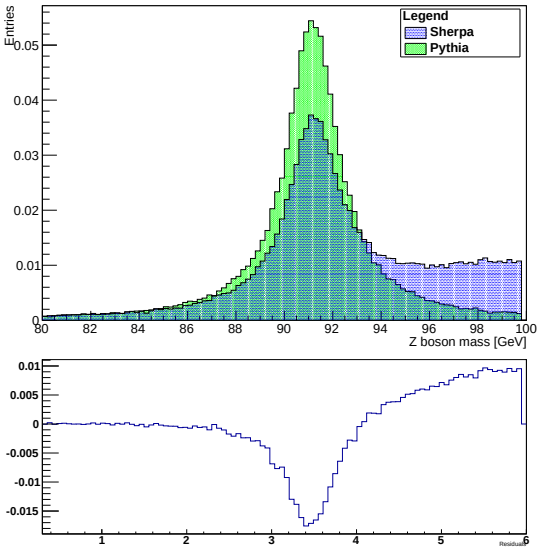

Figure 5.20: Z boson mass generated with PYTHIA and SHERPA simulating events without MPI

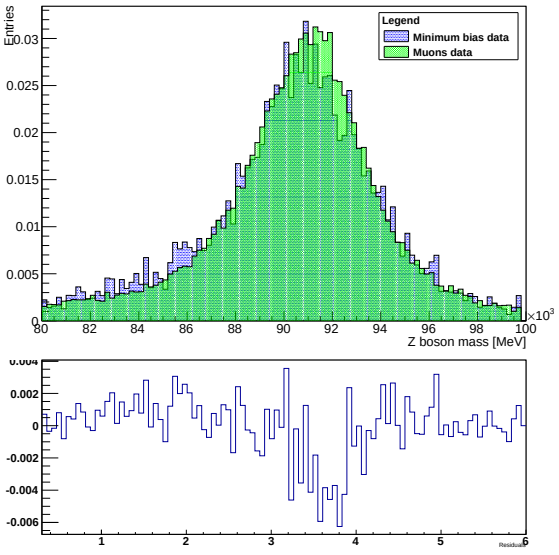

Figure 5.21: Z boson mass generated with the real data samples

Z Boson p_T

The transverse momentum of the Z boson is the result of the transverse momenta of the constituents of the signal process. Therefore, in the case of MPI, where the two interactions are considered as independent of each other the transverse momentum of the Z boson should be small, while it should be significantly larger in the case of no-MPI. Due to the emission of the jet producing particle the collision participants will receive a non-negligible transverse momentum thus generating a Z boson with a larger p_T than in the case of MPI.
This type of behaviour is confirmed in the PYTHIA simulations, as can be seen in Figure 5.22 and Figure 5.23. For the simulation with MPI (see Figure 5.22) the distribution peaks at very low transverse momentum values. A peak at exactly zero was not be expected since there are always diverting effects like non-negligible initial transverse momenta of the collision partners and radiative processes.
For no-MPI higher p_T values were expected since the two jets required in the process will most likely have originated from radiative processes. Since the requirement on the jet p_T is large (15 GeV), the recoil, one of the collision partners experiences must also be comparatively large, thus introducing a larger Z boson p_T than in the case of MPI. This sort of behaviour can be seen confirmed in Figure 5.23. The differences between the MPI and the no-MPI simulations in PYTHIA are very distinct and thus indicate that the transverse momentum of the Z boson could be used as a distinguishing variable in $l\bar{l} + 2$ jet events. In this study however, the Z boson p_T was not used as the aim was slightly different and because the results produced by SHERPA would not make such an approach sensible.
While PYTHIA produces very reasonable plots, SHERPA produces distributions that were not expected. The Z p_T is depicted in Figure 5.22 for simulations with MPI and in Figure 5.23 for a simulation without MPI. This type of behaviour is confirmed by neither the PYTHIA MC simulations nor by real data. It is therefore likely that technical issues experienced during the simulations caused these wrong distributions.
The distributions for real data are depicted in Figure 5.24. It can be seen that in the case of the minimum bias data sample the Z boson has, on average, a smaller transverse momentum than in the muons data sample. The reason for this kind of behaviour comes most likely from triggers that were used in the muons data sample.

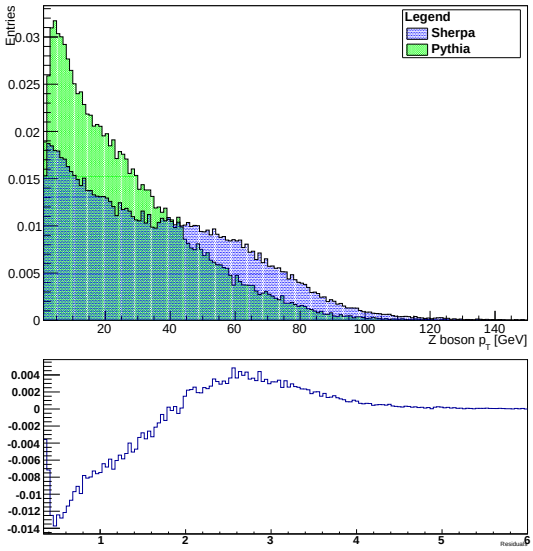

Figure 5.22: Z boson p_T generated with PYTHIA and SHERPA simulating events with MPI

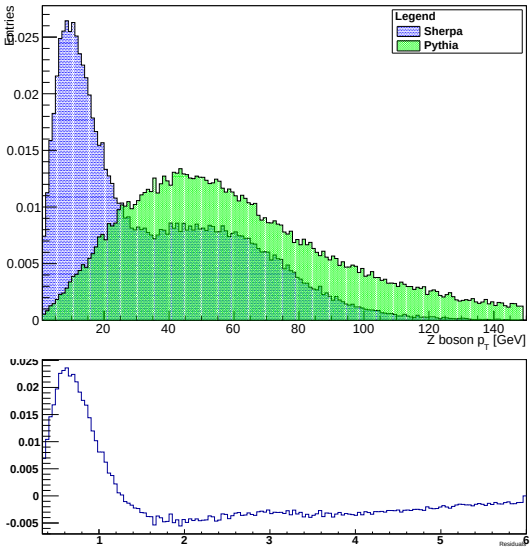

Figure 5.23: Z boson p_T generated with PYTHIA and SHERPA simulating events without MPI

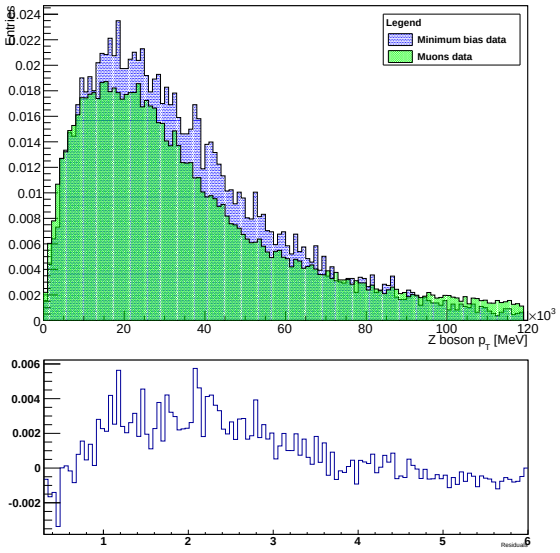

Figure 5.24: Z boson p_T generated with the real data samples

5.4 Distinguishing Variables

One of the main aims of this study was the separation of events with and without MPI. To do this a suitable property was required. The transverse momentum of the leading jet, for example, can act as an early indicator. However, it is not a suitable variable providing a clear separation. To obtain such a property a slightly different approach was chosen.
An important assumption made in the theoretical description of multiple parton interactions is the independence of the two occurring interactions. This also means that the two interactions must behave like two separate interactions. For single parton scattering processes momentum conservation dictates that the two particles that were created in the hard interaction roughly balance each other in the transverse plane. For events without MPI the created objects should not balance each other very well due to effects already explained in Chapter 5.3.
Nonetheless, the angular separation alone is not directly used as a distinguishing variable since there are effects like pile-up or radiation processes that influence it too much. The distinguishing variables used in this study are based on the transverse momentum of the final state objects. There are different implementations of such a property, two of which [27] were used in this study, but the underlying principle was in most cases the same. The first distinguishing variable is by,

$$\Delta_{\text{jets}} = |\vec{p}_{T,1} + \vec{p}_{T,2}| \ . \tag{5.12}$$

Regardless of the jets balancing each other, in most cases the vector sum of the jet p_Ts will not be zero. For events without MPI this was expected since in this case the jets originate from a boosted object. Of course there are additional phenomena diverting the jets or just the information about them. These can be technical effects, like limited detector precision, or physical effects like radiation processes. However, in contrast to events without MPI, in the case of MPI it is only these processes causing the diversion. As a result the p_T vector sum of the two jets is expected to be different from zero in both cases. Nevertheless, it is possible to distinguish, to some extent, between MPI and no-MPI by using Δ_{Jets}. The major difference is, that in cases without MPI the jets are boosted. Therefore, the jets originating from events with no-MPI should produce a high Δ_{Jets}. In events with MPI where the diversion is rather accidental, a small Δ_{Jets} was expected. Δ_{Jets} can be seen in Figure 5.25 using Pythia as generator and in Figure 5.26 using Sherpa. The corresponding distribution using the real data samples can be seen in Figure 5.27.

The MC simulations indicate that, while there clearly is a difference between the different simulations (see e.g. Figure 5.25), there is also a large area influenced by

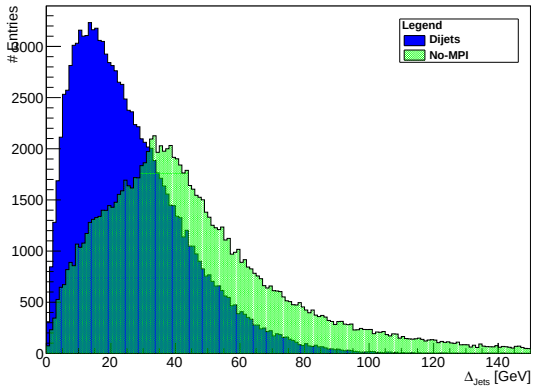

Figure 5.25: Distribution of Δ_{Jets} generated with PYTHIA results. The two graphs show a simulation with no-MPI and a dijet simulation, respectively

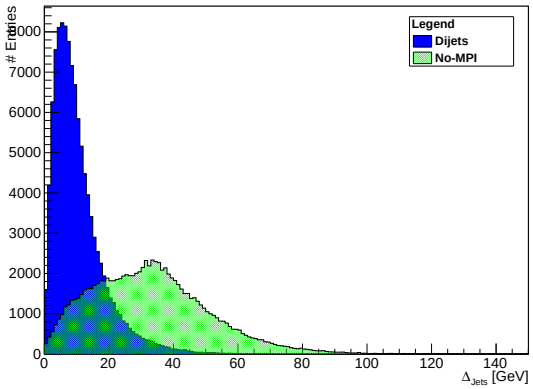

Figure 5.26: Distribution of Δ_{Jets} generated with SHERPA results. The two graphs show a simulation with no-MPI and a dijet simulation, respectively

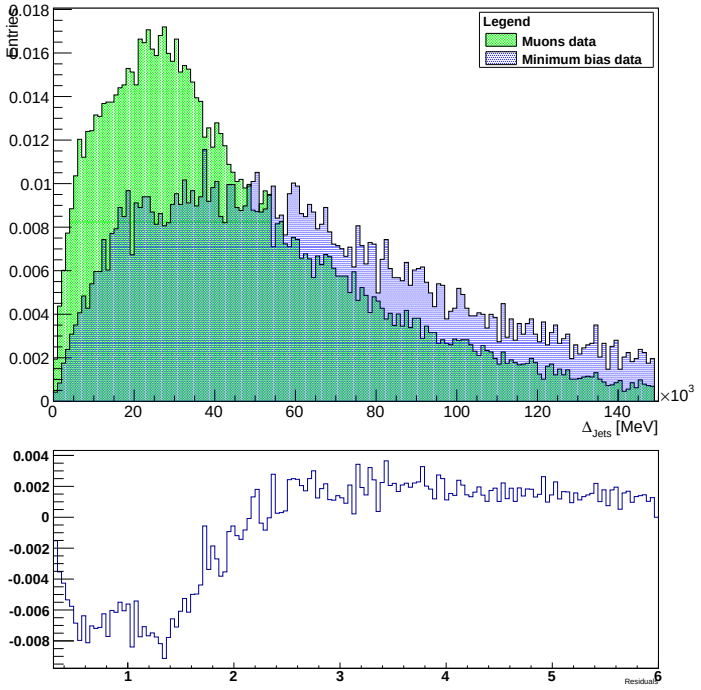

Figure 5.27: Distribution of Δ_{Jets} generated from real data.

both, events with and without MPI. This would make it hard to distinguish between

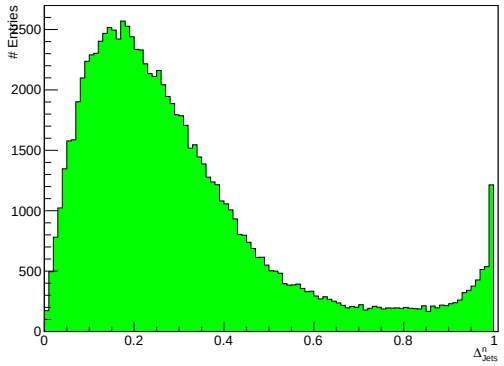

Figure 5.28: Δ^n_{jets} distribution generated by PYTHIA simulating dijets

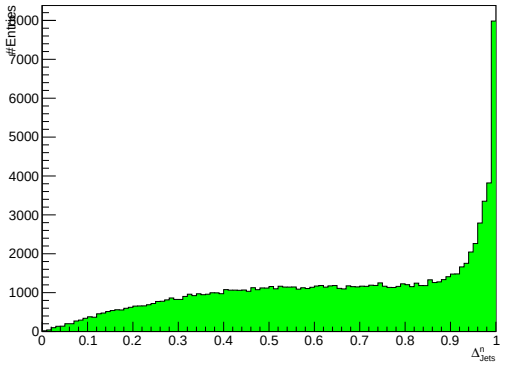

Figure 5.29: Normalised Δ^n_{jets} distribution generated by PYTHIA simulating No-MPI

the two cases. Therefore it is reasonable to consider the normalised version of Δ_{Jets}

$$\Delta^n_{\text{jets}} = \frac{|\vec{p}_{T,1} + \vec{p}_{T,2}|}{|\vec{p}_{T,1}| + |\vec{p}_{T,2}|} \ . \tag{5.13}$$

The two indices identify the two jets. This way the magnitude of the single momenta does not distort the results. The new variable Δ^n_{Jets} allows a clearer separation between cases with MPI and cases with no-MPI, basically, by normalising the jet momenta, it is the direction of the jets producing the Δ^n_{jets} distribution. Due to the better distinguishing ability of Δ^n_{Jets}, it was chosen in the following section (Chapter 5.5) to extract the fraction of MPI in a data sample containing data recorded by the ATLAS detector.
The MC simulations confirm the expectation that no single effect alone can reproduce the real data distribution but a combination of both. Therefore the real data distribution must be a combination of both, DPS and SPS. In this respect, the PYTHIA simulations, which can be seen in Figure 5.28 and Figure 5.29, show very reasonable results however, the distributions produced by SHERPA (see Figure 5.30 and Figure 5.31), especially for no-MPI, look incorrect. The corresponding, unfolded, distributions created from real data can be seen in Figure 5.32 for the minimum bias data set and in Figure 5.33 for the muons data sample.

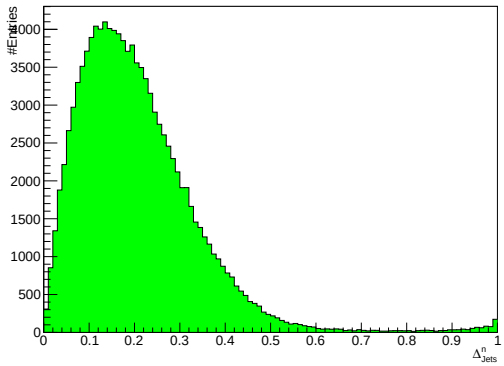

Figure 5.30: Δ^n_{jets} distribution generated by SHERPA simulating diets

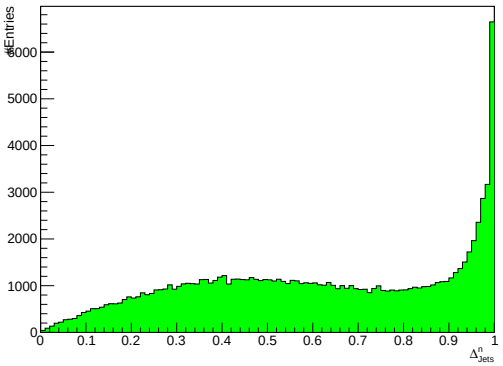

Figure 5.31: Normalised Δ^n_{jets} distribution generated by SHERPA simulating No-MPI

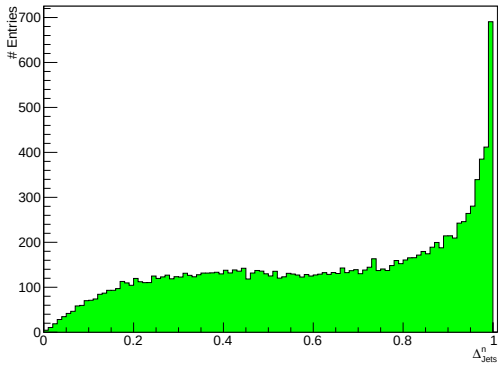

Figure 5.32: Unfolded Δ^n_{Jets} distribution generated from minimum bias data

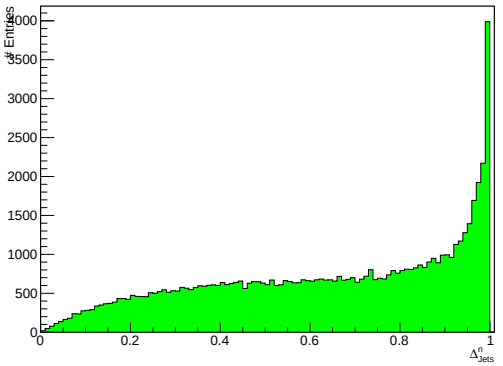

Figure 5.33: Unfolded Δ^n_{Jets} distribution generated from muons data

5.5 Determination of the Contribution of MPI

To determine the fraction of DPI events f_{DP} in a real data set a method called template method is used. In this study this means, two templates are created. One from dijet data (or the data sample containing MPI) and the other from the SPS (no-MPI) data set. These two templates are then fitted on top of the real data with the aim to minimise the deviation between the templates and the real data distribution. This is done by first establishing a fit function that depends on the two templates. This function is then used to minimise the difference between the function and the (bin) entries in the real data distribution. The method used to do this minimisation is called χ^2 minimisation.

5.5.1 χ^2 Minimisation Fit

A χ^2-fit [92] is a way to determine how well a fit describes the underlying distribution. It is arguably the most important test of this kind. Given a data set with real data, the question is which sort of distribution the real data can be described by. The χ^2-test provides an answer to the question how good a fit describes the data. It sums up all deviations between the real data measurement and the value the fit-function calculated and weights it with the error on the fit function's value.

$$\chi^2 = \sum_{i=1}^{n} \frac{(y_i - f(x_i))^2}{\sigma_i^2} \tag{5.14}$$

The y_i and $f(x_i)$ terms are the number of entries in bin i. As the minimisation will be performed on the Δ^n_{Jets} distribution the bins i correspond to Δ^n_{Jets} values. The variance σ_i^2 is the statistical error on bin i in the data sample. Assuming each bin content is distributed according to a Poisson distribution the error on each bin is given by $\sigma_i^2 = n_i$. A good fit should produce a $\chi^2 \approx n_{\mathrm{df}}$ where n_{df} is the number of degrees of freedom. This is because for a good fit the deviation between exact value and fit value should be within the boundaries of the error σ_i. Therefore, on average each term is expected to contribute 'one' to the χ^2-value. It might seem as if a $\chi^2 = 0$ could be achieved or, stated differently, every fit value exactly fits the measured value. However, a fit this good is usually not doable in a realistic scenario. Even very small χ^2 values are usually flawed or at least dubious since it would almost indicate a too good fit. A very small χ^2 usually indicates overstated errors or a handling of specifically selected data. Obviously, too large values are bad as well. It means that the obtained fit is not a particularly useful fit. Finally

however, there is no general rule what a good χ^2/n_{df} is. In principle it is left to the user to decide on limits. As a rule of thumb, a $\chi^2/n_{\mathrm{df}} \approx 1$ is usually considered as a good fit. For the fits performed here, n_{df} is number of bins in the Δ^n_{Jets} histogram. The fit-function used in this study is:

$$f(A,B) = (1 - f^{\mathrm{R}}_{\mathrm{DP}}) \cdot A + f^{\mathrm{R}}_{\mathrm{DP}} \cdot B \ . \tag{5.15}$$

The factor f_{DP} is the fraction of DPS contributing to the data set while $f_{\mathrm{SP}} = (1 - f_{\mathrm{DP}})$ represents the amount of SPS in the data set. A and B are the templates that are created using the MC simulations. A is the template from the data set without MPI while B is the MPI template created by using MC dijet or full MC MPI simulations. The data sets the fits were performed to were the real data sets introduced in Chapter 5.1, namely the minimum bias and the muons data set.
Instead of Δ_{Jets} the fit was performed to the Δ^n_{Jets} distribution since it showed a higher resilience to detector effects. For the fit the last seven bins, that is, all bins with $\Delta^n_{\mathrm{Jets}} > 0.93$ have been excluded. Events with a higher Δ^n_{Jets} represent situations where the two are almost parallel and are thus rather a test of the shower model.
The fractions extracted by using the χ^2 minimisation fit are presented in Table 5.7. Plots of the resulting fits can be seen in Figure 5.34 and Figure 5.35. These plots were obtained by using Pythia MC simulations for the templates (the simulation with no-MPI for template A and the dijet simulation for template B) and performing the fit to the unfolded minimum bias data set.

The results obtained by fitting the MC simulations to real data suggest that Pythia reproduces the real data distribution better than Sherpa. The best fits are obtained when using dijet events instead of a simulation with multiple parton interactions. Not only are the fits obtained by using dijet events much better, e.g $\chi^2/n_{\mathrm{df}} = 1.17$ using dijets against $\chi^2/n_{\mathrm{df}} = 1.71$ with a full MPI simulation, they also reproduce results from earlier studies better [27]. This earlier study determined the amount of MPI in $W \to l\nu + 2$jets events (from hereon called W study), however, applied slightly different cuts and used different data sets. Some of the cuts applied in the earlier study were different from cuts applied in this study. However, these differing cuts were process specific (e.g. $\not\!\!E_T$ cuts). The only different common cut was on the transverse momentum p_T of the particles, while this study required a $p_T > 15$ GeV, the W study required a $p_T > 20$ GeV. Furthermore, their study used data recorded in 2010, while in this study 2011 data is used, which means that their data set most likely had a much lower pile-up contribution. Additionally did they use dijet events exclusively as a replacement for MPI. They determined the fraction of DPS events to be $f^{(D)}_{\mathrm{DP}} = 0.080$ at detector level or $f^{(H)}_{\mathrm{DP}} = 0.064$ at the hadron

Generator	Data set	Fractions f_{DP} and f_{SP}	χ^2/n_{df}
PYTHIA (MPI)	Muons	$f_{\mathrm{SP}} = 9.68 \cdot 10^{-1} \pm 5.80 \cdot 10^{-3}$ $f_{\mathrm{DP}} = 3.16 \cdot 10^{-2} \pm 2.35 \cdot 10^{-3}$	$\chi^2/n_{\mathrm{df}} = 2.57$
PYTHIA (MPI)	Min. bias	$f_{\mathrm{SP}} = 9.46 \cdot 10^{-1} \pm 9.49 \cdot 10^{-3}$ $f_{\mathrm{DP}} = 5.37 \cdot 10^{-2} \pm 5.67 \cdot 10^{-3}$	$\chi^2/n_{\mathrm{df}} = 1.71$
PYTHIA (dijets)	Muons	$f_{\mathrm{SP}} = 9.52 \cdot 10^{-1} \pm 6.23 \cdot 10^{-3}$ $f_{\mathrm{DP}} = 4.78 \cdot 10^{-2} \pm 3.45 \cdot 10^{-3}$	$\chi^2/n_{\mathrm{df}} = 2.54$
PYTHIA (dijets)	Min. bias	$f_{\mathrm{SP}} = 9.22 \cdot 10^{-1} \pm 1.03 \cdot 10^{-2}$ $f_{\mathrm{DP}} = 7.78 \cdot 10^{-2} \pm 5.94 \cdot 10^{-3}$	$\chi^2/n_{\mathrm{df}} = 1.17$
SHERPA (MPI)	Muons	Did not converge	
SHERPA (MPI)	Min. bias	$f_{\mathrm{SP}} = 8.74 \cdot 10^{-1} \pm 3.55 \cdot 10^{-2}$ $f_{\mathrm{DP}} = 1.26 \cdot 10^{-1} \pm 3.51 \cdot 10^{-3}$	$\chi^2/n_{\mathrm{df}} = 3.29$
SHERPA (dijets)	Muons	Did not converge	
SHERPA (dijets)	Min. bias	$f_{\mathrm{SP}} = 9.89 \cdot 10^{-1} \pm 1.11 \cdot 10^{-2}$ $f_{\mathrm{DP}} = 1.31 \cdot 10^{-2} \pm 5.54 \cdot 10^{-3}$	$\chi^2/n_{\mathrm{df}} = 3.22$

Table 5.7: Extracted fractions by the minimisation fit; f_{SP} = fraction of single parton scattering events; f_{DP} = fraction of double parton scattering events; The number of degrees of freedom $n_{\mathrm{df}} = 91$, in all cases

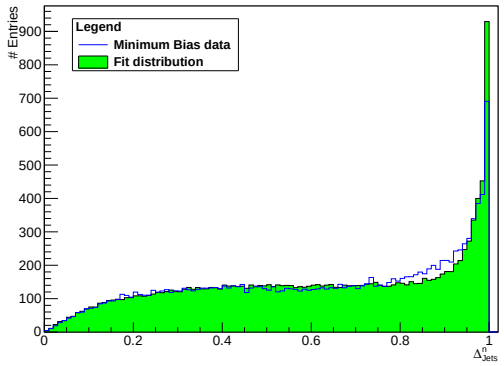

Figure 5.34: Data distribution and the fit distribution as determined by the χ^2 minimisation fit. Used data: Minimum bias. Generator: PYTHIA. Version: Dijet

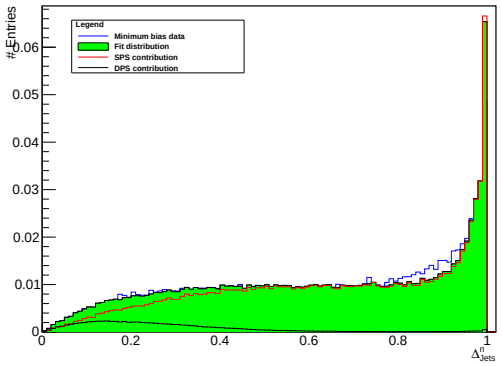

Figure 5.35: Data distribution and the fit distribution as in Figure 5.34, here accompanied by the weighted SPS and DPS parts

level. This result can be confirmed in this study with $f_{\mathrm{DP}} = 0.078$. This result

is obtained by using the same approach as the W study, meaning the fraction was extracted from a minimum bias data sample using a dijet simulation instead of a full MPI simulation. However, the fraction is of course influenced by uncertainties. In Chapter 5.6 the uncertainties influencing f_{DP} are discussed. Special attention is hereby on the uncertainty due to pile-up events. In the subsection on pile-up (see Section 5.6.2) events an alternative approach to the determination of f_{DP} is presented. The result obtained with this new method is $f_{\mathrm{DP}} = 0.062$ which matches very well the hadron level fraction determined in the aforementioned paper [27]. As before, this fraction is extracted by using similar data and MC simulation as in the case of the earlier study. For template A and B PYTHIA simulations without MPI and dijets were used respectively. As in the earlier study the fit was finally performed to minimum bias data. The results obtained in this study show a remarkably good consistency with the results obtained by the earlier study. The results obtained with Sherpa on the other do not show a good consistency with the W study. However, this does not mean that the approach is wrong since there were technical issues in the simulation process. This can clearly be seen in some of the distributions (e.g. see Figure 5.23 or Figure 5.15) generated by Sherpa.
If a simulation of MPI is used instead of dijet events the determined fraction for MPI decreases by about 30%, from $f_{\mathrm{DP}} = 0.0778$ to $f_{\mathrm{DP}} = 0.054$. This result suggests that the implementation of MPI in PYTHIA cannot simply be replaced with dijet events and thus implys further that there are parameters which are part of the implementation of MPI that reduce the determined fraction of MPI. It is furthermore interesting to see that the amount of MPI in minimum bias data is larger than in a specifically preselected muons data sample.
The fractions found using SHERPA do not agree with the corresponding PYTHIA data samples. In the case of the full MPI simulation the fraction determined by SHERPA is approximately twice the fraction determined with PYTHIA while in the case of the dijet simulation the fraction determined with PYTHIA is about six times larger than the one determined with SHERPA. The plots the SHERPA simulations produced show qualitatively correct behaviour in may parts (see e.g. Figure 5.13), other properties however show very unexpected behaviour (see e.g. Figure 5.16 or Figure 5.22), finally resulting in insensible results for the fraction of the contribution from MPI. The reason for this behaviour is not fully understood. All results obtained with SHERPA are thus to be considered with caution. *HepMCAnalysis* does not yet include an implementation of SHERPA. However, I assumed that, since SHERPA is available on ther CERN servers it should be possible to use it in the simulation programs just as the other MC generators. The simulations with SHERPA did however cause many non-analysis related technical problems. Eventually several of these issues could be solved and all simulations were conducted but considering the quality of many of the properties and the fit it is most likely that there still were technical issues.

5.6 Uncertainties

Every study is influenced by uncertainties of some kind, may they be statistical or systematic. The uncertainties distorting the results of this study will be discussed in the following section. After determining all the uncertainties, the statistical and systematic uncertainties will separately be added in quadrature.

5.6.1 Theoretical Uncertainty

The simulations run using MC generators can only achieve limited accuracy. From a technical point of view limitations arise, for example, from the limited machine precision. The implementation of physics knowledge into computer code creates problems. Problems that often have to be worked around thus introducing uncertainties. Furthermore, several parameters are set as constants with limited precision in the generators even though they might not be exactly constant. Each of these issues introduce an uncertainty on the results obtained from MC generators and thus also on the results of this study (f_{DP}).
To determine the uncertainty due to the generator the fraction is calculated again using the same dijet sample but using both MC simulations with no-MPI, Pythia and Sherpa. Since the production of dijets is a very basic process, Pythia and Sherpa should not produce significantly different results. However, the creation of a Z boson and 2 jets can generate different results for different generators. To take this into account the dijet sample generated by Pythia was used and the fractions were calculated using the Pythia no-MPI sample and the Sherpa no-MPI sample. The resulting fractions are:

$$f_{\mathrm{DP}} = 1.31 \cdot 10^{-2} \pm 5.54 \cdot 10^{-3}$$

using the Sherpa no-MPI sample. Using Pythia no-MPI the fraction is:

$$f_{\mathrm{DP}} = 7.10 \cdot 10^{-2} \pm 5.47 \cdot 10^{-3}$$

The difference between the two fractions is $\Delta f_{\mathrm{DP}}^{\mathrm{Theo.}} = 0.0579$ and is considered as the systematic uncertainty on the generators. This uncertainty is very large, which is probably rather due to technical problems experienced during the simulation process than really different working principles within the generators.

5.6.2 Pile-Up

As of 2011 pile-up events became a non-negligible issue in experiments at the ATLAS detector. Pile-up events are events where more than one pp collision occurs in a

bunch crossing, thus, the recorded results consist of objects coming from different pp collisions (see also Chapter 5.1.1). In order to take care of this effect one would ideally only use those events with only one primary vertex. This would be the best approach but drastically reduce statistics, hence this approach is not chosen here. To remain with as much usable data as possible, the real data set is split up into two separate data sets depending on the number of primary vertices. One containing only those events with a higher than average number of primary vertices and another containing only those events with fewer than the average number of vertices. To estimate the influence of multiple proton collisions on the fraction of events with MPI f_{DP} in the total data sample the fraction will be calculated for each of the new subsamples. This approach is applied to both, the minimum bias and the muons data set.
The average number of primary vertices for the data sets was 5.67 for the minimum bias data sample (see Figure 5.36) and 10.02 for the muons data (see Figure 5.37) sample. Table 5.8 and Table 5.9 show the fractions calculated for the two data subsets.

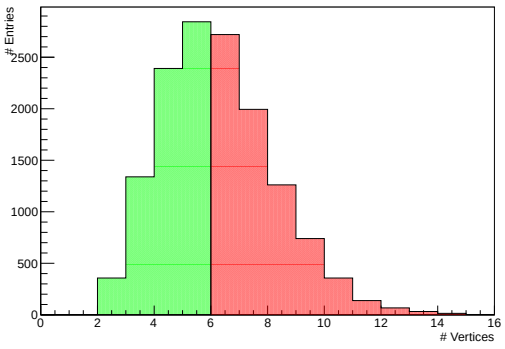

Figure 5.36: The figure shows the number of primary vertices in the minimum bias data sample. The green half contains fewer than average vertices, the red half events with more than the average number of vertices

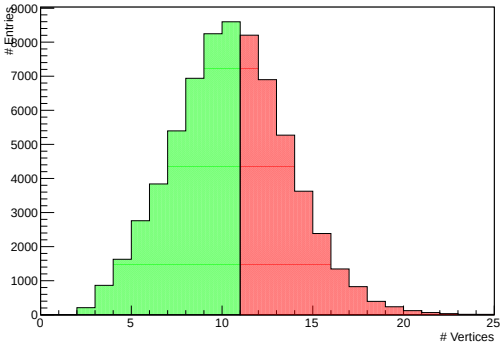

Figure 5.37: The figure shows the number of primary vertices in the muons data sample. The green half contains fewer than average vertices, the red half events with more than the average number of vertices

The average systematic uncertainty due to multiple proton interactions is thus about 6.88% for the fraction calculated with the dijet simulation generated by Pythia and the minimum bias data sample. In numbers the deviations are

$$\Delta f_{\mathrm{DP}}^{\mathrm{Pile-up}} = ^{+5.2}_{-5.5} \cdot 10^{-3} \ , \tag{5.16}$$

Generator	Data set	Fractions (small) f_{DP} & f_{SP}	χ^2/n_{df}
Pythia (MPI)	Muons	$f_{\mathrm{SP}} = 9.72 \cdot 10^{-1} \pm 7.03 \cdot 10^{-3}$ $f_{\mathrm{DP}} = 2.77 \cdot 10^{-2} \pm 2.85 \cdot 10^{-3}$	$\chi^2/n_{\mathrm{df}} = 1.74$
Pythia (MPI)	Min. bias	$f_{\mathrm{SP}} = 9.48 \cdot 10^{-1} \pm 1.48 \cdot 10^{-2}$ $f_{\mathrm{DP}} = 5.21 \cdot 10^{-2} \pm 7.42 \cdot 10^{-3}$	$\chi^2/n_{\mathrm{df}} = 0.98$
Pythia (dijets)	Muons	$f_{\mathrm{SP}} = 9.59 \cdot 10^{-1} \pm 7.55 \cdot 10^{-2}$ $f_{\mathrm{DP}} = 4.06 \cdot 10^{-2} \pm 4.15 \cdot 10^{-3}$	$\chi^2/n_{\mathrm{df}} = 1.71$
Pythia (dijets)	Min. bias	$f_{\mathrm{SP}} = 9.28 \cdot 10^{-1} \pm 1.43 \cdot 10^{-2}$ $f_{\mathrm{DP}} = 7.23 \cdot 10^{-2} \pm 8.22 \cdot 10^{-3}$	$\chi^2/n_{\mathrm{df}} = 0.67$
Sherpa (MPI)	Min. bias	$f_{\mathrm{SP}} = 8.79 \cdot 10^{-1} \pm 6.91 \cdot 10^{-2}$ $f_{\mathrm{DP}} = 1.21 \cdot 10^{-1} \pm 6.69 \cdot 10^{-2}$	$\chi^2/n_{\mathrm{df}} = 1.78$
Sherpa (dijets)	Min. bias	$f_{\mathrm{SP}} = 9.92 \cdot 10^{-1} \pm 1.50 \cdot 10^{-2}$ $f_{\mathrm{DP}} = 8.56 \cdot 10^{-3} \pm 7.49 \cdot 10^{-3}$	$\chi^2/n_{\mathrm{df}} = 1.82$

Table 5.8: Extracted fractions by the minimisation fit using the pile-up data sample with fewer than average vertices; f_{SP} = single parton scattering; f_{DP} = double parton scattering; The number of degrees of freedom $n_{\mathrm{df}} = 91$, in all cases

Generator	Data set	Fractions (large) f_{DP} & f_{SP}	χ^2/n_{df}
Pythia (MPI)	Muons	$f_{\mathrm{SP}} = 9.62 \cdot 10^{-1} \pm 7.85 \cdot 10^{-3}$ $f_{\mathrm{DP}} = 3.84 \cdot 10^{-2} \pm 3.44 \cdot 10^{-3}$	$\chi^2/n_{\mathrm{df}} = 1.73$
Pythia (MPI)	Min. bias	$f_{\mathrm{SP}} = 9.41 \cdot 10^{-1} \pm 1.46 \cdot 10^{-3}$ $f_{\mathrm{DP}} = 5.86 \cdot 10^{-2} \pm 7.55 \cdot 10^{-3}$	$\chi^2/n_{\mathrm{df}} = 1.12$
Pythia (dijets)	Muons	$f_{\mathrm{SP}} = 9.42 \cdot 10^{-1} \pm 8.35 \cdot 10^{-3}$ $f_{\mathrm{DP}} = 5.76 \cdot 10^{-2} \pm 4.71 \cdot 10^{-3}$	$\chi^2/n_{\mathrm{df}} = 1.58$
Pythia (dijets)	Min. bias	$f_{\mathrm{SP}} = 9.17 \cdot 10^{-1} \pm 1.39 \cdot 10^{-2}$ $f_{\mathrm{DP}} = 8.30 \cdot 10^{-2} \pm 8.16 \cdot 10^{-3}$	$\chi^2/n_{\mathrm{df}} = 0.66$
Sherpa (MPI)	Min. bias	$f_{\mathrm{SP}} = 8.25 \cdot 10^{-1} \pm 4.77 \cdot 10^{-2}$ $f_{\mathrm{DP}} = 1.75 \cdot 10^{-1} \pm 4.83 \cdot 10^{-2}$	$\chi^2/n_{\mathrm{df}} = 1.71$
Sherpa (dijets)	Min. bias	$f_{\mathrm{SP}} = 9.82 \cdot 10^{-1} \pm 1.25 \cdot 10^{-2}$ $f_{\mathrm{DP}} = 1.78 \cdot 10^{-2} \pm 7.04 \cdot 10^{-3}$	$\chi^2/n_{\mathrm{df}} = 1.75$

Table 5.9: Extracted fractions by the minimisation fit using the pile-up sample with more than average vertices; f_{SP} = single parton scattering; f_{DP} = double parton scattering; The number of degrees of freedom $n_{\mathrm{df}} = 91$, in all cases

While the uncertainty is rather modest in the case of minimum bias data it becomes considerable for the muons data sample (the generator is still PYTHIA simulating dijets).

$$\Delta f_{\mathrm{DP}}^{\mathrm{Pile-up}} = ^{+9.8}_{-7.2} \cdot 10^{-3} \ , \tag{5.17}$$

Turning now from the dijet simulations to the MPI simulations, the deviation in the minimum bias data sample is given by

$$\Delta f_{\mathrm{DP}}^{\mathrm{Pile-up}} = ^{+4.9}_{-1.6} \cdot 10^{-3} \ , \tag{5.18}$$

while the uncertainty in the muons sample is given by

$$\Delta f_{\mathrm{DP}}^{\mathrm{Pile-up}} = ^{+6.8}_{-3.2} \cdot 10^{-3} \ . \tag{5.19}$$

For SHERPA the uncertainty due to pile-up events was only calculated for the minimum bias data sample as it did not converge for the muons data sample. Using the dijet simulation the uncertainty introduced by multiple proton interactions is large but to a similar extent, 34.64% and 35.87% respectively.

$$\Delta f_{\mathrm{DP}}^{\mathrm{Pile-up}} = ^{+4.7}_{-4.5} \cdot 10^{-3} \tag{5.20}$$

For the full MPI simulation the errors differ much more, 3.96% and 38.88% respectively.

$$\Delta f_{\mathrm{DP}}^{\mathrm{Pile-up}} = ^{+49.0}_{-5.0} \cdot 10^{-3} \tag{5.21}$$

The percentage deviation is not given for all the data samples here as these are not the final results. The final results will be calculated in the following by applying a method that attempts to approximate the results calculated in this section for the different numbers of vertices back to only one vertex. This is a sensible ansatz since the impact of the uncertainty due to pile-up events is large and thus important in this study. The pile-up impact has already been calculated for both data samples. Assuming that there is a linear relationship between the two fractions at their corresponding average number of vertices the following equations can be established:

$$y_1 = f_0 + m v_1 \qquad\qquad y_2 = f_0 + m v_2 \ . \tag{5.22}$$

In the equations y_1 and y_2 stand for the fractions calculated with the minimum bias the muons data sample, while v_1 and v_2 are the average number of vertices. The y-axis coordinate f_0 can thus be calculated by

$$f_0 = \frac{y_1 + y_2}{2} - m\frac{v_1 + v_2}{2} \Rightarrow \Delta f_0 = \sqrt{\frac{\Delta y_1^2 + \Delta y_2^2}{4} + \Delta m^2 \left(\frac{v_1 + v_2}{2}\right)^2} . \quad (5.23)$$

The slope and the uncertainty on it are given by

$$m = \frac{y_2 - y_1}{v_2 - v_1} \Rightarrow \Delta m = \frac{\sqrt{\Delta y_2^2 + \Delta y_1^2}}{v_2 - v_1} . \quad (5.24)$$

Since the interest is actually on the fraction for one vertex on average it is not f_0 but f_1 that is sought after. It is given by

$$f_1 = f_0 + m \quad (5.25)$$

For the uncertainty this means

$$\Delta f_1 = \sqrt{\Delta f_0^2 + \Delta m^2} \quad (5.26)$$

The results for the fractions extrapolated back to one vertex on average are presented in Table 5.10.

Generator	Data set	Fraction $f_1 \pm \Delta f_1$
Pythia (MPI)	Muons	0.014 ± 0.010
Pythia (MPI)	Min. bias	0.046 ± 0.023
Pythia (dijets)	Muons	0.020 ± 0.014
Pythia (dijets)	Min. bias	0.062 ± 0.024
Sherpa (MPI)	Min. bias	0.069 ± 0.170
Sherpa (dijets)	Min. bias	0.000 ± 0.021

Table 5.10: Fractions of MPI that were extrapolated back to one vertex on average. For the extrapolation the information gained from splitting the data sample in a sample with larger than average vertices and a sample with fewer than average vertices was used. The method is described in more detail above.

5.6.3 Jet Energy Scale and Resolution

Jets reconstructed by the ATLAS detector and pure physics jets differ in that the former are affected by detector and physics effects thus introducing a systematic uncertainty. The ATLAS detector is a technical machine and thus has areas it cannot cover. Furthermore are particles measured by different sub-detectors consisting of components with limited resolution capability. On the other side, the recorded (raw) objects have to be converted into interpretable data. This is done using various algorithms like the reconstruction algorithms mentioned in Chapter 3.2.1 and Chapter 3.2.3. These programs suffer from technical drawbacks coming from limited machine precision as well as drawbacks from the working method of the algorithm. Particles actually belonging to a jet can for example be missed by the algorithm thus producing a jet that differs from the real physics jet. To account for these effects a Jet energy scale (JES) is calculated. It is determined by comparing events recorded by the ATLAS detector with Monte Carlo simulations.

The impact of the jet energy scale was determined by shifting the energy upwards and downwards in the MC samples by the jet energy scale uncertainty. The jet energy scale uncertainty was taken from an earlier study conducted on this topic [93]. Using the Anti-k_T algorithm with a $R = 0.4$ and low p_T ($p_T^{jet} = 20$ GeV) jets the uncertainty is 8.2% at maximum. This is measured in the pseudorapidity region $2.1 < |\eta| < 2.8$. The uncertainty is smaller in all regions with a smaller pseudorapidity, namely 4.5%. Here the uncertainty was calculated for the worst case scenario, meaning an uncertainty of 8.2%, which resulted in an uncertainty on the fraction f_{DP} of

$$\Delta^{\mathrm{JES}} f_{DP} = ^{+1.2}_{-1.9} \cdot 10^{-3} \ . \tag{5.27}$$

These values were obtained using the Pythia dijet simulation and the minimum bias data sample to perform the fit.

The uncertainty due to the jet energy resolution is determined by degrading the resolution in the MC sample by the jet energy resolution uncertainty. Afterwards the fit is performed again and the variation on the fraction is taken as the uncertainty due to the jet energy resolution. This is a well established approach and the jet energy resolution uncertainty has been determined very accurately which is why it is considered safe to use the uncertainty determined in an earlier similar study [27]. The uncertainty due to the jet energy resolution was determined to be

$$\Delta^{\mathrm{JER}} f_{DP} = -5 \cdot 10^{-3} \ . \tag{5.28}$$

Chapter 6

Conclusions and Outlook

The fraction of multiple parton interactions was measured in $pp \to Z + 2$ jet $+X$ events. Various data samples and different event generators (Pythia and Sherpa) were used to obtain information about multiple parton interactions. The fractions obtained from the different data samples and MC generators can be seen in table 5.7. Pythia produced very good results and the fractions calculated with these simulations were in a range that they were able to confirm an earlier, similar study [27]. The output generated by Sherpa on the other hand was very unexpected. However, it must be said that in simulations with Sherpa there were some serious technical issues. It is therefore rather likely that the differing results Sherpa produced were caused by technical rather than physical effects.
Using the results generated by Pythia and the minimum bias data sample, the calculated fraction was determined as

$$f_{DP} = 0.062 \pm 0.024 \text{ (stat.)} \pm 0.058 \text{ (sys.)}$$

. This result is very close to the results obtained in an earlier study [27] where the fraction of MPI was determined in $W \to l\nu + 2$ jet events. Sherpa on the other hand suggested a much higher fraction of MPI in the same data sample, namely

$$f_{DP} = 0.000 \pm 0.021 \text{ (stat.)} \pm 0.058 \text{ (sys.)} \ .$$

This result is however influenced by technical difficulties and must thus be considered with caution.
Interestingly, the fractions obtained by calculating the fraction of MPI using a simulation of MPI instead of dijet events posing as a replacement, the fractions decrease. For Pythia for example to fraction decreases to

$$f_{DP} = 0.046 \pm 0.023 \text{ (stat.)} \pm 0.058 \text{ (sys.)} \ .$$

using the same minimum bias data sample as before. The Sherpa simulations show similar behaviour

$$f_{DP} = 0.069 \pm 0.170 \text{ (stat.)} \pm 0.058 \text{ (sys.)} .$$

For the muons data sample the fractions obtained with Pythia were lower than for the minimum bias data sample. For the dijet simulations the fraction was

$$f_{DP} = 0.020 \pm 0.014 \text{ (stat.)} \pm 0.058 \text{ (sys.)} .$$

while the simulation with MPI suggested a fraction of

$$f_{DP} = 0.014 \pm 0.010 \text{ (stat.)} \pm 0.058 \text{ (sys.)} .$$

The systematic uncertainties presented on the these results were calculated with the uncertainties that were determined in Chapter 5.6 by adding them in quadrature. The theoretical systematic uncertainty is very large and thus has a large impact on the total systematic uncertainty. Since it was calculated with the results from the Sherpa simulations it can be expected that the uncertainty is overestimated due to the quality of these simulations. In order to obtain a more realistic estimation of the theoretical uncertainty the value calculated in [27] was used in Table 6.1.

Generator	Data set	Fraction $f_{DP} \pm \Delta f_{DP}$
Pythia (MPI)	Muons	0.014 ± 0.010 (stat.) ± 0.009 (sys.)
Pythia (MPI)	Min. bias	0.046 ± 0.023 (stat.) ± 0.009 (sys.)
Pythia (dijets)	Muons	0.020 ± 0.014 (stat.) ± 0.009 (sys.)
Pythia (dijets)	Min. bias	0.062 ± 0.024 (stat.) ± 0.009 (sys.)
Sherpa (MPI)	Min. bias	0.069 ± 0.170 (stat.) ± 0.009 (sys.)
Sherpa (dijets)	Min. bias	0.000 ± 0.021 (stat.) ± 0.009 (sys.)

Table 6.1: Final results for the fraction of MPI in different data sets. The results in this table are the ones obtained with the back extrapolation to one vertex on average in order to take care of pile-up effects and the corrected theoretical uncertainty.

MPI are not yet fully understood and hence are MC generators, or rather their implementation of MPI still exposed to unknown effects regarding MPI. It would therefore be useful to gain a deeper understanding of MPI in order to improve the theoretical knowledge of MPI and thus improve the MPI implementations in the generators. A further reason for an interest in MPI, that does not have to do with MC generators, is the fact that they are an important part of the Higgs search and take a serious role in SUSY experiments. In order to improve the quality of the results from experiments concerning either, the Higgs or SUSY search, it is important

to improve the current understanding of MPI. It is therefore also worthwhile to investigate MPI in different particle processes that have not yet been payed attention to in research regarding MPI. It would be useful to find out how MPI contributes to these, currently ignored, processes in order to determine whether some processes or properties show interesting or unexpected behaviour in relation to MPI.
Another very interesting approach would be to doubt the validity of the factorisation theorem by assuming that the two interactions in double parton scattering processes are in fact correlated. Hints that they are were already given in earlier studies [94, 95]. If true, this would have a significant effect on the currect understanding of MPI.
It would also be very interesting to investigate the frequency and properties of triple parton interactions (TPI). These processes are expected to occur much more seldom than double parton interactions but it has been argued that they could be observable at the LHC [29, 96]. It would be very exciting to determine how specific variables and properties of TPI behave, especially in relation to SPS and DPS processes.
Finally, and on a rather technical note. It must be added that it cannot be underestimated how important time is in generator based studies like this one. Before any (generator heavy) study is conducted an estimation on how long the simulations will take and how efficient they are is crucial and must be done with all necessary thoroughness.

List of Figures

List of Tables

Bibliography

[1] B. Povh et al. *Teilchen und Kerne: Eine Einfuehrung in die physikalischen Konzepte*. Springer-Lehrbuch, 8 edition, 2009.

[2] D. Griffiths. *Introduction to Elementary Particles*. John Wiley & Sons Ltd, 2 edition, 2008.

[3] J. Beringer et al. Review of particle physics 2012. *Phys. Rev. D*, 86(1), 2012.

[4] S. P. Martin. A Supersymmetry Primer. `http://arxiv.org/abs/hepph/9709356`. arXiv:hep-ph/9709356.

[5] Maxime Gabella. The Randall-Sundrum Model. `www-thphys.physics.ox.ac.uk/people/MaximeGabella/rs.pdf`.

[6] The DØ Collaboration. Search for Randall-Sundrum gravitons in the dielectron and diphoton final states with 5.4 fb-1 of data from ppbar collisions at sqrt(s)=1.96 TeV. *Phys. Rev. Lett.*, 104(241802), 2010.

[7] Supersymmetry: uniting the forces. `http://cms.web.cern.ch/news/are-there-more-particles-left-find`. Figure on force unification.

[8] O. Eberhardt et al. Impact of a Higgs Boson at a Mass of 126 GeV on the Standard Model with Three and Four Fermion Generations. *Phys. Rev. Lett.*, 109(241802), 2012.

[9] Wikipedia. The Standard Model of elementary particles. `http://en.wikipedia.org/wiki/Standard_model`, 2006.

[10] P. Higgs. Broken Symmetries and the Masses of Gauge Bosons. *Phys. Rev. Lett.*, 13:508–509, 1964.

[11] The ATLAS Collaboration. Observation of an Excess of Events in the Search for the Standard Model Higgs boson with the ATLAS detector at the LHC. *36th International Conference on High Energy Physics*, page 22, 2012.

[12] The CMS Collaboration. Observation of a new boson with a mass near 125 gev. http://cds.cern.ch/record/1460438. 4^{th} of July publication.

[13] The ATLAS Collaboration. Observation of a new particle in the search for the Standard Model Higgs boson with the ATLAS detector at the LHC. *Phys. Lett. B*, 716:1–29, 2012.

[14] The CMS Collaboration. Observation of a new boson at a mass of 125 GeV with the CMS experiment at the LHC. *Phys. Lett. B*, 716:30–61, 2012.

[15] M. Srednicki. *Quantum Field Theory*. Cambridge University Press, 1 edition, 2007.

[16] A. Messiah. *Quantum Mechanics: Two Volumes Bound as One*. Dover Publications Inc., 2003.

[17] L. Landau and E. Lifschitz. *Lehrbuch der theoretischen Physik, Band 1: Mechanik*. Harri Deutsch, 14 edition, 1997.

[18] S. Weinberg. *The Quantum Theory of Fields: Volume 1, Foundations*. Cambridge University Press, 2005.

[19] M. z. Nedden. Lecture script: Experimental elementary particle physics. http://www-hera-b.desy.de/people/nedden/lectures/04_05/exptp/, 2004.

[20] F. Halzen. *Quarks and Leptons: An Introductory Course in Modern Particle Physics*. John Wiley & Sons Ltd, 1 edition, 1984.

[21] S. Bethke. Experimental Tests of Asymptotic Freedom. *Prog. Part. Nucl. Phys.*, 58:351–386, 2007.

[22] G. Dissertori. *Quantum Chromodynamics: High Energy Experiments and Theory*. Oxford University Press, 1 edition, 2009.

[23] Official Nobel Prize Web Site. Asymptotic Freedom. http://www.nobelprize.org/nobel_prizes/physics/laureates/2004/popular.html, 2004.

[24] E. Komatsu et al. Five year Wilkinson Microwave Anisotropy Probe (WMAP) Observations: Cosmological Interpretations. *Astrophys. J. Suppl.*, 180(2):330–376, 2009.

[25] Illustration of an LHC proton-proton collision. http://imperialhep.blogspot.dk/2011/08/strangeness-at-lhcb.html.

[26] E. L. Berger and C. B. Jackson. Characteristics and Estimates of Double Parton Scattering at the Large Hadron Collider. *Phys. Rev. D*, 81(1), 2010.

[27] E. Dobson. A measurement of hard double-partonic interactions in W $\rightarrow l\nu + 2jet$ events using the ATLAS detector at the LHC. `http://cdsweb.cern.ch/record/1404953`, 2011.

[28] E. Maina. Multiple Parton Interactions in $Z + jets$ production at the LHC. A comparison of factorized and non-factorized double parton distribution functions. *JHEP*, 2011(061), 2011.

[29] E. Maina. Multiple Parton Interactions in $Z+4j$, $W^{\pm}W^{\pm}+0/2j$ and $W^{+}W^{-}+2j$ production at the LHC. *JHEP*, 2009(081), 2009.

[30] L. Evans and P. Bryant. LHC machine. *JINST*, 3(S08001), 2008.

[31] D. Fournier. Performance of the LHC, ATLAS and CMS in 2011. `http://arxiv.org/abs/1201.4681`, 2012. Presented at the 2011 Hadron Collider Physics symposium (HCP-2011).

[32] CERN. Geographic view of the LHC. `http://www.atlas.ch/photos/lhc.html`, 1999.

[33] CERN. LHC Cryodipole. `http://www.atlas.ch/photos/lhc.html`, 1998.

[34] C. Lefevre. CERN accelerator complex. `http://cdsweb.cern.ch/record/1260465`, 2008.

[35] I. Belikov. Physics of the ALICE Experiment. `http://arxiv.org/abs/hep-ex/0605035`, 2006.

[36] The LHCb Collaboration. The LHCb Detector at the LHC. *JINST*, 3(S08005), 2008.

[37] The LHCf Collaboration. The LHCf detector at the CERN Large Hadron Collider. *JINST*, 3(S08006), 2008.

[38] The TOTEM Collaboration. The TOTEM Experiment at the CERN Large Hadron Collider. *JINST*, 3(S08007), 2008.

[39] The MoEDAL Collaboration. Technical Design Report of the MoEDAL Experiment. `http://cds.cern.ch/record/1337782`, 2009. CERN-LHCC-2009-006.

[40] The CMS Collaboration. The CMS experiment at the CERN LHC. *JINST*, 3(S08004), 2008.

[41] CERN. ATLAS fact sheet. `www.atlas.ch/fact_sheets.html`, 2011.

[42] G. Aad et al. The ATLAS Experiment at the CERN Large Hadron Collider. *JINST*, 3(S08003), 2008.

[43] CERN AC. The ATLAS detector. http://cdsweb.cern.ch/record/39038, 1998.

[44] CERN AC. Particle tracks in the ATLAS detector. http://www.atlas.ch/multimedia/how-atlas-detects-particles.html, 2010.

[45] Gabriele Reiter. Studien zur Higgs-Produktion im Kanal $H \to W^+W^- \to \mu^+\mu^-\nu_\mu\bar{\nu}_\mu$ mit dem ATLAS Detektor am LHC, 2007. Master thesis, University of Munich.

[46] A. Grohsjean. *Measurement of the Top Quark Mass in the Dilepton Final State Using the Matrix Element Method*. Springer Berlin, 1 edition, 2010.

[47] The ATLAS Collaboration. Inner Detector description. http://www.atlas.ch/inner-detector.html.

[48] CERN AC. Figure of the combined inner detector. http://www.atlas.ch/photos/inner-detector-combined.html.

[49] The ATLAS Collaboration. Pixel Detector. http://www.atlas.ch/pixel-detector.html.

[50] P. Hansen and S. Xella. Experimental nuclear and particle physics, 2011. Lecture given at the University of Copenhagen.

[51] CERN. A computer generated image of the full calorimeter. http://www.atlas.ch/photos/calorimeters-combined-barrel.html.

[52] CERN. A computer generated image of the ATLAS muon spectrometer. http://www.atlas.ch/photos/muons-combined.html, 2008.

[53] K. Perez. Choice of Jet Algorithms in ATLAS, 2009. Presentation at ISSP 2009.

[54] G. P. Salam M. Cacciari and G. Soyez. The anti-kt jet clustering algorithm. *JHEP*, (063), 2008.

[55] ATLAS Collaboration. Reconstruction and identification of electrons. http://cdsweb.cern.ch/record/1171939, 2009. CERN-OPEN-2008-020.

[56] B. Resende. Muon identification algorithms in ATLAS. *PoS EPS-HEP2009*, page 431, 2009.

[57] W. Ji. Prospects of Observing the Decay $B_C \to J/\psi\pi$ and the Alignment Performance in the ATLAS Experiment, 2010. CERN-THESIS-2010-127.

[58] F. Siegert. Monte-Carlo event generation for the LHC. http://etheses.dur.ac.uk/484/, 2010. Ph.D. thesis, Durham University.

[59] A. Buckley et al. General-purpose events generators for lhc physics. `http://arxiv.org/abs/1101.2599`. arXiv:1101.2599 [hep-ph].

[60] T. Sjöstrand. Monte carlo generators. `http://arxiv.org/abs/hep-ph/0611247`. arXiv:hep-ph/0611247.

[61] The Geant4 Collaboration. `http://geant4.cern.ch/support/userdocuments.shtml`. Geant4 user documentation.

[62] S. Mrenna T. Sjöstrand and P. Skands. PYTHIA 6.4 Physics and Manual. *JHEP*, 05:026, 2006.

[63] S. Mrenna T. Sjöstrand and P. Skands. A Brief Introduction to PYTHIA 8.1. *Comput. Phys. Comm.*, 178:852–867, 2008.

[64] R. Fields. Pythia tune set a. `http://www.phys.ufl.edu/~rfield/cdf/tunes/py_tuneA.html`.

[65] P. Z. Skands. The perugia tunes. `http://arxiv.org/abs/0905.3418`. arXiv:0905.3418 [hep-ph].

[66] T. Gleisberg et al. Sherpa 1.4.2 Manual. `http://sherpa.hepforge.org/doc/SHERPA-MC-1.4.2.html`, 2012.

[67] The CTEQ Collaboration. `http://www.phys.psu.edu/~cteq/`. The Coordinated Theoretical-Experimental Project on QCD.

[68] The MSTW Collaboration. `http://mstwpdf.hepforge.org/`. Martin-Stirling-Thorne-Watt Parton Distribution Functions.

[69] The NNPDF Collaboration. `https://nnpdf.hepforge.org/`. Neural Network Parton Distribution Functions.

[70] H1 and Zeus Collaboration. `https://www.desy.de/h1zeus/combined_results/index.php?do=proton_structure`. HERA Parton Distribution Functions.

[71] The MSTW Collaboration. Parton density function figure. `http://www.hep.phy.cam.ac.uk/~wjs/partons2008nlo.jpg`, 2008.

[72] S. Höche et al. Matching Parton Showers and Matrix Elements. `http://arxiv.org/abs/hep-ph/0602031`, 2006. Proceedings of the "HERA and the LHC" workshop, CERN/DESY 2004/2005, arXiv:hep-ph/0602031.

[73] T. Sjöstrand et al. Pythia 8 online manual. `http://home.thep.lu.se/~torbjorn/pythia81html/Welcome.html`, 2012.

[74] S. Mrenna and P. Richardson. Matching Matrix Elements and Parton Showers with HERWIG and PYTHIA. *JHEP*, 05(040), 2004.

[75] N. Lavesson and L. Lönnblad. Merging parton showers and matrix elemens - back to basics. *JHEP*, 04(085), 2008.

[76] J. Alwall et al. Comparative study of various algorithms for the merging of parton showers and matrix elements in hadronic collisions. *Eur. Phys. J. C*, 53(473-500), 2008.

[77] T. Plehn. LHC Phenomenology for Physics Hunters. `http://arxiv.org/abs/0810.2281`, 2009. arXiv:0810.2281v2 [hep-ph].

[78] S. Catani et al. QCD Matrix Elements + Parton Showers. *JHEP*, 11(063), 2001.

[79] L. Lönnblad and S. Prestal. Matching Tree-Level Matrix Elements with Interleaved Showers. *JHEP*, 03(019), 2012.

[80] M. Gosselink et al. Radiating Top Quarks. `https://cdsweb.cern.ch/record/1295161?ln=en`. Ph.D. thesis, University of Amsterdam.

[81] B. Webber. Fragmentation and Hadronization. `www.slac.stanford.edu/econf/C990809/docs/webber.pdf`.

[82] D. Amati and G. Veneziano. Preconfinement as a Property of Perturbative QCD. *Phys. Lett. B*, 83(1):87–92, 1979.

[83] T. Toll. MC@NLO for Heavy Flavour Photoproduction at HERA, 2010. Ph.D. thesis, University of Hamburg.

[84] B. Webber. Parton shower Monte Carlo event generators. `http://www.scholarpedia.org/article/Parton_shower_Monte_Carlo_event_generators#Hadron_decays`, 2011.

[85] G. Barker et al. Studies on b-quark fragmentation. `www-ekp.physik.uni-karlsruhe.de/pub/web/DPG-Vortraege_2002/kerzel.ps.gz`, 2002.

[86] O. Biebel. Experimental tests of the strong interaction and its energy dependence in electron positron annihilation. *Phys. Rep.*, 340(3):165–289, 2001.

[87] The ATLAS Collaboration. Charged-particle multiplicities in pp interactions measured with the ATLAS detector at the LHC. *New J. Phys.*, 13(053033), 2011.

[88] A. Schwartzman D. W. Miller and D. Su. Jet-Vertex Association Algorithm. `https://cdsweb.cern.ch/record/1082880?`, 2008. ATL-COM-PHYS-2008-008.

[89] V. Blobel. Unfolding methods in high energy physics experiments. *Proceedings of the 1984 CERN School of Computing*, 85(09):88, 1984.

[90] G. D'Agostini. A multidimensional unfolding method based in Bayes' theorem. *Nucl. Instr. and Meth. in Phys. Res. A*, 362(2-3):487–498, 1995.

[91] T. Adye. RooUnfold: ROOT Unfolding Framework. `http://hepunx.rl.ac.uk/~adye/software/unfold/RooUnfold.html`, 2011.

[92] R. J. Barlow. *Statistics: A Guide to the Use of Statistical Methods in the Physical Sciences*. John Wiley & Sons Ltd, 1 edition, 2008.

[93] The ATLAS Collaboration. Jet energy scale and its systematic uncertainty in proton-proton collisions at sqrt(s)=7 TeV in ATLAS 2010 data. `http://cds.cern.ch/record/1337782`, 2011. ATLAS-CONF-2011-032.

[94] A. M. Snigirev. Double parton distributions in the leading logarithm approximation of perturbative QCD. *Phys. Rev. D*, 68(114012), 2003.

[95] V. L. Korotkikh and A. M. Snigirev. Double parton correlations versus factorized distributions. *Phys. Lett. B*, 594:171–176, 2004.

[96] E. Maina. Multiple Parton Interactions, top-antitop and $W+4j$, $W^{\pm}W^{\pm}+0/2j$ and $W^{+}W^{-}+2j$ production at the LHC. *JHEP*, 09(081), 2009.